# SET-POINT ALGORITHMS FOR ACTIVE HEAVE COMPENSATION OF TOWED BODIES

by

Clark Calnan

Submitted in partial fulfilment of the requirements
for the degree of
Master of Applied Science

at

Dalhousie University
Halifax, Nova Scotia
December 2016

*To my family; you have encouraged my curiosity.*

# TABLE OF CONTENTS

# LIST OF TABLES

# LIST OF FIGURES

# ABSTRACT

Active heave compensation is a technique used in marine applications to attenuate undesirable wave motions between a load and its host vessel. Motion attenuation is often achieved by reeling in or reeling out a cable tethering the load to the host vessel in response to the host vessel's heave motion. Most applications of active heave compensation are single degree-of-freedom systems which only operate vertically. In order to apply active heave compensation to towed bodies – which experience significant multiple degree-of-freedom disturbances – a "set-point algorithm" is required which determines the length of tow cable that should be reeled in or reeled out in response to external wave motion. This thesis proposes, implements, and assesses four different set-point algorithm approaches in experimental and simulated environments.

# LIST OF ABBREVIATIONS AND SYMBOLS USED

| Symbol | Description |
|---|---|
| $A$ | Representative cable cross-sectional area |
| $a$ | Cable radius of curvature |
| $A_E$ | Exposed area to fluid flow |
| $A_i$ | Cable segment cross-sectional area |
| $A_{\mathrm{O}}$ | Area of connection to PHC cylinder |
| ADHC | Actively Damped Heave Compensation |
| AHC | Active Heave Compensation |
| $Amp$ | Amplitude of cable oscillation |
| $B_m$ | Electric motor rotational friction |
| $B_R$ | Cable rotational damping |
| $b_p$ | Two-dimensional cable tangential linear damping coefficient |
| $b_q$ | Two-dimensional cable normal linear damping coefficient |
| $C_D$ | Submerged object drag coefficient |
| $C_d$ | Cable normal drag coefficient |
| $C_{DT}^i$ | Cable segment tangential drag coefficient |
| $\mathrm{C_f}$ | Servo valve flow coefficient |
| $C_s$ | Towed sphere drag coefficient |
| $C_t$ | Cable tangential drag coefficient |
| $\mathrm{C_V}$ | Valve damping |
| $D$ | Logarithmic decrement |
| $D_C$ | Characteristic length of submerged object |
| $d_C$ | Cable diameter |
| $D_i$ | Cable segment diameter |
| DOF | Degrees of Freedom |
| DSTO | Defence Science and Technology Organization |
| $E$ | Representative cable modulus of elasticity |
| $E_i$ | Cable segment modulus of elasticity |
| $f$ | Cable model forcing vector |
| $F_B$ | Buoyancy |
| $F_D$ | Drag force |
| $F_W$ | Gravitational force |
| FDM | Finite Difference Method |
| FEM | Finite Element Method |
| $g$ | Acceleration of gravity |
| $G_x$, $G_y$, $G_z$ | Flow signal gains in world reference frame |
| $I$ | Moment of inertia |
| $i$ | Electric motor current |
| IMU | Inertial Measurement Unit |
| $J$ | Cable rotational moment of inertia |
| $j$ | Imaginary variable |
| $J_m$ | Electric motor rotational inertia |
| $\boldsymbol{K}$ | Model stiffness matrix |
| $K_m$ | Electric motor back EMF constant |

| | |
|---|---|
| $K_R$ | Cable rotational stiffness |
| $K_T$ | Cable tensile stiffness |
| $L_i$ | Cable segment link *i* |
| $L_m$ | Electric motor inductance |
| $l_c$ | Characteristic length of change of tow cable |
| $l_i$ | Cable segment length |
| $l_{Tot}$ | Total tow cable length |
| $LP$ | Low-pass filter |
| $\boldsymbol{M}$ | Cable model mass matrix |
| $M$ | Cable moment |
| $m$ | Representative cable mass/length |
| $m_{CA}$ | Added mass of cylinder segment |
| $M_{CG}$ | Virtual mass of ROV cage |
| $m_i$ | Cable segment mass/length |
| $m_{obj}$ | Mass of object |
| $M_{ROV}$ | Virtual mass of ROV |
| $m_S$ | Towed body mass |
| $m_{SA}$ | Added mass of sphere |
| MPTP | Model Predictive Trajectory Planner |
| MPC | Model Predictive Control |
| $n$ | Cable oscillation cycles |
| $N(0, \sigma^2)$ | Zero-mean Gaussian distribution with variance of $\sigma^2$ |
| $p$ | Cable tangential deflection |
| PD | Proportional Derivative |
| PHC | Passive Heave Compensation |
| PI | Proportional Integral |
| PID | Proportional Integral Derivative |
| $q$ | Cable normal deflection |
| $r_C$ | Cable radius |
| $R_m$ | Electric motor coil resistance |
| $r_S$ | Radius of towed sphere |
| $r_X, r_Y, r_Z$ | Ellipsoid radii along ellipsoid axes |
| $Re$ | Reynolds Number |
| ROV | Remotely Operated Vehicle |
| $S$ | Cable shear force |
| **s** | Laplace variable |
| $s$ | Lagrangian cable co-ordinate |
| $SP$ | Set-point |
| $T$ | Cable tension |
| $t$ | Time |
| $T_p$ | Oscillation period |
| $T_t$ | Trajectory horizon |
| TS | Towed sphere |
| $U$ | Flow speed |
| $u$ | Two-dimensional cable tangential velocity |
| $U_i$ | Relative flow velocity to submerged object in $x_i$, $y_i$, $z_i$ frame |

| | |
|---|---|
| $u_i^p$ | Cumulative elastic displacement to node $p$ |
| $u_{sys}$ | System input |
| $U_x$, $U_y$, $U_z$ | Fluid flow in world reference frame |
| $\overline{U_x}$, $\overline{U_y}$, $\overline{U_z}$ | Mean fluid flow in world reference frame |
| $V$ | Electric motor voltage |
| $v$ | Two-dimensional cable normal velocity |
| $V_D$ | Displaced volume of water |
| $w_c$ | Controller disturbance |
| $w_0$ | Cable water weight/length |
| $x$, $y$, $z$ | Environment co-ordinates |
| $X_E$, $Y_E$, $Z_E$, | Ellipsoid co-ordinates |
| $x_i$, $y_i$, $z_i$ | Cable segment co-ordinates |
| $x_{sim}$ | Simulated state |
| $x_{sys}$ | System state |
| $y_{sim}$ | Simulated output |
| $y_{sys}$ | System output |
| $Z$ | Distance from mean sea surface to top cable element |
| $z$ | Discrete time variable |
| $\alpha$ | Ratio of valve opening area to port area between cylinder and accumulator |
| $\Delta x$ | Sheave displacement from nominal along world $x$ axis |
| $\Delta z$ | Sheave displacement from nominal along world $z$ axis |
| $\delta_i$ | Cable segment deflection |
| $\varepsilon_{C\,Max}$ | Maximum curvature strain |
| $\varepsilon_T$ | Tensile strain |
| $\zeta$ | Damping ratio |
| $\theta$ | Sheave angle |
| $\theta_m$ | Electric motor rotational position |
| $\theta_{nom}$ | Nominal sheave angle |
| $\lambda$ | Scaling factor |
| $\lambda_g$ | Gravitational scaling factor |
| $\lambda_l$ | Length scaling factor |
| $\lambda_m$ | Towed mass scaling factor |
| $\lambda_v$ | Velocity scaling factor |
| $\lambda_\rho$ | Fluid density scaling factor |
| $\mu$ | Dynamic fluid viscosity |
| $\rho_{oil}$ | Density of compensator cylinder oil |
| $\rho_w$ | Density of water |
| $\sigma_x$, $\sigma_y$, $\sigma_z$ | Flow variance in world reference frame |
| $\tau$ | Normal cable shear |
| $\varphi$ | Two-dimensional cable pitch angle |
| $\omega$ | Angular frequency |

## ACKNOWLEDGEMENTS

I would like to thank my graduate committee for their commitment and guidance throughout this project: Dr. Pan, Dr. Gonzalez-Cueto, and, in particular, Dr. Irani and Dr. Bauer. Your experience and motivation have been a huge help. I would also like to thank my father for helping me conduct my flume tank experiments.

# CHAPTER 1 INTRODUCTION

Collecting data for oceanographic research often requires the use of a towed body. Towed bodies are submerged behind a host vessel and towed through the water at a desired depth. Towed bodies can be outfitted with a wide range of sensory equipment which allows them to record oceanographic data during their tow. Depending on the purpose of the tow and the specific sensory equipment housed inside the towed body, the equipment could respond negatively to any undesired motion.

Often the influence of undesired towed body motion can be removed from data through data processing techniques [1], but in instances of high sea states or especially sensitive equipment, a method of motion-compensation is desired to prevent ship motion from impacting towed body motion. An illustration depicting the effects of unwanted ship motion on a towed body is presented in Figure 1.1.

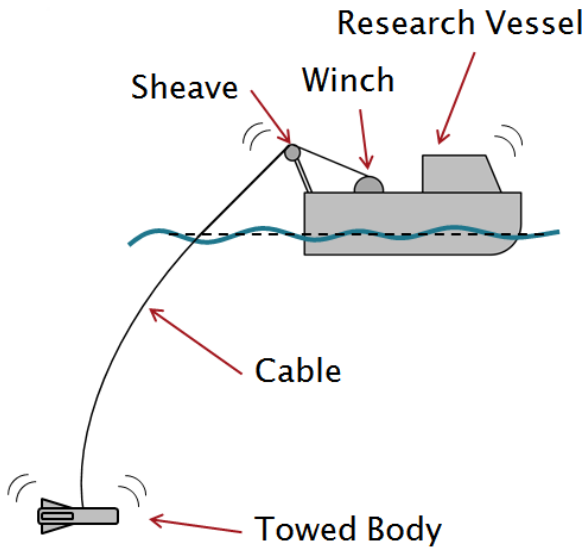


**Figure 1.1: Schematic of a research vessel transferring motion to a towed body via its tow cable.**

In Figure 1.1, the research vessel travels along the ocean surface and is therefore subjected to surface wave motion. The ship motion imparts disturbances at the sheave, which contacts the top of the tow cable. The tow cable then transfers the disturbance motion underwater to the towed body.

A compensation method is needed to effectively attenuate unwanted towed body motion caused by wave motion at the surface. Motion-compensation systems are typically referred to as heave compensation systems in the field of ocean engineering. Heave compensation systems can be categorized as either passive heave compensation (PHC) or active heave compensation (AHC) systems depending on the method of compensation which is employed.

PHC systems do not require a power source to function; instead they employ a vibration damping element along the tow line which attenuates towed body motion. Figure 1.2 and Figure 1.3 have been adapted from Woodacre [2] in order to demonstrate how a PHC system operates. Figure 1.2 shows a schematic of a ship attempting to maintain depth on its submerged load from states 1 through 3 using a PHC system, represented as a parallel spring and damper pair.

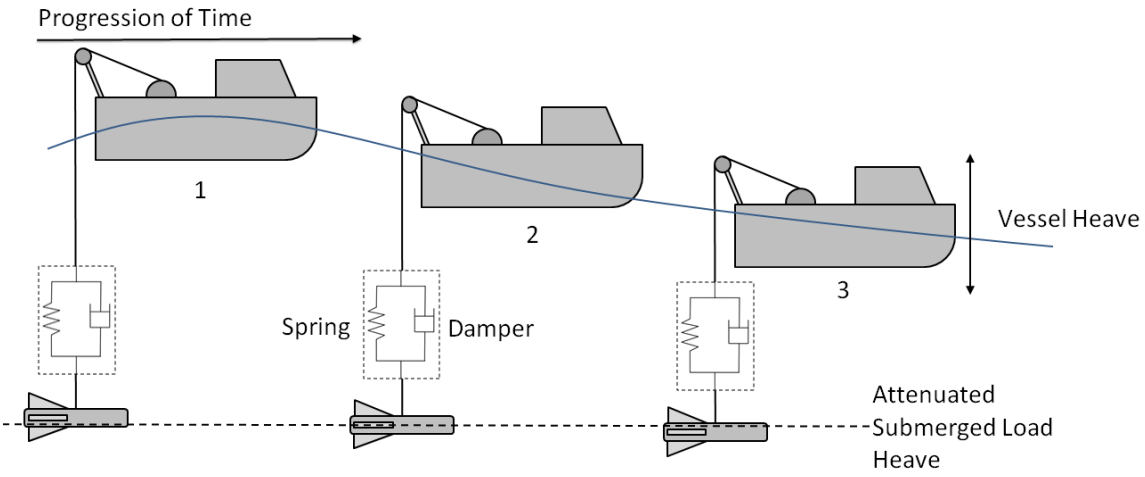


**Figure 1.2: Schematic of a PHC system.**

PHC system parameters can be tuned to shift the resonant peak of the cable-load system out of the expected wave disturbance frequency band. A bode plot of the PHC attenuation effect is presented in Figure 1.3. The compensated system response is attenuated so that a much lower magnitude response is produced from the wave frequency spectrum.

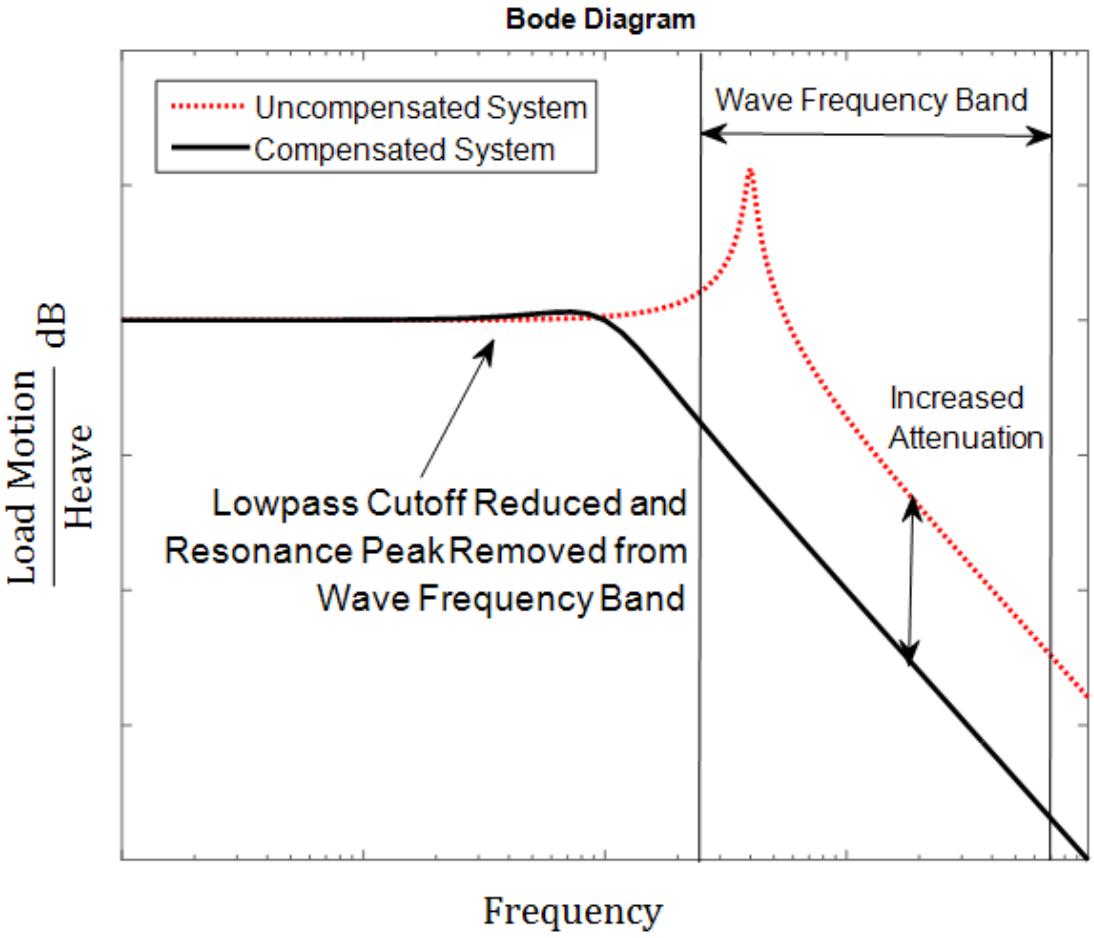


**Figure 1.3: Bode diagram of uncompensated and compensated load motion attenuation for a range of frequencies for a PHC system.**

As mentioned in Hatleskog and Dunnigan [3], passive compensation techniques can only be expected to reduce up to 80% of vertical heave motion induced on a submerged load. For applications which require better attenuation performance, AHC is needed. For example, Neupert et al. [4] were able to achieve 85% to 90% vertical motion reduction using an AHC crane system in experimental tests. AHC systems require powered actuation to operate, increasing system complexity, but offering the potential for increased performance. Figure 1.4 illustrates how the tow cable can be reeled in and out using an on-board winch to maintain a constant load depth in an AHC system. As the ship moves vertically in response to wave motion, its load is reeled in and out to maintain a constant depth from states 1 through 3.

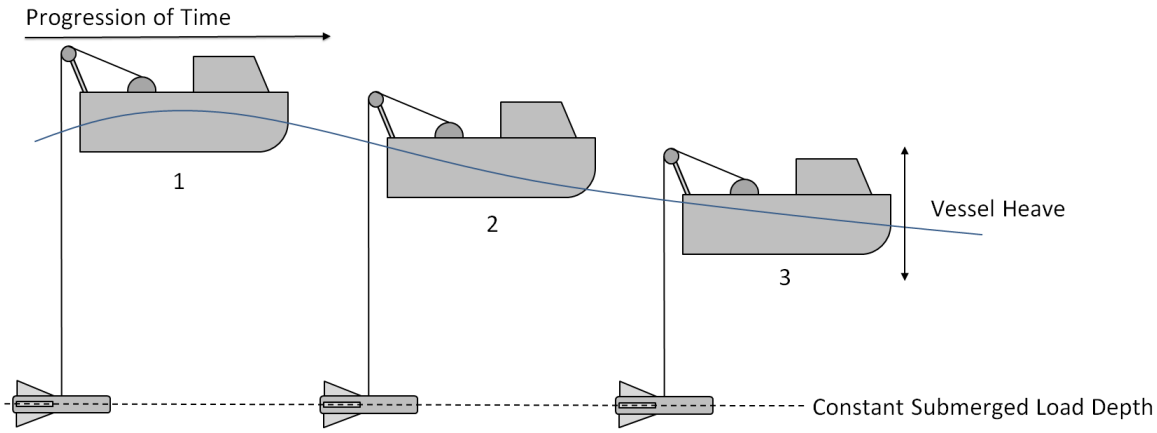


**Figure 1.4: Schematic of an AHC system.**

Most AHC research in ocean engineering tends to focus on vertical heave compensation [2]. Some of the most common applications of vertical heave motion-compensation are for offshore drilling operations and to stabilize Remotely Operated Vehicles (ROVs). In these scenarios, vertical heave tends to be the most dominant disturbance acting on the system and the tow cable is primarily oriented in the vertical direction resulting in a one degree-of-freedom (DOF) system. As the surface vessel heaves up, the winch must let out line equal to the heave displacement to effectively cancel the motion. Similarly, as the surface vessel lowers, the winch must reel line in equal to the displacement. A corresponding control loop is depicted in Figure 1.5, which outlines how on-board measurements of wave disturbances with an Inertial Measurement Unit (IMU) can be used to determine an appropriate closed-loop controller set-point.

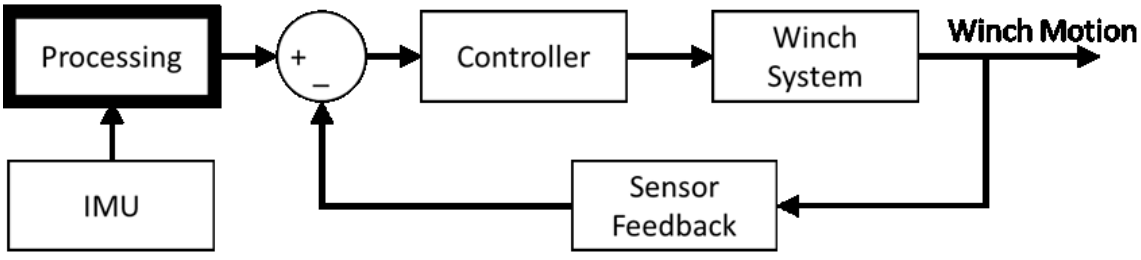


**Figure 1.5: Control loop directing the response of an on-board winch using processed IMU data for a reference signal.**

Determination of an appropriate set-point for closed-loop AHC controller actuation will be referred to as a "set-point algorithm" in this thesis. The set-point algorithm is applied

to the processing step in Figure 1.5. The winch controller and an appropriate feedback sensor, such as a winch encoder (to measure the actual length of tow line which has been reeled in or out) completes the control loop. In the case of the one DOF heave compensation system, the set-point algorithm is simple. Vertical motion of the host vessel's sheave is directly used as the winch controller's set-point.

Towed bodies operate when their host ship is underway. As waves interact with the surface vessel, the sheave point is not limited to simple vertical heave motion. Vessel motion takes place in six degrees-of-freedom. A diagram illustrating the six degrees of freedom and a frame of reference for describing ship motion is presented in Figure 1.6, adapted from Benedict et al. [5]. The back view on the left of the figure illustrates positive sway and heave directions along the vessel's *y* and *z* axes, respectively. Pitch and yaw are rotational motions about the *y* and *z* axes, respectively. The side view on the right completes the illustration by indicating positive surge along the vessel's *x* axis and roll about the *x* axis. Convention dictates that positive rotational motion is determined by the right-hand rule about each orthogonal axis.

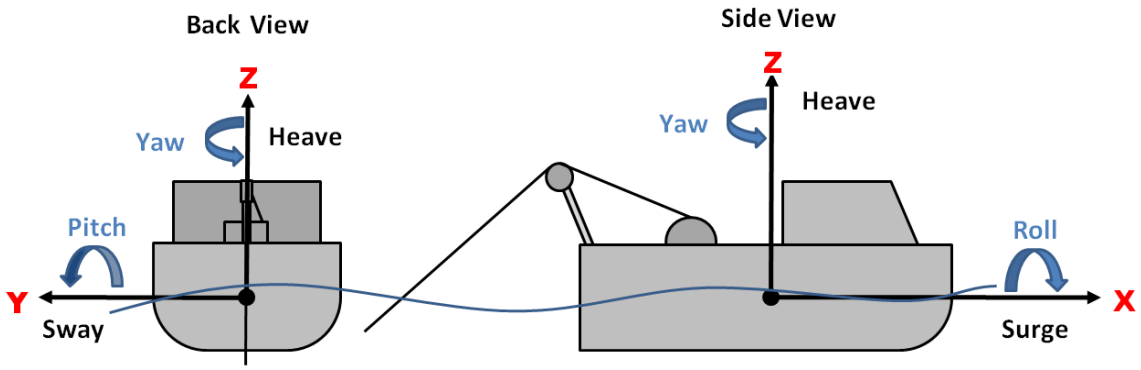


**Figure 1.6: Reference frame and six degrees of freedom for ship motion. Counter-clockwise rotation about an axis is positive.**

When a research vessel is underway, the tow cable connecting the towed body to the host vessel typically forms an arc along its length, resulting in a non-vertical angle at the sheave. This effect is illustrated in Figure 1.1 where the tow cable can be seen entering the water and curving downward toward the towed body. The particular shape of the tow cable is a function of several factors, such as weight, buoyancy, and drag forces on the towed body and tow cable, as well as host vessel speed.

As a result of the six DOF host vessel motion and tow cable geometry, AHC design for a generalized towed system is considerably more complex than a purely vertical system. Many towed bodies are constructed with moving stabilization fins or other actuators which can help attenuate unwanted motion. Much like AHC systems on-board the host vessel, towed bodies which are constructed in this way require a source of power for their actuators and can be considered "active" towed bodies, as opposed to "passive" towed bodies which are entirely dependent on the host vessel for navigation and stabilization. The effects of unwanted surface motion on passive towed bodies are the primary consideration of this thesis.

Because passive towed bodies are susceptible to imparted wave motion from their host vessel, an AHC system is desired. Unfortunately, due to the complicated behaviour of the tow cable during operation and the possibility of six DOF motion of the host vessel, the AHC system must be capable of using the host vessel's on-board sensory equipment to provide the winch system with an appropriate set-point for closed-loop control, as illustrated in the processing step in Figure 1.5. It should be re-iterated that the set-point algorithm for pure heave motion is relatively simple because the resulting set-point for pure heave motion is directly related to the vertical displacement of the host vessel. The case of heave compensation in purely vertical applications is discussed widely in the literature. Literature concerning AHC systems for passive towed bodies is sparse. *As a result, the first key objective of this thesis is to develop an appropriate set-point algorithm for the control of a winch-based AHC system to reduce surface disturbances on passive towed bodies.*

Additionally, it is assumed that information regarding the tow cable's angle as it leaves the host vessel's sheave (henceforth called the "sheave angle," displayed in Figure 1.7) is available to an on-board controller through the use of an additional measurement device. *It is a second key contribution of this thesis to assess the necessity of real-time measurement of the sheave angle.* The necessity of real-time sheave angle measurement is determined by comparing the performance of different control setups with real-time sheave angle measurement to trials where a constant nominal value is assumed.

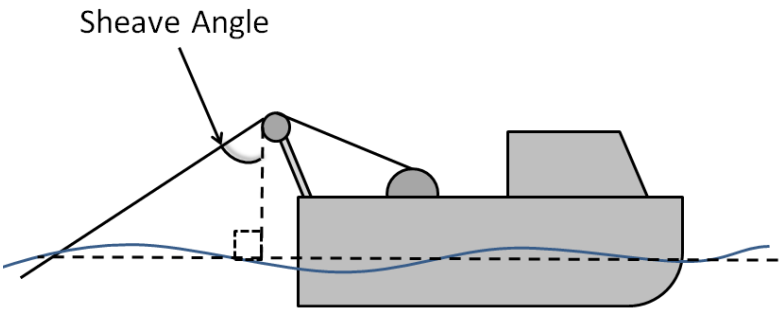


**Figure 1.7: Schematic of a research vessel underway with the sheave angle labeled.**

Multiple methods of producing an AHC system set-point are explored in this thesis. As a way of assessing their relative performance and selecting an effective solution, experimental trials are carried out. These experimental trials are also used to validate a computer simulator for further study and comparison of different set-point algorithms in a simulated environment.

Next, a full-scale simulator is created to implement an AHC system for a generalized towed sphere to compare the performance of different set-point algorithms. This simulator is used to alter the towed system parameters to a range of values to identify whether these parameters favour any particular set-point algorithm.

*It is the third objective of this thesis to report on test results collected from experimental and simulated trials of different set-point algorithms and, in doing so, assess the performance of the various control strategies.*

This thesis is divided into six chapters. Chapter 2 contains a literature review, which discusses heave compensation systems and computer simulation of marine tow cables in the publically-available literature. Chapter 3 discusses experimental tests which were conducted to empirically compare the performance of different control strategies on a small-scale test rig. Chapter 4 contains work which was carried out to construct and validate a small-scale computer simulator of the experimental test environment. In Chapter 5, a full-scale computer simulator is presented, which is used to further compare the different control strategies. Different towed body parameters, tow cable parameters, and tow depths are also explored through a parametric study. Finally, Chapter 6

summarizes the results and contributions of this thesis and indicates potential areas for future work.

# CHAPTER 2 CABLE MODELS AND HEAVE COMPENSATION

While AHC systems are the primary focus of this thesis, both PHC and AHC systems are currently employed for a range of heave compensation applications. Occasionally, PHC and AHC are used in tandem to produce a "semi-active" heave compensation system. PHC systems are most commonly found in the literature as a solution for towed body heave compensation. Unfortunately, while PHC systems are generally less expensive and less complex, they are also less effective at attenuating unwanted vessel motion [2]. In a towed application where better attenuation performance is needed, an AHC system may be desirable. Section 2.1 will investigate a range of PHC, AHC, and semi-active heave compensation systems which have been developed in the literature for pure vertical motion, as well as some methods which have been designed for applications with towed loads.

Like many engineering fields, ocean engineering benefits greatly from computer simulation. Many marine cable systems are large and expensive, and hiring a vessel for in-the-field testing can incur large costs. Research has been conducted to develop mathematical models of marine cables which are used to simulate an ocean environment preceding field work. Section 2.2 will present some examples of marine cable models which have been documented in literature. Based on the cable models examined in Section 2.2, a cable model will be simulated in this thesis to evaluate the performance of towed body AHC systems.

Finally, Section 2.3 will revisit some of the key contributions of this thesis as stated in Chapter 1 and indicate how the current literature can be applied to these contributions and advance heave compensation technology for towed bodies.

## 2.1. HEAVE COMPENSATION

This section presents heave compensation systems which have been designed for a wide range of marine applications. PHC systems are discussed in Section 2.1.1 as the first category of heave compensation systems. Section 2.1.2 discusses AHC systems, including control strategies which are used to actuate motion compensating mechanisms. Finally,

Section 2.1.3 discusses semi-active heave compensation systems, which are a blend of active and passive systems.

### 2.1.1. Passive Heave Compensation

PHC systems require no power to operate. PHC systems are widely applied to the field of ocean engineering and are commercially available from various manufacturers, such as Bosch Rexroth [6] or Craneworks [7]. Many commercially available PHC systems consist of a cylinder and accumulator system which act as a damper as described in Chapter 1. These systems can be positioned above or below the water surface, and some are designed to operate in both environments. A simple schematic of the cylinder PHC system is presented in Figure 2.1.

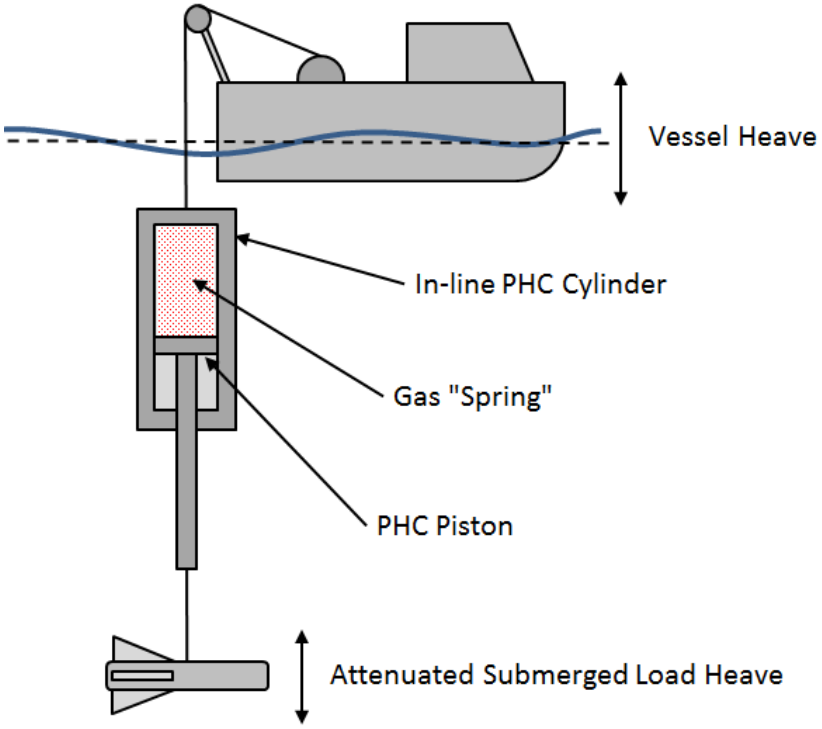


**Figure 2.1: Towed body system with a gas cylinder PHC system.**

The illustrated PHC system in Figure 2.1 acts as a vibration isolating spring which dampens vessel motion relative to the submerged load below the surface. Typically an accumulator is added to the system for ship-based PHC. Accumulators and pistons can be sized to control the compensator stiffness, since the piston force is a product of piston

pressure and cross-sectional area. PHC attenuation parameters can be tuned for a particular application by selecting an appropriate PHC system stiffness [8].

A limitation of this simple mechanical design arises from the inability to adjust gas pressure during operation to adapt to changes in hydrostatic pressure over a range of depths [8]. As hydrostatic pressure changes, it creates an inconsistent loading force on the PHC piston rod, which affects the performance of the PHC system. This limitation is addressed in the application of a depth compensator to the gas accumulator as presented in Cannell et al. [9]. Figure 2.2 shows a schematic adapted from the patent.

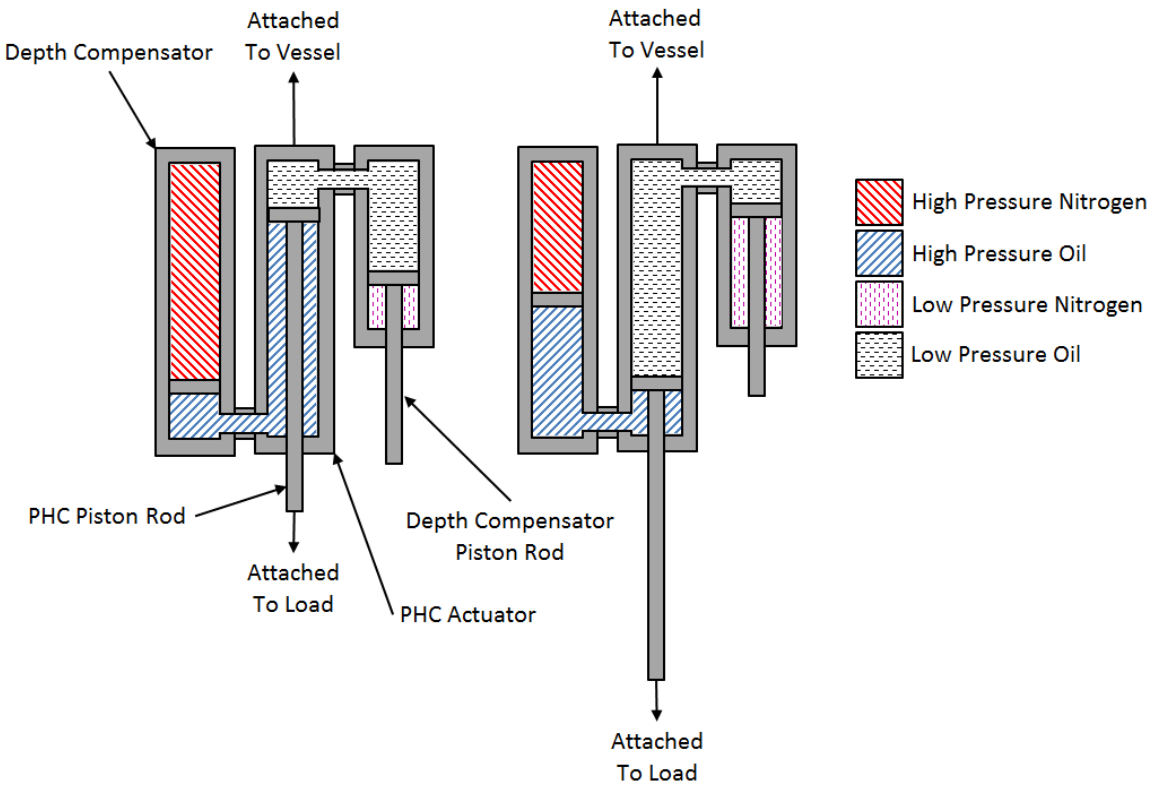


**Figure 2.2: Depth compensated PHC system in retracted and extended states.**

In the PHC system depicted in Figure 2.2, pressure applied to the main PHC piston rod is transferred to an accumulator piston using high pressure incompressible oil. In the PHC's retracted state, the high pressure oil allows the accumulator's nitrogen gas to expand, while in the PHC's extended state, the accumulator gas is compressed. Accumulator gas expansion and compression provides motion attenuation. Because this system is intended for use underwater, the effect of changing hydrostatic pressure can be counteracted with

the depth compensator. The depth compensator piston rod is exposed to the current hydrostatic pressure in the same manner as the main PHC piston rod. Because an equivalent hydrostatic pressure is applied on either side of the main PHC piston, any pressure differential on the PHC piston is cancelled. The depth compensator thereby allows for the system to perform consistently at a range of depths.

Wu et al. [10] propose an on-board PHC system which is intended for ROV applications. Their design is sized to reduce the possibility of snap-loading the ROV umbilical tether, while minimizing required deck space. By restricting oil flow between the cylinder and accumulator with a servo valve, damping effects can be tuned, which allows for the PHC system to avoid resonance effects while in operation. The system's damping coefficient is changed by controlling the servo valve's opening area. The damping caused by the valve opening is shown in Equation (2.1):

$$C_V = \frac{\rho_{oil}}{2C_f^2\alpha^2}A_O \tag{2.1}$$

where $C_v$ is the damping caused by the valve opening, $\rho_{oil}$ is the density of the oil used in the compensator cylinder, $\alpha$ is the ratio of the area of the valve opening to the cross-sectional area of the connection between the cylinder and the accumulator, $A_O$ is the area of the connection to the cylinder, and $C_f$ is the flow coefficient, which is a function of $\alpha$. It can be observed in Equation (2.1) that, when the valve opening $\alpha$ is reduced, the damping $C_v$ is increased. Valve control can, therefore, be used to achieve a desired damping value. Additionally, the cylinder system proposed by Wu et al. [10] is equipped with a set of pulleys which, for the same piston stroke, can increase the length of the tow cable being reeled in or out – effectively reducing the required deck space.

A fourth-order Runge-Kutta method is used to solve nonlinear dynamic equations in a simulation of Wu et al.'s [10] proposed PHC system. Through multiple simulations with differing forcing periods, it was observed that without damping regulation, resonance can greatly impede performance and result in the PHC system causing heave motion amplification rather than attenuation. However, with damping regulation enabled, resonance effects can be completely removed. The performance of the system without

damping regulation is approximately the same as when the forcing frequencies are far from resonance, indicating that damping regulation is effective. Despite the improvements offered by damping regulation, 100% motion attenuation is not possible with vibration damping. It will be seen later in Section 2.1.3 that the approach taken by Wu et al. [10] with damping regulation can be adapted into an active control loop to adjust damping in real-time in and respond to fluctuating input frequencies.

The method of increasing the effective piston stroke with pulleys used by Wu et al. [10] is similar to a method proposed by Driscoll et al. [11], who presented a mechanism for PHC of ROVs. The PHC system proposed by Driscoll et al. [11] is to be mounted to a ROV cage, which is a protective structure tethered to the host vessel and ROV that can be used in deployment and retrieval and to manage excess ROV tether. Figure 2.3 depicts a diagram of the pulley mechanism.

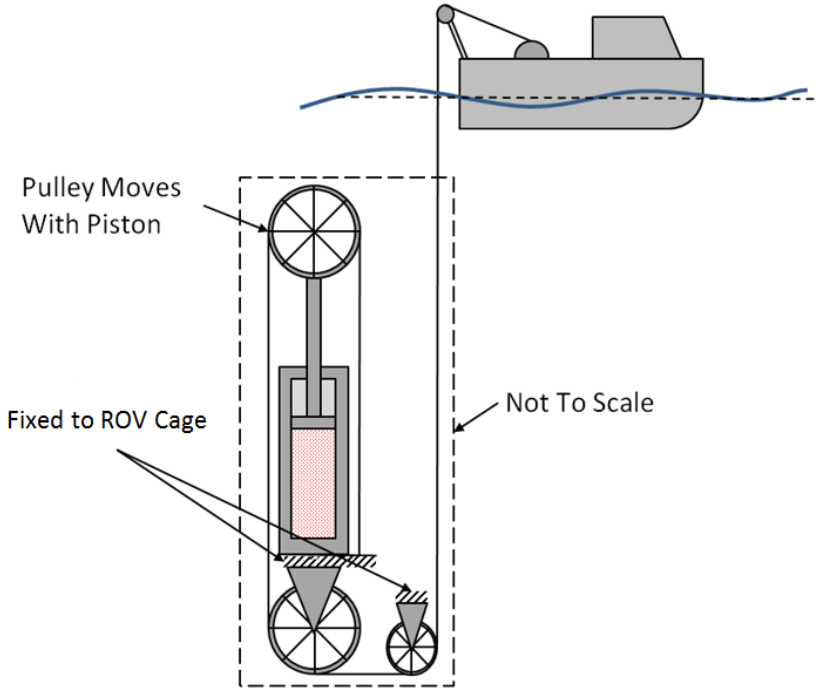


**Figure 2.3: Cage mounted PHC system with pulleys to extend compensation stroke.**

Referring to Figure 2.3, the PHC system presented by Driscoll et al. [11] has one end of the tow cable fixed to the ROV cage. The cable then loops around a pulley which is fixed to a piston. As the piston stroke damps perturbations, the pulley increases the tow cable

response, which allows for a more compact cylinder design. In Figure 2.3, the tow cable extension or retraction is twice as long as the piston stroke. Extending the length of tow cable which can be used for heave compensation is useful, especially in towed applications in high sea states, where large waves and combined vessel motions can lead to large vessel displacements.

One method of PHC described by Hover et al. [12] used for towed loads involves attaching floats to the tow cable in order to achieve a static "s-shape" depicted in Figure 2.4. Hover et al. [12] performed an analysis of this method using a linearized cable model adapted from Bliek [13] and a tow depth of 100 m. Generally the analysis revealed as much as 90% attenuation of heave and surge from 0.5 rad/s to 1.2 rad/s. For lower and higher frequency inputs, however, attenuation suffered, decreasing to 70% at 0.2 rad/s. The frequency response analysis of the s-shaped cable revealed several peaks within the wave frequency spectrum which could easily become prohibitive for use with forward-looking visual or sonar systems, as it was found that towed body pitch could oscillate by up to 3.5 degrees peak-to-peak.

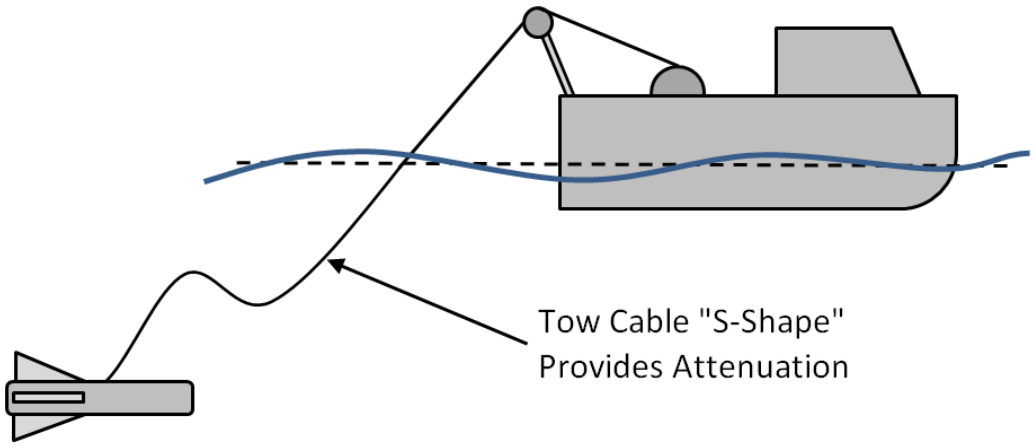


**Figure 2.4: PHC system consisting of buoyant cable section. The S-shape attenuates vessel heave relative to the towed body.**

PHC systems excel at providing reasonable motion attenuation at a relatively low cost for a range of applications, including towed bodies. Unfortunately, PHC systems are only capable of reacting to a specific range of input frequencies and always allow some level

of motion transmission. It is, therefore, impossible for a PHC system to achieve 100% motion attenuation, and limitations of approximately 80% motion attenuation for PHC systems have been observed [2]. In order to improve motion attenuation, powered actuation provided by an AHC system is explored.

### 2.1.2. Active Heave Compensation

Unlike PHC systems, strict AHC systems forego any significant passive component, meaning that their performance is entirely dependent on sensors and actuators. By relying on actively controlled components, AHC systems represent an opportunity for the application of advanced control algorithms to achieve good heave compensation. While AHC systems generally outperform PHC systems, they require power to operate, and are often more complex and expensive. Many AHC systems exist in literature, however most of the designs are (as is the case with PHC and semi-active heave compensation systems) primarily intended for ROV and offshore drilling applications.

The control diagram presented in Figure 2.5 is adapted from Gu et al. [14]. The control architecture applied is a cascade configuration. The controller consists of an outer proportional controller and an inner proportional-integral controller. The outer controller is used for payload positioning using an angular position set-point for the winch, while the inner controller is used for heave compensation. In simulation with idealized sinusoidal wave motion, the controller structure is capable of achieving 99% motion attenuation in simulation. More complicated wave motion is not examined.

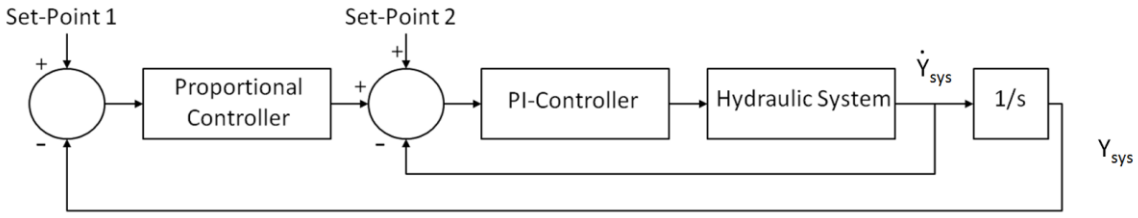


**Figure 2.5: Control loop for AHC system. Proportional control is used to determine speed response for changing position reference on inner control loop.**

Do and Pan [15] present an advanced controller architecture for an AHC system with a non-linear approach for an offshore drilling application with actuation provided by an

electro-hydraulic system. Disturbance observers are used to model immeasurable disturbance effects arising from the drill string's reaction force on the compensation system as well as any effects resulting from the linearization of friction forces. Lyapunov's direct method is used to generate a non-linear controller. Parameters are taken from Korde [16] and Yao [17] to simulate the system and assess its performance. A motion attenuation of 97.5% is achieved in their simulation.

Hatleskog and Dunnigan [18] indicate that time delay effects can impede an AHC system in achieving 100% motion attenuation. The severity of the time delay effect is dependent on the particular application and compensation mechanism. The work of Richter et al. [19] addresses time delay with an advanced control solution for AHC. The paper presents a controller design for a two DOF AHC system. In order to function properly, the AHC system requires a smooth real-time reference trajectory. To overcome time delay and actuator limitations, a model predictive trajectory planner (MPTP) is presented. The MPTP design is framed as a constrained open-loop optimal control problem. MPTP uses model states to derive the AHC reference trajectory and as a result, the MPTP is independent from the physical system. The predictive component of MPTP relies on work carried out by Kuchler et al. [20] and Fusco and Ringwood [21] on short-term wave forecasting to overcome inherent time delays.

Shortcomings of the MPTP design involve a lack of generalized solvability. The constrained optimization problem is not guaranteed to be feasible, and as such, the MPTP algorithm can return without a result. Soft constraints, as described in Rao et al. [22] cannot be used due to computational limitations arising from real-time trajectory generation. Instead, a fallback strategy is presented wherein polynomials are used to parametrize highly differentiable trajectories with acceleration and jerk values of zero at the beginning and end of the forecast window. Examples of an acceptable and an unacceptable velocity trajectory are illustrated in Figure 2.6 which has been adapted from Richter et al. [19]. The undesired trajectory is projected to $T_t$ and has an arbitrary terminal acceleration and jerk value, while the desired trajectory begins and completes the projection with acceleration and jerk values of zero.

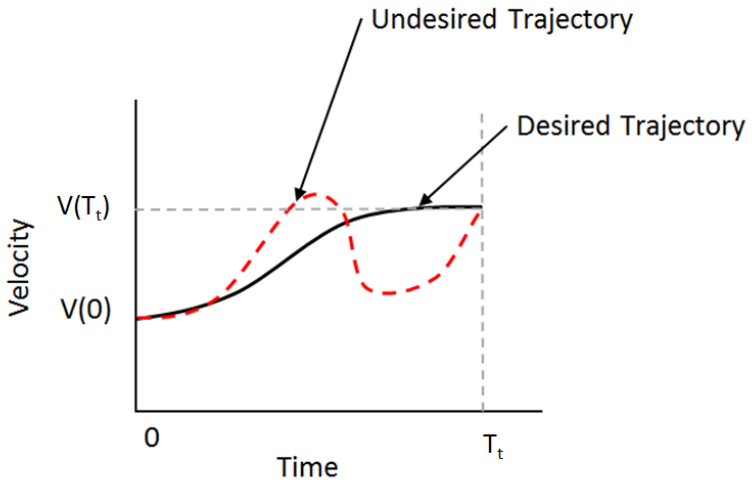


**Figure 2.6: AHC velocity response for desired and undesired trajectories.**

Simulation and experimental results from Richter et al. [19] indicate good performance of the MPTP system. Smoothness is lost in the presented experimental results; however, Richter et al. [19] state that MPTP weighting coefficients can be tuned depending on the particular controller to improve smoothness.

Additional model predictive work was conducted by Woodacre [23], [24] also drawing on a wave forecasting algorithm from Kuchler et al. [25]. Woodacre's [23] work includes system identification and model linearization of a non-linear hydraulic test rig with significant time delay. The test rig is representative of relatively inexpensive hydraulic equipment which might be found on small oceanographic research vessels. As a result of the significant time delay within the hydraulic system, a model predictive controller (MPC) is explored. Figure 2.7, adapted from Richter et al. [19], illustrates the difference between MPTP and MPC approaches.

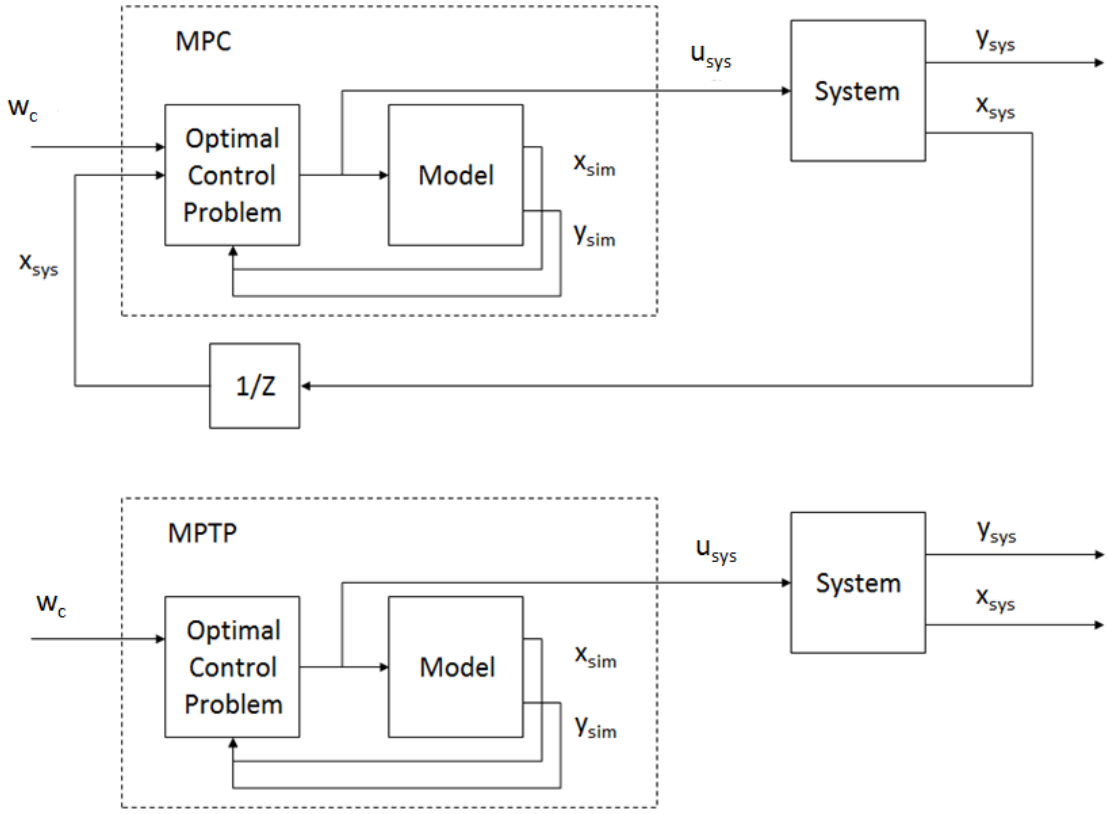


**Figure 2.7: Control loop comparison between MPC and MPTP for AHC system.**

The MPC control technique is similar to the MPTP design presented by Richter et al. [19], except that MPC introduces a feedback component. This feedback enables MPC model states to be updated with physical values instead of maintaining independence from the physical system. With significant model non-linearities, this feedback component presents an opportunity to improve controller robustness over an MPTP design

Woodacre [23] simulates MPC performance against a PID controller for benchmark wave motion data. The results show that the MPC controller is able to outperform the PID controller. MPC performance suffers when measurement noise is added to the simulation, but Woodacre [23] states that a low-pass filter can alleviate this problem, leading to an effective solution for AHC time delay.

With recent work in the development of predictive control, AHC systems can provide increasingly superior motion attenuation performance relative to PHC systems.

Additionally, winch-based AHC systems have practically no limitations with regards to the length of cable which can be extended or retracted in response to vessel motion, whereas PHC systems are limited by the length of the attenuation mechanism. As a result of these advantages, this thesis focuses on winch-based AHC systems.

### 2.1.3. Semi-Active Heave Compensation

Semi-active heave compensation describes a combination of PHC and AHC systems. A passive system may be paired with an active system to reduce the power requirement of the heave compensation system. Semi-active heave compensation systems may also be used as a precautionary design measure in the event of an AHC system failure, thereby increasing overall system robustness. The majority of semi-active heave compensation systems in the literature have been applied to ocean drilling from floating platforms [26].

In an effort to reduce the power requirements of typical AHC systems for offshore drilling applications, Huang et al. [27] designed a semi-active draw-works heave compensation system. Figure 2.8 depicts a mechanical schematic of the semi-active system.

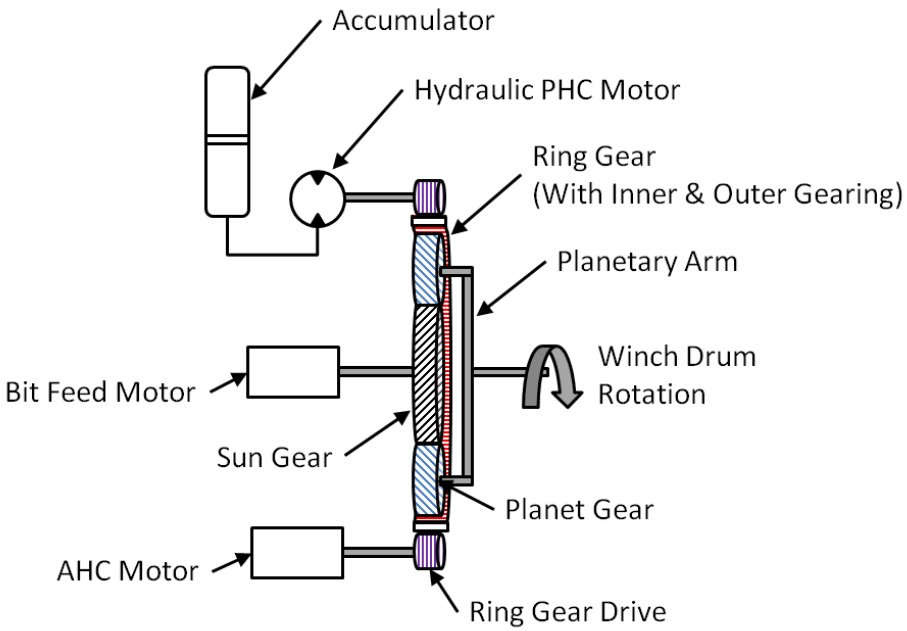


**Figure 2.8: Semi-active heave compensation system with a planetary gear mechanism.**

The system in Figure 2.8 uses a differential planetary gear reduction drive for advancing the drill bit. The gear mechanism accepts two inputs to provide a single output. The system is driven by an electric motor for AHC on the ring gear. Also meshing with the ring gear is a hydraulic motor and gas accumulator providing PHC. The sun gear is driven by the bit feed motor, while the draw-works shaft and drum are connected to the planetary gear arm. This system allows for constant speed operation of the bit feed motor for heave compensation while lowering the drill bit. The benefit of allowing constant bit feed motor operation does not translate easily to a towed application where it is common to maintain a constant depth of tow. This system uses a PID controller to drive the AHC motor. The semi-active heave compensation system attenuated 95% of motion by simulation and 90% by experimental results.

Liu et al. [28] present another semi-active heave compensation design with the intent of reducing power consumption over AHC systems. Their mechanical semi-active heave compensation system uses compression cylinders and a rack and pinion to compensate for heave. Figure 2.9 contains a diagram of their proposed design.

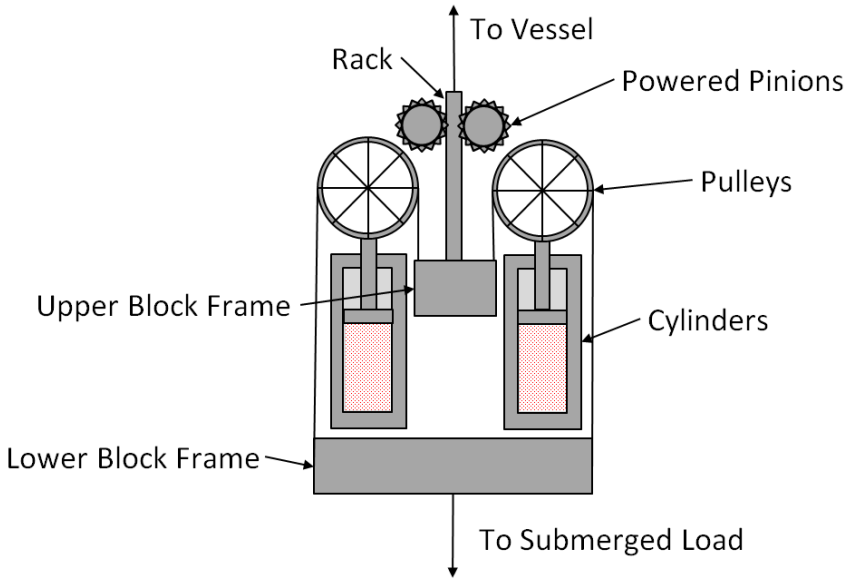


**Figure 2.9: Schematic of a semi-active heave compensation system with a rack and pinion.**

The system in Figure 2.9 uses a pair of cylinders to provide passive motion compensation between the lower and upper block frame. The rack and pinion set moves the entire assembly for AHC of vessel motion. Vessel motion is, therefore, first compensated with the AHC components, then PHC components. The performance of Liu et al.'s design [28] is similar to an AHC system, while consuming approximately 12% of the power of an AHC system in simulation with AMEsim software. Additionally, when the PHC component of the semi-active compensation system is compared to a strictly PHC system, the accumulator volume is reduced by half, thereby requiring less deck space for the proposed design. Despite reducing cylinder size, the design presented by Liu et al. [28] may be oversized for many towing applications and limit the extension and retraction length as a result of the cylinders and rack and pinions.

Yuan [29] presents a concept for a semi-active heave compensation system for offshore drilling applications which the author entitles an "actively damped heave compensation" (ADHC) system. The ADHC system is comprised of a typical AHC system driven by a hydraulic motor similar to the method presented by Yang et al. [30], however it also allows for real-time control of system damping through valve actuation, similar to the concept presented by Wu et al. [10]. The ability to control damping allows for

compensation of induced cable tension from subsea effects on the tow cable and payload, as well as vessel heave. The presented design's performance is simulated in MATLAB and Simulink. Wave dynamics are simulated along with ship perturbation. The ADHC system performance is compared to an AHC system without active damping enabled. Peak-to-peak heave motion at the sheave is in excess of 4 m for the trial. The AHC system without active damping experiences payload heave of 0.7 m signifying a modest motion attenuation of 83%, while the ADHC system is capable of reducing payload motion to 0.02 m signifying a motion attenuation of 99.5%. This enormous improvement is also in observed in attenuation of cable tension fluctuations, which exhibits a peak-to-peak range of 80 kN for the AHC system and approximately 2 kN for the ADHC system.

While most of the available literature concerning semi-active heave compensation focuses on offshore drilling applications, the work of Quan et al. [31], [26] details the design of a semi-active heave compensation system for an ROV application. Figure 2.10 depicts the proposed design.

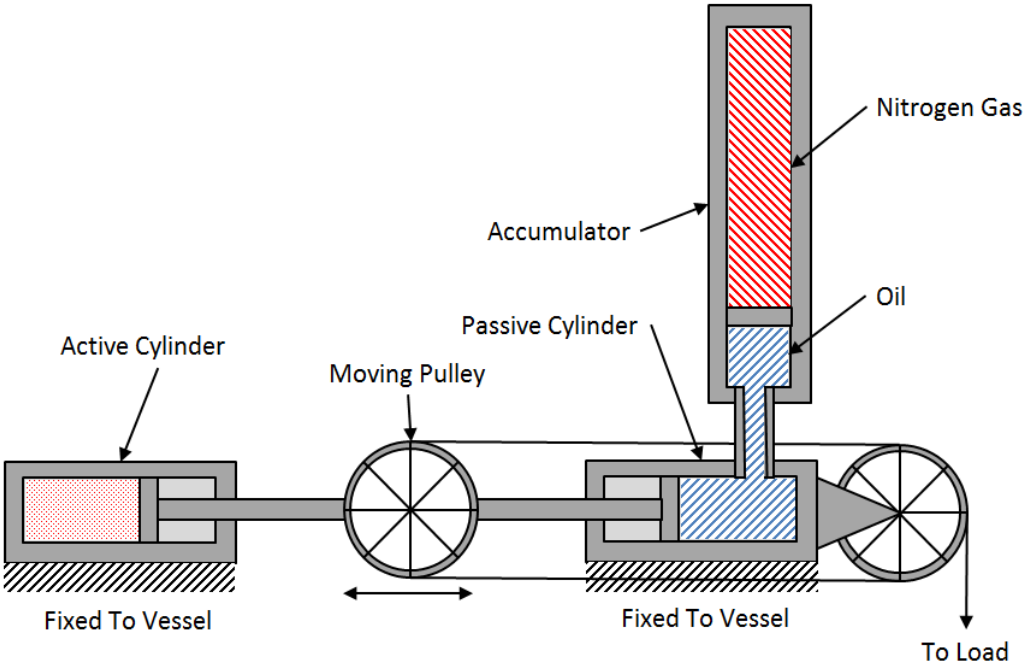


**Figure 2.10: Dual piston semi-active heave compensation system.**

The system aims to reduce heave on a ROV cage using a pair of cylinders mounted to the host vessel in parallel. One cylinder is actively controlled, while the other is passive and connected to a nitrogen accumulator (similar in concept to the ring gear drive configuration presented in Huang et al. [27]). Active cylinder piston motion is coupled with passive cylinder piston motion. Lateral pulley translation is transformed into vertical payload motion compensation with pulleys.

Small-scale testing of the system presented by Quan et al. [31], [26] showed a maximum motion attenuation of 59% at 4000 m simulated depth. While the performance of these tests are low compared to a benchmark of approximately 80% for PHC provided by Hatleskog and Dunnigan [33], it should be considered that the compensation depth examined in this work is extreme. Additionally, these results showed an encouraging improvement over strictly PHC tests in the same test environment which indicated maximum motion attenuation of 18%. These tests, therefore, show a threefold improvement in motion attenuation from PHC to semi-active heave compensation.

Semi-active heave compensation methods generally represent an improvement in performance over simple PHC approaches. Semi-active systems are, however, typically used for large-scale drilling applications and at several kilometres depth, meaning that many of the proposed mechanisms are often over-sized for general towing applications. Additionally, the extension and retraction length of systems proposed by Liu et al. [28], Yuan [29], and Quan et al. [31], [26] are limited compared to a winch-based AHC system. While it is possible to add a PHC system to the tow cable of any AHC system to increase robustness, for generality, this thesis will focus on winch-based AHC systems.

## 2.2. CABLE SIMULATIONS

In the work presented by Hover et al. [12], a dynamic cable model is thoroughly explored for a heave compensated towed body application. The two-dimensional equations of motion for marine cables as presented in Hover et al. [12] draw from previous work, such as Howell [34], Irvine[35], and Tyrantafyllou [36] who, collectively, present two and three dimensional non-linear formulations of cable models. Figure 2.11 illustrates a cable element force analysis including shear and moments adapted from Chen et al. [37].

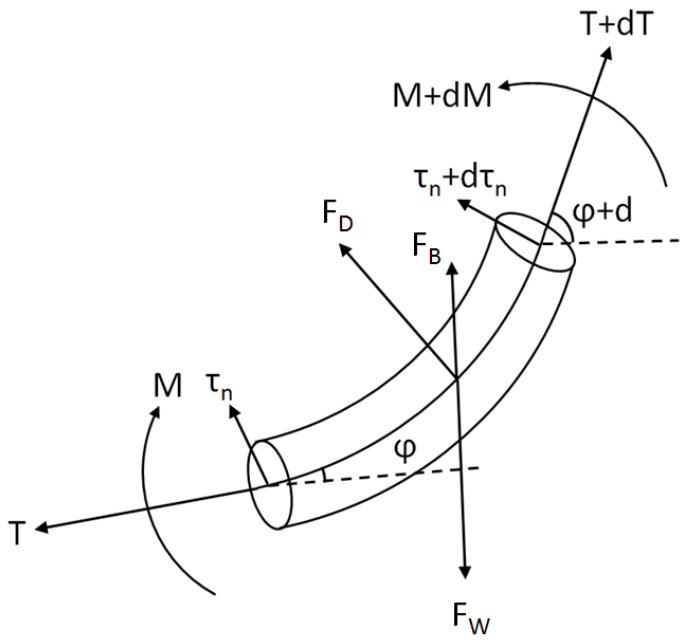


**Figure 2.11: Free body diagram of an elemental segment of a tow cable.**

Nomenclature for Figure 2.11 is presented in Table 2.1.

**Table 2.1: Nomenclature of Figure 2.11.**

| Nomenclature | Symbol |
|---|---|
| Tension | $T$ |
| Moment | $M$ |
| Normal Shear | $\tau$ |
| Cable Pitch Angle | $\varphi$ |
| Cable Weight | $F_W$ |
| Cable Buoyancy | $F_B$ |
| Drag Force | $F_D$ |

Hover et al. [12] reduce the equations of motion into a formulation for a towed body application by neglecting cable torsion, rotational inertia of the cable, and bending stiffness of the cable. Howell [34] justifies such assumptions by considering a two-dimensional cable model configuration and compares induced strains from tension versus curvature. Strain induced by tension is calculated using Equation (2.2) while maximum strain induced by curvature is calculated using Equation (2.3):

$$\varepsilon_T = \frac{T}{EA} \tag{2.2}$$

$$\varepsilon_{C\,Max} = \frac{r_C}{a} \tag{2.3}$$

where $\varepsilon_T$ is tension strain, $T$ is tension, $E$ is the cable modulus of elasticity, $A$ is the cable cross-sectional area, $\varepsilon_{C\,Max}$ is the maximum curvature strain, $r_c$ is the radius of the cable cross-section, and $a$ is the radius of curvature.

When the magnitude of $\varepsilon_T$ is close to $\varepsilon_{C\,Max}$, then:

$$\frac{T}{EA} \cong \frac{r_C}{a} \tag{2.4}$$

Equation (2.4) can then be rearranged to yield:

$$E \cong \frac{Ta}{Ar} \tag{2.5}$$

The maximum binormal bending moment $M$ is calculated in Equation (2.6) for circular cables.

$$M = \frac{E\pi {r_C}^4}{4a} \tag{2.6}$$

Substituting the approximation from Equation (2.5) and the definition of the area of a circle into the calculation of the binormal bending moment produces Equation (2.7).

$$M \cong \frac{Tr_C}{4} \tag{2.7}$$

The shear force, $S$ is then obtained by differentiating the moment along the length of the cable as shown in Equation (2.8):

$$S = \frac{dM}{ds} \cong \frac{Tr_C}{4l_c} = \left(\frac{r_C}{4l_c}\right)T \tag{2.8}$$

where the cable length element is *ds* and $l_c$ represents the characteristic length of change of the cable. In order for equivalent tensile and bending strain to be achieved, the cable radius must be larger than the characteristic length of cable over which the moment is applied, which is physically impossible for a reasonably long tow cable. It is, therefore, evident that static bending is a significant consideration of a cable model only when bending strains are greater than those induced by tension, indicating a "low tension" application.

Hover et al. [12] present Equation (2.9) and Equation (2.10) as the two-dimensional governing equations resulting from their aforementioned simplifications. Nomenclature for Equations (2.9), (2.10), and (2.11) are presented in Table 2.2.

$$m\left(\frac{\partial u}{\partial t} - \frac{\partial \varphi}{\partial t}v\right) = \frac{\partial T}{\partial s} - w_0 \sin\varphi - \frac{1}{2}\rho_w d_C C_t u|u| \tag{2.9}$$

$$m\left(\frac{\partial v}{\partial t} - \frac{\partial \varphi}{\partial t}u\right) + m_a \frac{\partial v}{\partial t} = T\frac{\partial \varphi}{\partial s} - w_0 \cos\varphi - \frac{1}{2}\rho_w d_C C_d v|v| \tag{2.10}$$

It should be noted that two principal analysis techniques of marine cable model exist [38]. The finite difference method (FDM) approximates the governing equations of a cable by difference equations along the cable, using position as a state variable. The finite element method (FEM) discretizes the cable into a finite number of elements along the cable length. While physical parameters for each element may vary throughout the model, the governing equations for each element are the same in FEM, allowing for easier algorithmic computation when it is applicable.

Hover et al. [12] indicate that model linearization was required in order to achieve reasonable computational efficiency of their FDM model at the time their research was conducted. To achieve this linearized model, a small angle approximation is applied, high order terms are removed, and fluid drag is linearized. Bliek's [13] method of forming a

finite-difference transfer matrix in the frequency domain and discretizing the tow cable is then applied. It can be noted that tangential and normal deflection are both included as state variables, and the static component is removed in order to examine only the small dynamic deflections about the static cable configuration.

$$\frac{d}{ds}\begin{bmatrix}\tilde{T}\\ \tilde{\varphi}\\ p\\ q\end{bmatrix}=\begin{bmatrix}0 & w_0\cos\bar{\varphi} & -m\omega^2+i\omega b_p(s) & 0\\ -\frac{1}{\bar{T}}\frac{\partial\bar{\varphi}}{\partial s} & -\frac{w_0\sin\bar{\varphi}}{\bar{T}} & 0 & \frac{1}{\bar{T}}\left(-(m+m_a)\omega^2+j\omega b_q(s)\right)\\ \frac{1}{EA} & 0 & 0 & \frac{\partial\bar{\varphi}}{\partial s}\\ 0 & 1+\frac{\bar{T}}{EA} & -\frac{\partial\bar{\varphi}}{\partial s} & 0\end{bmatrix}\begin{bmatrix}\tilde{T}\\ \tilde{\varphi}\\ p\\ q\end{bmatrix} \quad (2.11)$$

Some of the variables presented in Table 2.2 are modified in Equations (2.9), (2.10), and (2.11). Overbars indicate that the variable represents only the static component, whereas the tilde represents the dynamic component, which is a parameter held constant in simulation. Summation of the static and dynamic components fully describes the variable.

**Table 2.2: Nomenclature for Equations (2.9), (2.10), and (2.11)**

| Nomenclature | Variable |
|---|---|
| Cable Mass/Length | $m$ |
| Cable Tangential Velocity | $u$ |
| Cable Normal Velocity | $v$ |
| Cable Pitch Angle | $\varphi$ |
| Cable Tension | $T$ |
| Cable Water Weight/Length | $w_0$ |
| Water Density | $\rho_w$ |
| Cable Diameter | $d_C$ |
| Cable Tangential Drag Coefficient | $C_t$ |
| Cable Normal Drag Coefficient | $C_d$ |
| Cable Tangential Deflection | $p$ |
| Cable Normal Deflection | $q$ |
| Lagrangian Cable Co-ordinate | $s$ |
| Angular Frequency | $\omega$ |
| Imaginary Variable | $j$ |
| Cable Tangential Linear Damping Coefficient | $b_p$ |
| Cable Normal Linear Damping Coefficient | $b_q$ |
| Modulus of Elasticity | $E$ |
| Cable Cross-sectional Area | $A$ |

Driscoll et al. [39] pursue a finite element approach with a lumped-mass cable model to study ROV cage displacement. Because this problem is principally vertical, the model formulation is simplified to a one-dimensional case. Some simplifications were made concerning complex fluid interactions, such as the time history of vortices acting about the ROV cage influencing the ROV's added mass effect. The mass matrix parameters are lumped along the matrix horizontal, decoupling acceleration terms and simplifying computation. The FEM formulation of the *N* second-order differential equations that govern the vertical tethered system are constructed into Equation (2.12) with internal forces arranged on the left-hand side and external forces on the right-hand side. Nomenclature for Equations (2.12) through (2.16) is presented in Table 2.3. The subscript *i* indicates the $i^{\text{th}}$ cable element.

$$\boldsymbol{M}\ddot{z} + \boldsymbol{K}u = f \tag{2.12}$$

From applying the lumped-mass approximation, the diagonal mass matrix is presented in Equation (2.13) as follows:

$$\boldsymbol{M} = \frac{1}{2}\begin{bmatrix} 0 & m_1 l_1 + m_2 l_2 & 0 & \cdots & 0 & 0 \\ 0 & 0 & m_2 l_2 + m_3 l_3 & \cdots & 0 & 0 \\ \vdots & \vdots & \vdots & \ddots & \vdots & \vdots \\ 0 & 0 & 0 & \cdots & m_{N-1} l_{N-1} + m_N l_N & 0 \\ 0 & 0 & 0 & \cdots & 0 & m_N + 2M_{CG} + 2M_{ROV} \end{bmatrix} \tag{2.13}$$

The tridiagonal stiffness matrix is then presented in Equation (2.14):

$$\boldsymbol{K} = \begin{bmatrix} -\frac{E_1 A_1}{l_1} & \frac{E_1 A_1}{l_1} + \frac{E_2 A_2}{l_2} & -\frac{E_2 A_2}{l_2} & \cdots & 0 & 0 \\ 0 & -\frac{E_2 A_2}{l_2} & \frac{E_2 A_2}{l_2} + \frac{E_3 A_3}{l_3} & \cdots & 0 & 0 \\ \vdots & \vdots & \vdots & \ddots & \vdots & \vdots \\ 0 & 0 & 0 & \cdots & \frac{E_{N-1} A_{N-1}}{l_{N-1}} + \frac{E_N A_N}{l_N} & -\frac{E_N A_N}{l_N} \\ 0 & 0 & 0 & \cdots & -\frac{E_N A_N}{l_N} & \frac{E_N A_N}{l_N} \end{bmatrix} \tag{2.14}$$

And finally, the forcing vector is presented in Equation (2.15)

$$f = \begin{bmatrix} f_1^{(2)} + f_2^{(1)} \\ f_2^{(2)} + f_3^{(1)} \\ \vdots \\ f_{N-1}^{(2)} + f_N^{(1)} \\ f_N^{(2)} + f_{CG}^{(1)} \end{bmatrix} \tag{2.15}$$

With the external hydrodynamic, gravitational, and buoyancy forces at side $k$ (where $k = 1$ for the upper side and $k = 2$ for the lower side) of node $i$ are included in the model presented in Equation (2.16).

$$\begin{aligned} f_i^{(k)} = {} & \frac{1}{2}(m_i - \rho_w A_i) g l_i - \frac{1}{2}\rho_w D_i C_{DT}^i l_i \\ & \times \left[\frac{1}{3k}\left(\dot{Z} + \dot{u}_i^{(1)}\right)\left|\dot{Z} + \dot{u}_i^{(1)}\right| + \frac{k}{6}\left(\dot{Z} + \dot{u}_i^{(2)}\right)\left|\dot{Z} + \dot{u}_i^{(2)}\right|\right. \\ & \left. - \frac{1}{12}\left(\dot{u}_i^{(1)} - \dot{u}_i^{(2)}\right)\left|\dot{u}_i^{(1)} - \dot{u}_i^{(2)}\right|\right] \end{aligned} \tag{2.16}$$

**Table 2.3: Nomenclature for Equations (2.12) through (2.16)**

| Nomenclature | Variable |
|---|---|
| Cable Mass/Length | $m_i$ |
| Cable Segment Length | $l_i$ |
| Virtual Mass of Cage | $M_{CG}$ |
| Virtual Mass of ROV | $M_{ROV}$ |
| Modulus of Elasticity | $E_i$ |
| Cable Cross-sectional Area | $A_i$ |
| Acceleration of Gravity | $g$ |
| Cable Diameter | $D_i$ |
| Cable Tangential Drag Coefficient | $C_{DT}^i$ |
| Distance from Mean Sea Surface to Top Cable Element | $Z$ |
| Cumulative Elastic Displacement to Node $p$ | $u_i^p$ |

Next, the $N$ second-order differential equations are presented as $2N$ first-order equations. Model simulation was then carried out with a fourth/fifth order Runge-Kutta integration method. The model is validated against data of real ROV cage motion and cable tension. Excellent agreement was found. A spectral analysis of the model response within the expected wave band (0.1 Hz to 0.25 Hz) reveals a maximum disagreement of 7%.

Another cable model is presented in the work of Wu and Chwang [40], who propose an active towed body design and create a hydromechanical model to investigate towed body behaviour. The towed system consists of an actively maneuvered depressor tethered to a vessel through a primary cable. A towed body is tethered to the primary cable behind the depressor by a secondary cable. The configuration is depicted in Figure 2.12. The model of the towed system includes six DOF considerations for the hydromechanical forces on the depressor and towed body. Additionally, boundary conditions on the secondary cable are more complex than previously described work due to the secondary and primary cable interacting dynamically. A FDM approach is used to carry out the simulation.

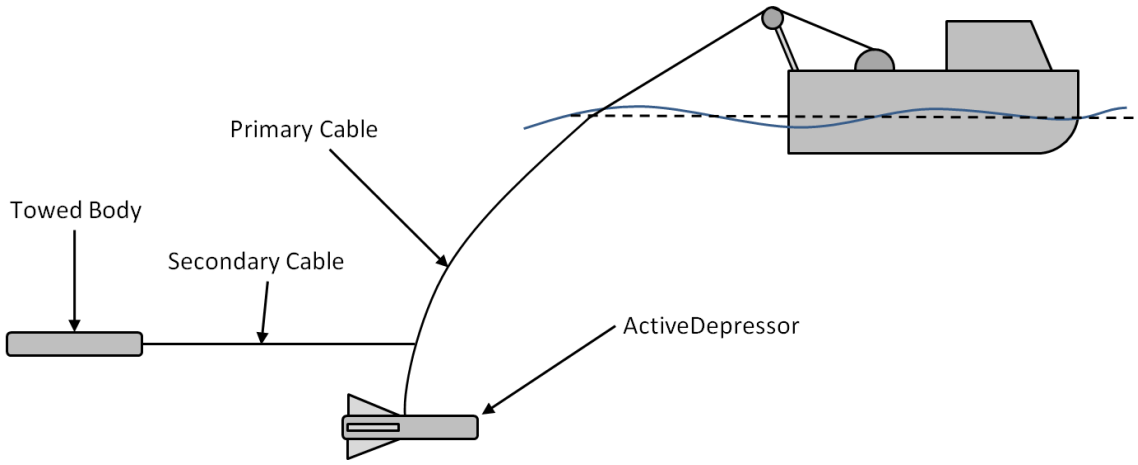


**Figure 2.12: AHC of a two part towed system consisting of a maneuverable depressor and a towed body.**

Additional cable models have investigated rotational cable deformation by applying beam theory. Some early work throughout the 1970s and 1980s was conducted by Reissner [41], Simo and Vu-Quoc [42], Cardona and Geradin [43], and Ablow and Schechter [44]. The benefit of a beam approach is that it can be applied to cable systems with low tension to model rotational effects when rotational strain is significant. When considering the governing equations of the cable, shear forces and moments are not neglected.

The work of Park et al. [45] describes the development and validation of a three-dimensional model of an unloaded cable using a FDM for a towed application. This model is validated under static conditions as well as during constant oscillatory motion of the fixed end. To overcome non-linear and coupling problems, a Newton-Raphson

iteration method is applied and FDM is used. Once drag coefficients are adjusted to account for vortex induced vibrations, good agreement between the simulator and experimental results is realized. Park et al. [45] indicate that this model can be applied for a towed system in order to increase the model robustness in a case of low tension, such as a shallow tow with low velocity.

Many tow cable models presented in the literature are based on a similar description of the forces on an elemental segment of the cable presented in Figure 2.11. Differences arise between cable models as a result of simplifications which are made regarding shear forces and rotational strain, the number of dimensions which are required to accurately describe the system, linearization of forces, and boundary conditions for cable endpoints. In the full-scale analysis which is presented in this thesis, the cable model is presented as a three-dimensional system with quadratic drag forces acting on the cable segments. It is assumed, however, that the full-scale towed applications simulated in this thesis are not "low tension" and as such, rotational stresses are not modeled.

## 2.3. SUMMARY

Various heave compensation methods have been explored in the literature. The majority of AHC and semi-active heave compensation systems are currently used in offshore drilling applications and in ROV cage stabilization. PHC literature is more common with respect to towed systems, such as Hover et al.'s [12] analysis of two PHC methods. Unfortunately, PHC is shown to be a less effective approach than AHC [33]. For towed applications which require better motion attenuation, an AHC system should be pursued. As mentioned in Chapter 1, an AHC design for a towed system is complex, as a purely vertical AHC solution is no longer sufficient. In order to apply the AHC systems explored in this chapter to a towed case, a set-point algorithm must be designed for the winch controller to track. The design of a set-point algorithm for AHC of towed bodies is, therefore, a key objective of this thesis.

Full-scale experimental testing of towed cable systems is expensive; a small-scale or simulated test environment is preferable for proof-of-concept work. Drawing from simulated cable models and towed systems discussed in this chapter, a computer

simulator of a towed system is developed to explore the set-point algorithm's performance over a range of test conditions. This computer simulator is validated using small-scale test data. Finally, an additional computer simulator is developed for a full-scale towed system so that a range of full-scale test conditions can be explored. It is a key objective of this thesis to perform simulation tests and small-scale experimental tests of the proposed set-point algorithms.

# CHAPTER 3 SET-POINT ALGORITHM DEVELOPMENT

This chapter first describes the development of two different set-point algorithms and how they are implemented by either measuring the sheave angle in real-time or assuming a constant, nominal value from the towed system's steady-state. The development of these set-point algorithms meets the first key objective of this thesis. The set-point algorithms are presented in Section 3.1. Next, Section 3.2 outlines small-scale experimental tests used to compare the different set-point algorithms, discusses results of these tests, and finally draws conclusions from the results. Small-scale tests in Dalhousie's Aquatron Lab flume tank were carried out to experimentally compare the performance of the set-point algorithms. An AHC system was developed for the flume-scale tests using a test mechanism to provide ship disturbance motions and a small electric motor to reel tow cable in and out. System identification work was conducted to derive a dynamic model of the electric winch motor to design a closed-loop PD controller in Simulink. System identification work and controller design is presented in Section 3.3. Next, Section 3.4 explains the metric by which the different set-point algorithms are compared to assess their relative performance and presents and discusses results from the experimental tests. Finally, Section 3.5 summarizes the experimental test results, contributing towards the second and third key objectives of this thesis.

## 3.1. SET-POINT ALGORITHMS

In order to apply an AHC system, some manner of set-point algorithm is required to provide a target cable length to reel in or out. The AHC winch controller then tracks this set-point to provide heave compensation for the towed system. This section discusses the formulation of the two principle set-point algorithms which are employed in this thesis and which have been developed in the author's previous work [46]. The set-point algorithms were developed assuming that the only sensors available at sea are IMU sensors on the surface vessel to measure the vessel's motion, a winch encoder to measure the length of cable that has been reeled in or out, and a sensor to measure the sheave angle of the tow cable as it leaves the sheave to enter the water. While it is possible to equip the towed body with IMU sensors to report its location underwater for additional controller feedback, this towed body motion information is generally not available or

feasible to acquire. Section 3.1.1 describes the Waterline set-point algorithm, which computes a set-point value based on the length of tow cable crossing the static waterline. Section 3.1.2 describes the Sheave set-point algorithm, which computes a set-point value based on sheave motion. Section 3.1.1 and Section 3.1.2 are divided into two sections each, which derive specific formulae adapted for the presence or absence of sensory equipment capable of measuring the towed system's sheave angle in real-time.

### 3.1.1. Waterline Set-Point Algorithm

Figure 3.1 depicts the Waterline set-point algorithm. The Waterline algorithm compensates for unwanted towed body motion by reeling the tow cable in or out to ensure that the same point along the tow cable always crosses the static water level.

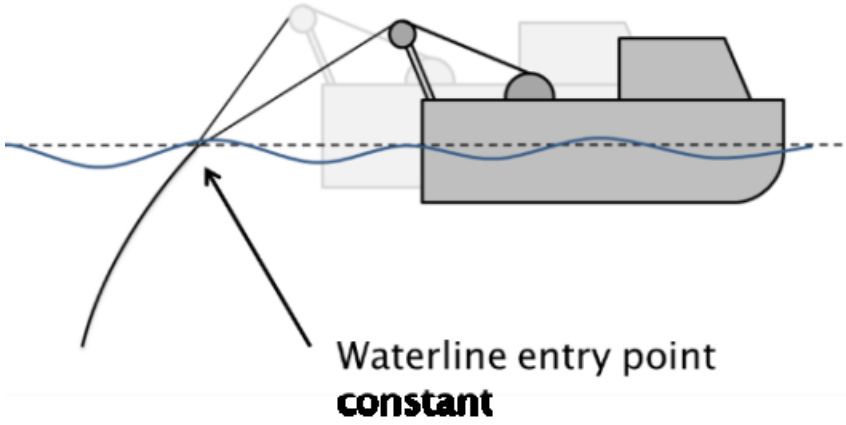


**Figure 3.1: Waterline algorithm maintaining a constant water entry point along the tow cable.**

Two approaches to this algorithm are defined. The first approach measures the sheave angle in real-time, while the other assumes that sheave angle variance remains sufficiently small that it can be assumed that the sheave angle is a constant nominal value. When the sheave angle is measured in real-time, the set-point algorithm is defined as being "Rigorous," and the full description of the set-point algorithm is the Rigorous Waterline algorithm. Conversely, when the sheave angle is assumed to be as a constant value, the algorithm is "Simplified" and the set-point algorithm is fully described as the Simplified Waterline algorithm.

### 3.1.1.1. Simplified Waterline Set-Point Algorithm

Figure 3.2 depicts the Simplified Waterline algorithm. With this set-point algorithm, the surface vessel's motion is measured. The vertical position of the sheave above the waterline is referred to as *Height*. The *Height* can be calculated from IMU data. The exact value of the sheave angle $\theta$ is not measured, and as a result, the exact length of exposed tow-line length cannot be determined. For this case, a nominal sheave angle is used to calculate the amount of tow cable exposed above the mean waterline. The winch controller can ensure that the same point along the cable enters the water, which provides heave compensation to the towed body.

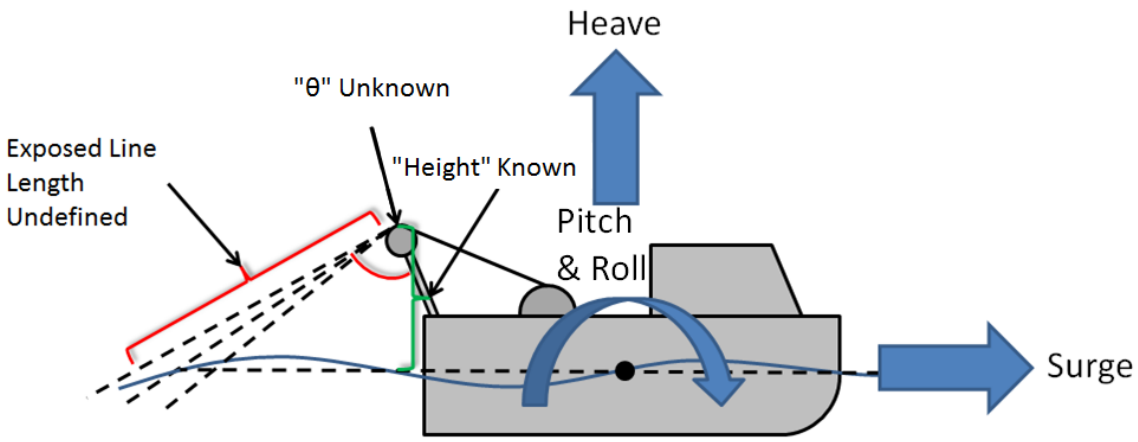


**Figure 3.2: Simplified Waterline set-point algorithm.**

Equation (2.5) describes the computation of the winch control loop set-point for the Simplified Waterline algorithm, where *SP* is the winch system set-point and the subscript *nom* indicates nominal values (when the vessel is operating in steady conditions).

$$SP = \frac{Height}{\cos\theta_{nom}} - \frac{Height_{nom}}{\cos\theta_{nom}} \tag{3.1}$$

### 3.1.1.2. Rigorous Waterline Set-Point Algorithm

Figure 3.3 illustrates the Rigorous Waterline algorithm in which the actual sheave angle is measured in real-time. In this case, both the sheave height and sheave angle are known. Knowing both the sheave height and sheave angle enables the exposed line length to be

fully defined and used by the winch controller to ensure that the same point along the cable enters the water.

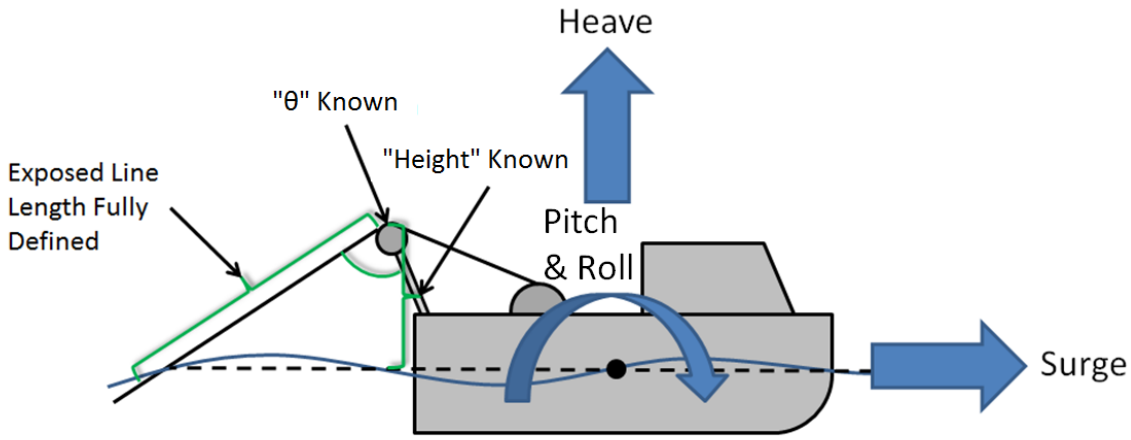


**Figure 3.3: Rigorous Waterline set-point algorithm.**

Equation (3.2) describes the computation of the winch control loop set-point for the Rigorous Waterline algorithm.

$$SP = \frac{Height}{\cos\theta} - \frac{Height_{nom}}{\cos\theta_{nom}} \tag{3.2}$$

### 3.1.2. Sheave Set-Point Algorithm

Figure 3.4 depicts the Sheave set-point algorithm. The Sheave algorithm determines the desired cable adjustment length based on the motion of the vessel's sheave projected along the tow cable.

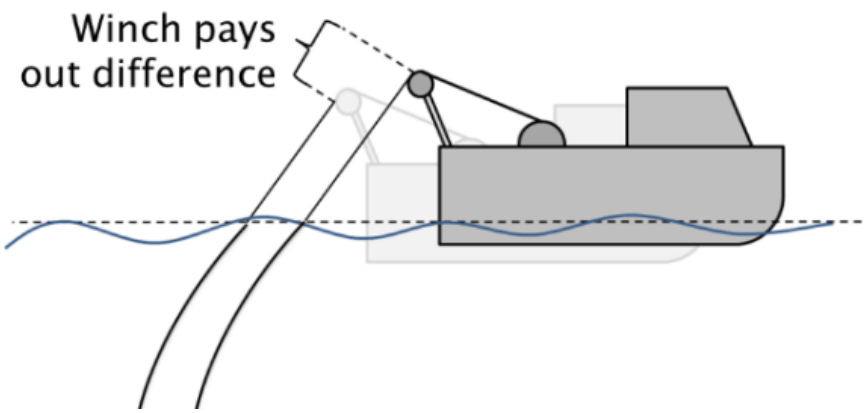


**Figure 3.4: Sheave algorithm determines the desired cable adjustment based on the motion of the vessel's sheave projected along the tow cable.**

As with the Waterline algorithm, Rigorous and Simplified approaches are defined for the Sheave algorithm. The Simplified approach again assumes that changes in sheave angle are relatively small and that the sheave angle can be approximated as a nominal value. The Rigorous approach measures the sheave angle in real-time for feedback into the set-point algorithm.

#### 3.1.2.1. Simplified Sheave Set-Point Algorithm

Figure 3.5 depicts the Simplified Sheave algorithm. For this case, the tow cable angle is unknown and a nominal tow cable angle is assumed. The resulting displacement of the sheave in the vertical and horizontal directions is measured relative to the nominal, undisturbed position of the sheave. The sheave disturbance can then be projected along the tow cable to determine the amount of cable that needs to be reeled in or out by the winch.

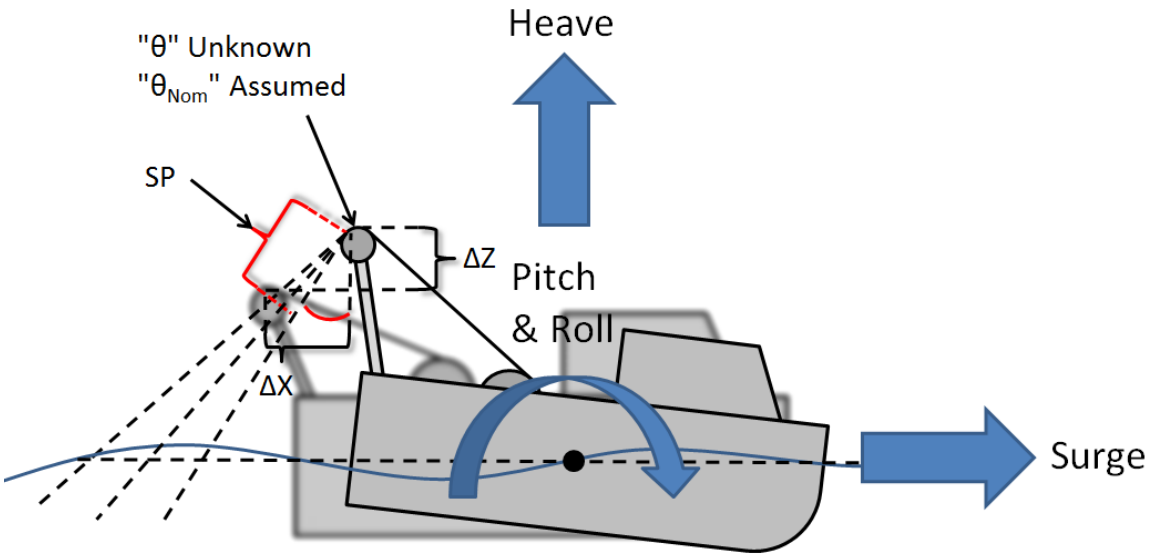


**Figure 3.5: Simplified Sheave set-point algorithm.**

Equation (3.3) describes the computation of the winch control loop set-point for the Simplified Waterline algorithm, where $\Delta x$ and $\Delta z$ indicate the displacement of the host vessel sheave from its nominal position along the $x$ and $z$ axes, respectively. $SP$ is then calculated by projecting this displacement along the assumed location of the tow line, determined using $\theta_{nom}$.

$$SP = (\Delta x)\sin(\theta_{nom}) + (\Delta z)\cos(\theta_{nom}) \tag{3.3}$$

### 3.1.2.2. Rigorous Sheave Set-Point Algorithm

Figure 3.6 illustrates the Rigorous Sheave method in which, similar to the Rigorous Waterline method, the tow-line angle is measured in real-time. As a result, the displacement of the sheave can be projected onto the actual tow cable to determine the accurate set-point that the winch controller needs to track.

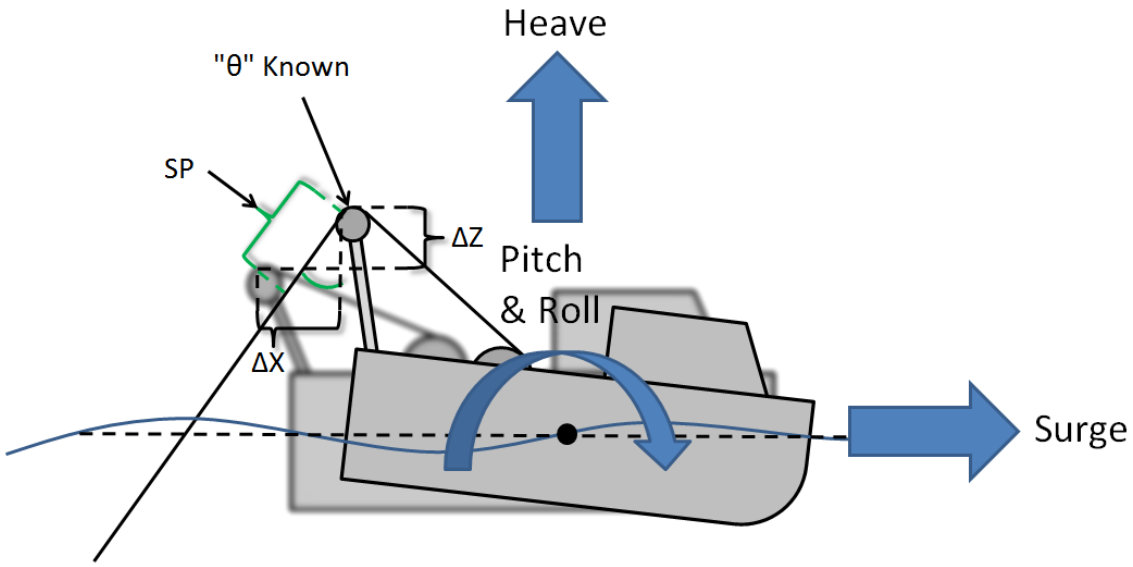


**Figure 3.6: Rigorous Sheave set-point algorithm.**

Equation (3.4) describes the computation of the winch control loop set-point for the Rigorous Sheave algorithm.

$$SP = (\Delta x)\sin(\theta) + (\Delta z)\cos(\theta) \tag{3.4}$$

In order to empirically assess the performance of the different reference methods described in Section 3.1, a set of small-scale experimental test were conducted. These small-scale tests were designed to emulate the effects of unwanted ship motion on a generalized spherical towed body.

## 3.2. FLUME-SCALE TEST ENVIRONMENT

This section will outline the test equipment and methods which were used to perform the flume-scale set-point algorithm tests. Figure 3.7 shows a three-dimensional schematic of the flume-scale test environment.

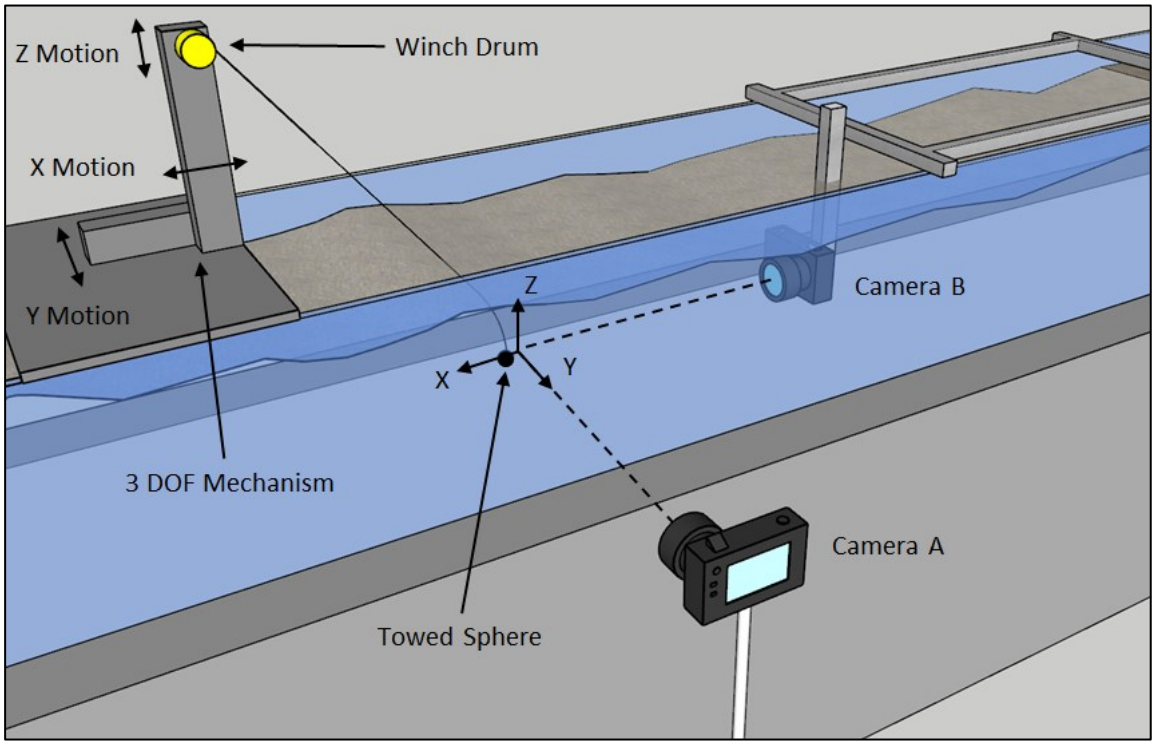


**Figure 3.7: Diagram of the test apparatus.**

The test apparatus is positioned over a recirculating flume water tank. Constant flow from the flume tank produces a drag force on a submerged tow cable and towed body, represented with thin nylon tow cable and a towed sphere. A three DOF Cartesian mechanism translates a powered winch drum in the *x*, *y*, and *z* directions to follow a pre-recorded motion path simulating wave disturbance of a host vessel's sheave. The powered winch is commanded to either reel in or out the tow cable in accordance with the set-point algorithm which is under examination. A winch motor encoder provides feedback for closed-loop control. Additionally, an absolute encoder is mounted to the exterior of the winch drum which provides measurement of the current sheave angle, for comparison of rigorous and simplified set-point algorithm approaches. The entire test rig, including the winch, translating mechanism, and absolute sheave angle encoder, is controlled by a MyRIO microcontroller operating in a control loop at a 1 kHz rate. Displacement of the sphere is recorded by two cameras. One camera is positioned perpendicular to the flume tank flow, filming through the transparent acrylic wall. The second camera is submerged into the flume tank, fixed to an aluminum frame and facing into the flow. From these two cameras, a three-dimensional trace of the sphere's position over time can be recreated.

The sphere trace which is produced can be analyzed to determine the extent of induced towed body motion. The flume tank flow profile is measured with an acoustic profiler. Finally, a Cartesian co-ordinate system for the test environment is adapted from the ship motion diagram in Figure 1.6. This test environment co-ordinate system is depicted in Figure 3.7. An origin is located at the intersection of the center of both cameras' field of view. This co-ordinate system is used to compute the relative distances between test equipment in order to extract the correct displacement of the sphere from collected footage.

### 3.2.1. Flume Tank

Dalhousie University's Aquatron Lab contains a flume tank which was used to facilitate the flume-scale tests. The flume tank is pictured in Figure 3.8.

**Figure 3.8: Dalhousie Aquatron lab's flume tank with aluminum camera mounting frame.**

The flume tank has a 0.5 m by 0.5 m cross-section and is approximately 7.3 m long. The flume tank flow speed is adjustable. For the set of tests which were carried out, the tank was run at a surface flow speed of 0.33 m/s.

A Vectrino Doppler velocimeter [47] was used to measure the flow profile of water within the flume tank. As shown in Figure 3.8, the Vectrino sensor was mounted to an aluminum frame at various depths to record the flume tank flow speed over a two minute period.

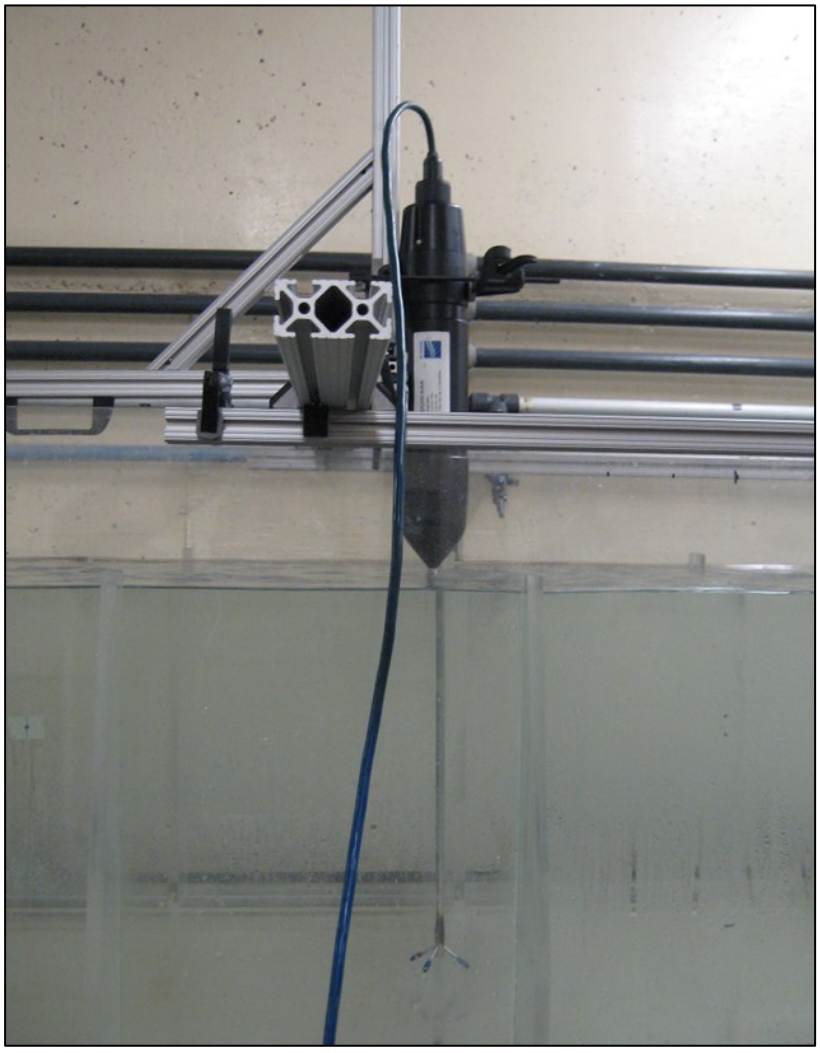

**Figure 3.9: Vectrino Doppler velocimeter in the flume tank.**

The Vectrino profiler measures flow as a three dimensional vector. A rotation is applied to the Vectrino data in order to align the measurements with the world frame of the test

environment. In accordance with the reference frame depicted in Figure 3.7, flow along the *x* axis is parallel to the flume tank flow. Net flow in the *y* and *z* direction is zero. The flow profile constructed from *x* direction flow was used to replicate the test conditions in simulation. From the data which were collected, an estimate of flow variance was measureable. This value was associated with flow turbulence and used to produce an approximation of the turbulence imposed on the towed system in simulation.

### 3.2.2. Flume-Scale Towed System

Static tow cable shape can be influenced by hydromechanical forces and gravitational forces. When selecting an appropriate size for the flume-scale towed system and flow speed for flume-scale testing, a reasonable approximation of a full-scale system tow cable shape was desired. Figure 3.10 was based on results of Sun et al. [38] and shows sub-sea tow cable shapes at different vessel speeds for a 460 m length of cable using a specific towed body and tow cable. The vertical axis of Figure 3.10 represents the depth of the tow cable beneath the waterline and the horizontal axis represents the distance of the tow cable behind the ship stern.

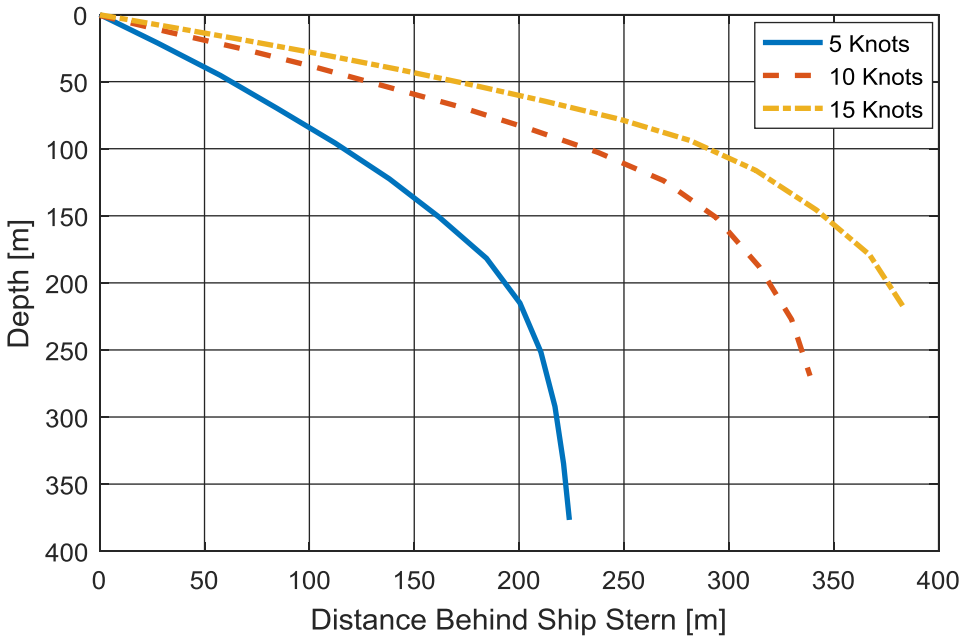


**Figure 3.10: Tow cable shapes for 460 m of cable at various tow speeds [38].**

A range of tow line shapes can be observed in Figure 3.10 – all exhibiting some extent of downward curvature. An approximate representation of this downward curvature was qualitatively replicated in the flume tank experiments by selecting an appropriate tow cable and towed body substitute for the flume tank depth and flow speed.

Dimensional analysis was carried out to ensure that the towed system parameters are properly scaled. Quan et al. [26] describe their method of sizing a small-scale ROV system using the Froude criterion. The Froude number of a system can be used to provide a scaling factor for various model parameters, providing similarity between systems if it is held constant between the original and scaled systems. Equation (3.5) shows the equality which must be satisfied in order for the Froude criterion to be met:

$$\frac{\lambda_v^2}{\lambda_g \lambda_l} = 1 \tag{3.5}$$

where $\lambda$ indicates a ratio of the prototype system parameter to the flume-scale model parameter, $\lambda_v$ is the velocity ratio, $\lambda_g$ is the ratio of gravitational fields, and $\lambda_l$ is the ratio of characteristic length.

As described in Quan et al. [26] Equation (3.6) expresses towed body mass as a scale factor:

$$\frac{\lambda_m}{\lambda_\rho \lambda_l^3} = 1 \tag{3.6}$$

where $\lambda_\rho$ is the ratio of fluid densities and $\lambda_m$ is the ratio of towed body mass.

A 101 cm length of monofilament nylon line was selected as a substitute for a tow cable in the small-scale tests, as its diameter and drag characteristics were agreeable in the range of speeds attainable in the flume tank. For the towed body, a 10 mm diameter sphere weighing 1.33 g was used so that a simple and classical solution could be analyzed without the additional complexities associated with towed body dynamics arising from more complex towed body geometry. A towed sphere is also studied by Kamman and

Huston [48] as a generalized representation of a towed body. Figure 3.11 shows the tow cable and sphere in the flume tank and the tow cable shape.

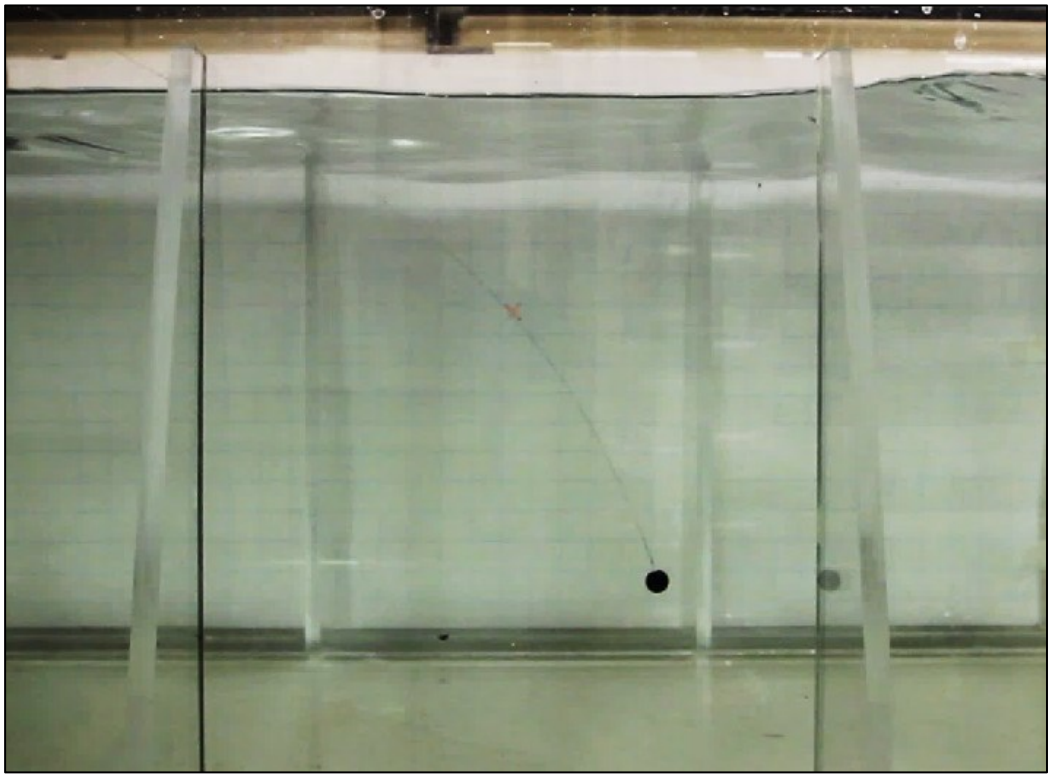

**Figure 3.11: Tow cable and towed sphere.**

The flume-scale parameters are compared to an imagined full-scale towed system to verify the Froude criteria listed in Equations (3.5) and (3.6). The full-scale towed body mass was taken as 3250 kg with a 125 m length of tow cable, similar to the system described by Sun et al. [38]. Full-scale mean ship velocity is taken from an Australian Defence Science and Technology Organisation (DSTO) report [49] as 3.66 m/s. The surface flume tank flow speed of 0.33 m/s is used as an approximation of flume-scale flow speed, as the towed system is often reasonably far from the bottom of the tank where the flow speed is lower. Table 3.1 contains a list of all the full-scale and flume-scale towed system parameters along with the relevant parameter scaling factors, $\lambda$.

**Table 3.1: Flume-scale and full-scale towed system parameters.**

| Parameter | Full-Scale | Flume-scale | $\lambda$ |
|---|---|---|---|
| Tow Cable Length | 125 m | 1.01 m | 123.8 |
| Relative Flow Velocity | 3.66 m/s | 0.33 m/s | 11.1 |
| Towed Mass | 3250 kg | 0.00133 kg | 2443609 |
| Gravity Field | 9.81 m/s$^2$ | 9.81 m/s$^2$ | 1 |
| Seawater Density | 1026 kg/m$^3$ | 1026 kg/m$^3$ | 1 |

Equations (3.5) and (3.6) are now used to evaluate the flume-scale parameters.

$$\frac{\lambda_v^2}{\lambda_g \lambda_l} = \frac{11.1^2}{123.8} = 0.99 \cong 1 \tag{3.7}$$

$$\frac{\lambda_m}{\lambda_\rho \lambda_l^3} = \frac{2443609}{123.8^3} = 1.29 \cong 1 \tag{3.8}$$

It should be noted that while 1.29 might not appear to be approximately equivalent to 1, perfect equivalence of Equation (3.8) would correspond to a full-scale tow cable length of 136 m, which is only 9% longer than the full-scale length of 125 m. From the approximate equivalences observed in Equations (3.7) and (3.8), the Froude criterion is upheld for the stated towed system parameters when compared to a full-scale towed system.

Following the selection of materials and the test environment, ship perturbation was investigated so that the flume-scale test-rig could replicate realistic ship motion.

### 3.2.3. Simulated Ship Motion

The three DOF test mechanism uses rack and pinions mounted in orthogonal directions to produce repeatable tow-point motion. The test rig has a maximum range of motion of ±4 cm in each direction and is actuated with several small 12 V motors. No datasheet or model number is available for the motors which were used to actuate the test rig, but the motor parameters are explored later.

Ship motion data were digitized from the Australian DSTO report [49] in order to obtain a representative motion path over which to translate the test rig winch. The ship displacement motion included effects from all six DOF. The data were then resolved into three translational degrees of freedom for a sheave located at the ship's stern. Motion was next scaled down to fit within the test mechanism's motion envelope. Figure 3.12 shows the resulting *x, y*, and *z* axis motion. The vertical figure axis represents displacement, while the horizontal figure axis represents the passage of time. For each flume tank trial, the test apparatus winch tracked the motion path presented in Figure 3.12.

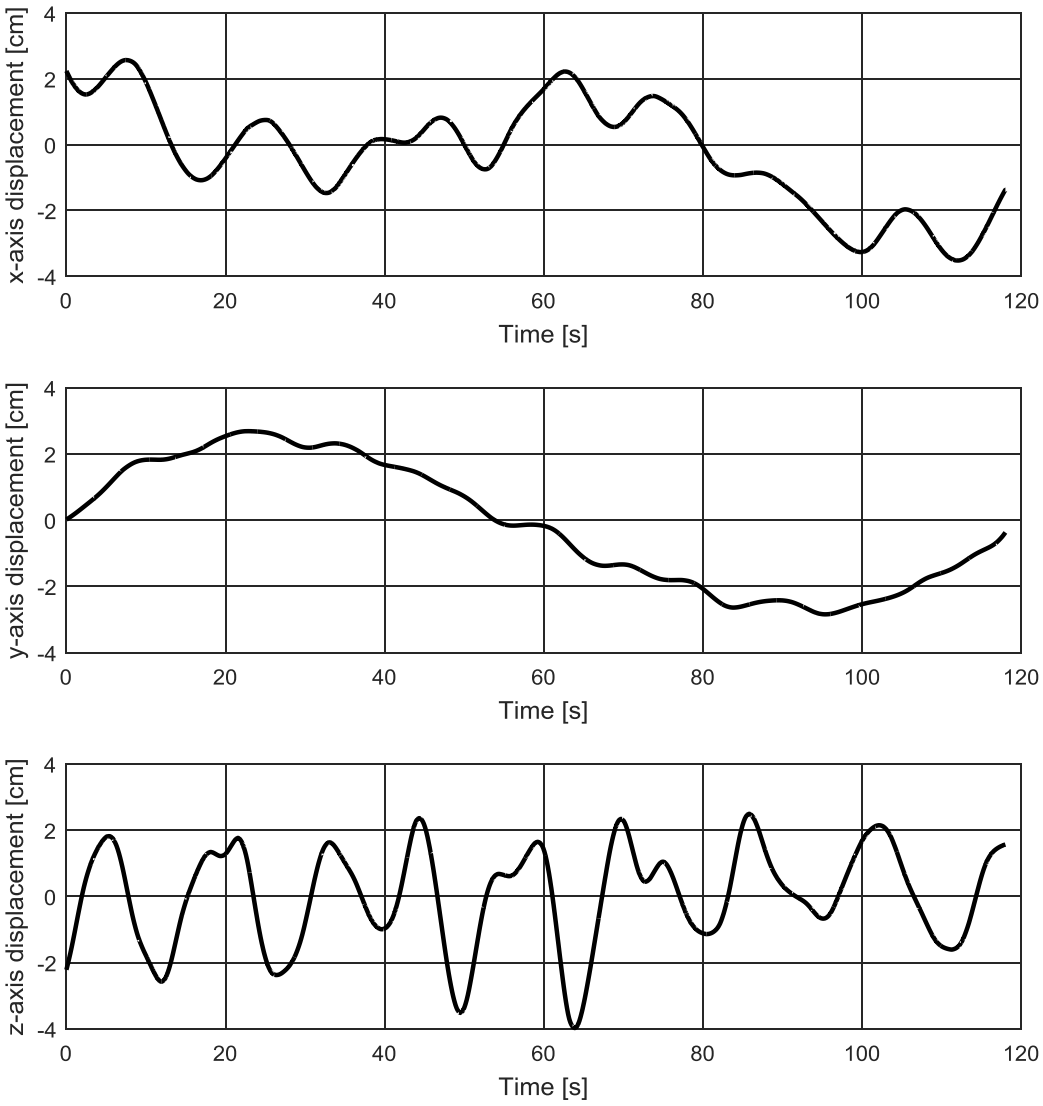


**Figure 3.12: Digitized and rescaled ship motion from DSTO report.**

The test apparatus displacement repositions a powered winch, controlled in closed-loop by a PD controller. The rigorous set-point algorithms used by this controller require that the sheave angle is measured in real-time.

### 3.2.4. Sheave Angle Measurement

The output of Rigorous set-point algorithms is a function of the sheave angle. To measure the sheave angle, a device was constructed which senses the sheave angle and measures it in real-time using a non-contact absolute encoder. An AEAT-6012-A06 12-bit magnetic encoder [50] was used for the test rig. Figure 3.13 displays the sheave angle measurement device.

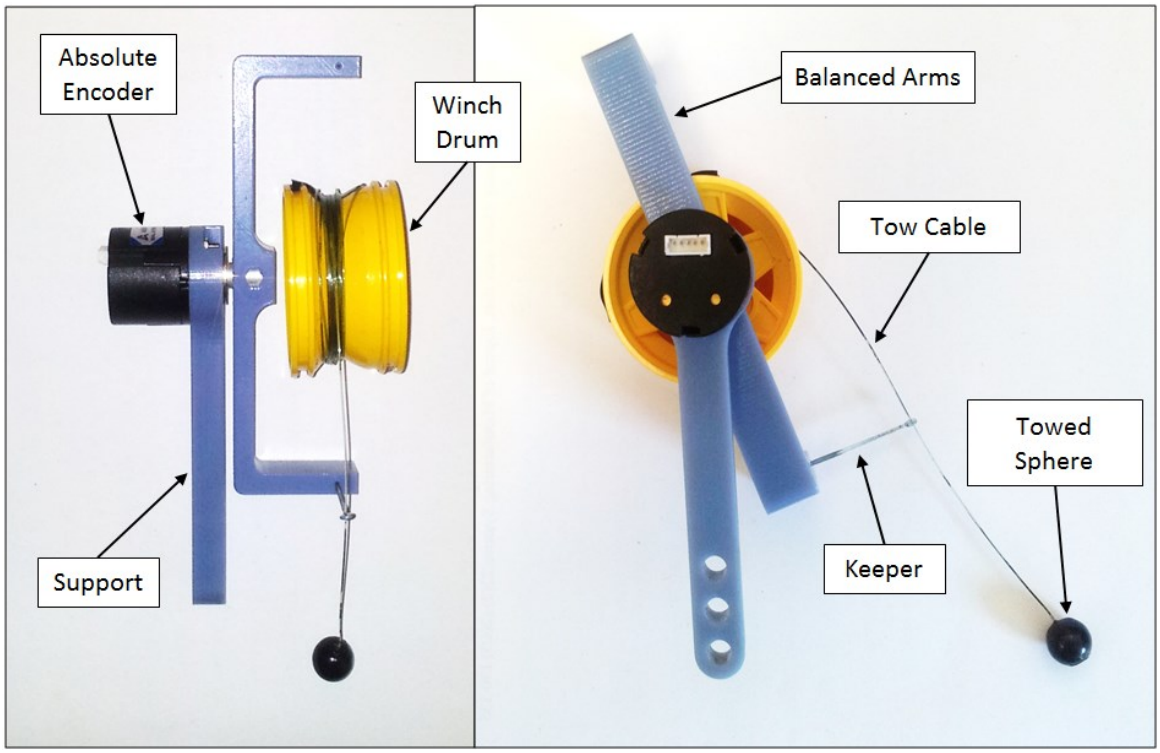


**Figure 3.13: Sheave angle measurement device.**

The sheave angle measurement device depicted in Figure 3.13 has a support structure which is connected to the translating mechanism. The absolute encoder is also fixed to the vertical support. The shaft of the encoder is co-linear with the winch shaft and free to spin relative to the support structure and the winch drum. The encoder shaft is fixed to a balanced set of arms which extend around the winch drum. Connected to one of the arms

is a light, plastic tow cable keeper. The keeper is a thin rod with an eye (like a needle) at the end. Figure 3.14 shows an image of the keeper. The tow cable passes through the eye. As the angle of the tow cable changes, the keeper is adjusted and rotates the arms and thus the encoder shaft.

**Figure 3.14: Sheave angle measurement device keeper**

In addition to real-time data collection for winch control and heave compensation, data were collected to analyze the performance of the set-point algorithms.

### 3.2.5. Towed Body Motion Capture

To film the displacement of the sphere over time, two cameras were positioned such that the centre of their field of view intersected orthogonally. The cameras were level, meaning that the bottom of their field of view was parallel with the floor of the flume tank. Figure 3.15 shows the layout of the two cameras.

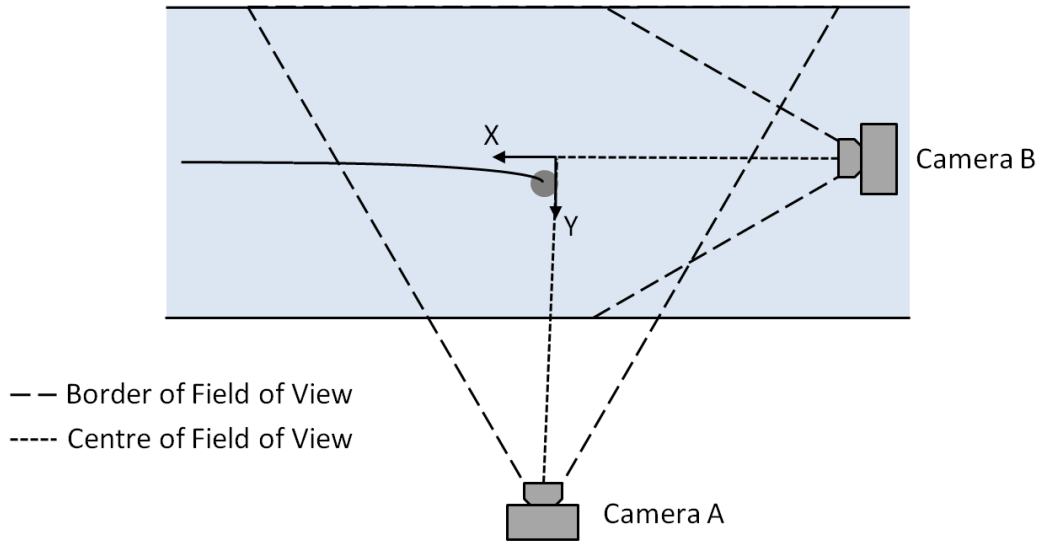


**Figure 3.15: *x-y* planar view of the flume test area.**

Figure 3.15 depicts the *x-y* planar view of the test area. The intersection of the centre of the two camera fields of view is the origin for the test environment. Camera A is a Canon EOS 7D [51] mounted on a tripod. Camera B is a GoPro Hero 3+ [52] attached to an aluminum frame for rigid support in the flume tank flow. Figure 3.16 is an image of the two test environment cameras and the aluminum support structure. The centre of the cameras' fields of view is indicated with a dotted line and the test environment origin and axes are depicted.

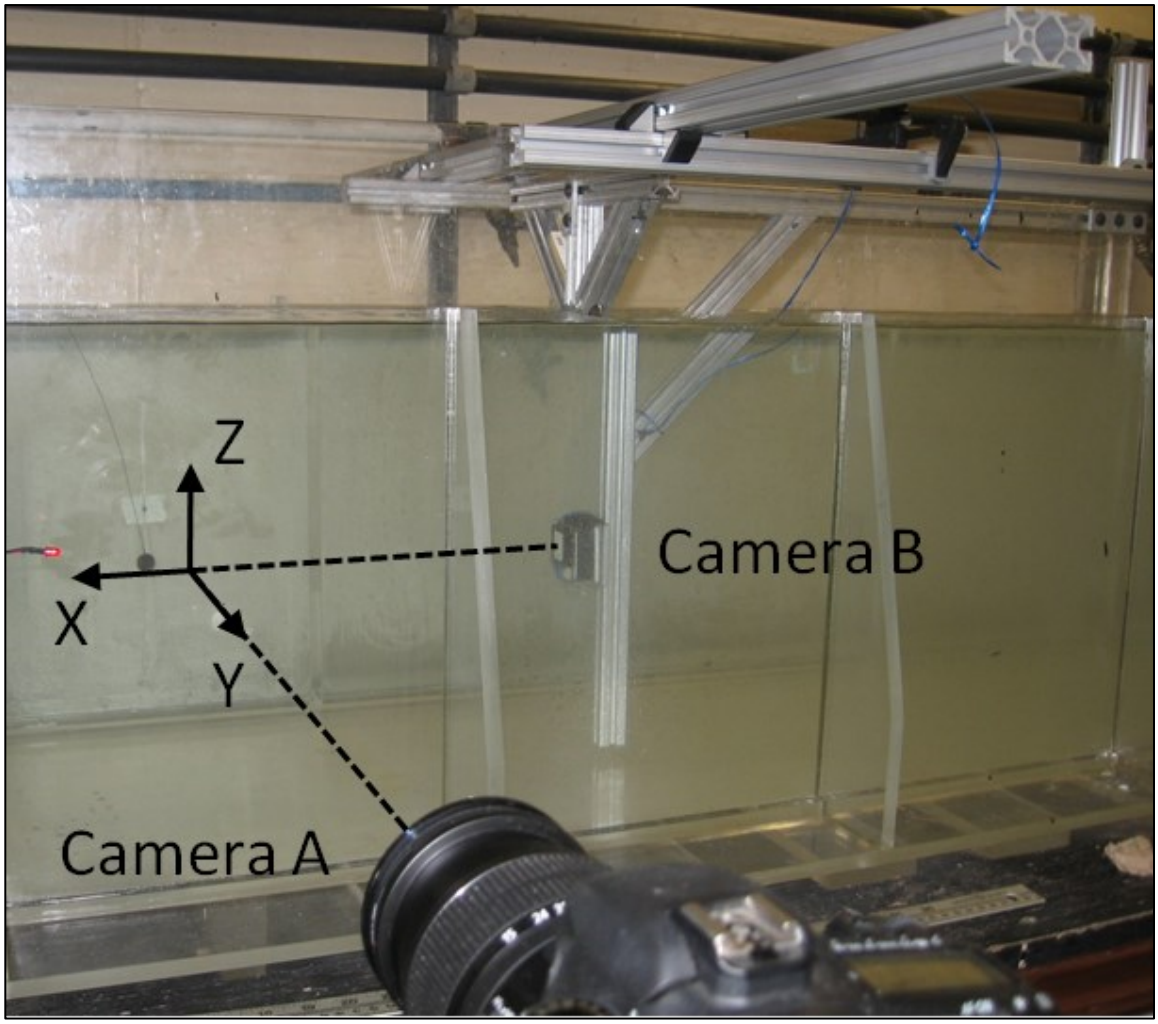


**Figure 3.16: Camera A and Camera B in the flume tank.**

The location of the test environment origin is 18.5 cm from the bottom of the flume tank. For the tests which are examined in this thesis, the nominal position of the winch is (51, 0, 63.9) cm and the nominal length of tow cable is 101 cm.

Once footage is collected by the two cameras, it is deconstructed into constituent frames in MATLAB. Five frames per second are maintained and stored for analysis. The images are converted to black-and-white and an object-finding function is used to detect the location of the sphere within the field-of-view of both cameras. Figure 3.17 shows the original frame from Camera B (section 1) and the processed image (section 2) with the circular object of interest identified within the frame with a red outline.

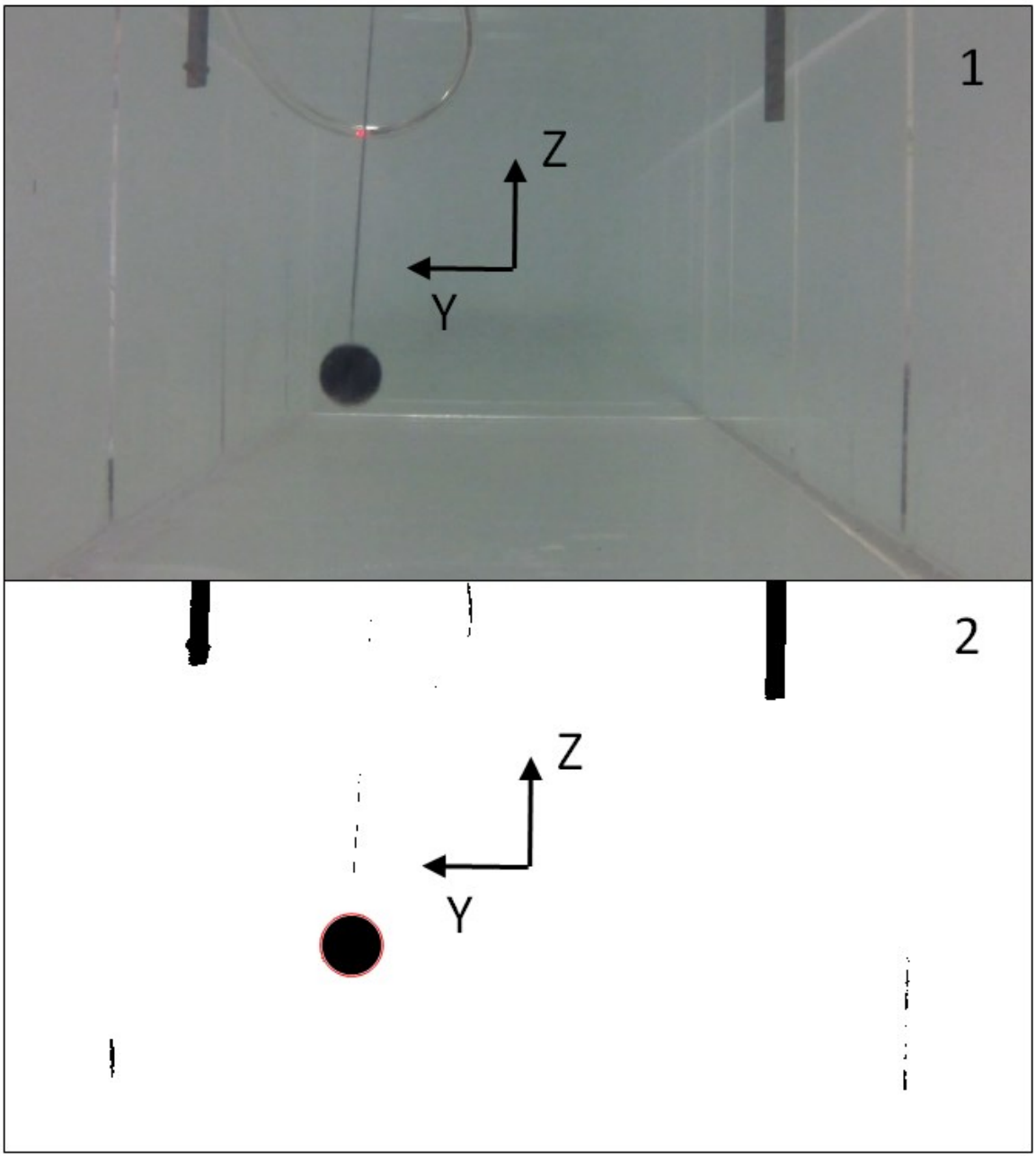


**Figure 3.17: Processing Camera B footage**

After obtaining a trace of the position of the sphere within the camera's frame of view, the sphere location is identified in physical space. This transformation is accomplished by applying a conversion from distance in the camera frame in units of pixels to distance in the physical world in units of cm. The conversion value between camera pixels and cm is based on the size of the sphere in frame. Figure 3.18 shows a sample trace of the sphere's

path following analysis of the footage for a trial where no heave compensation algorithm is applied.

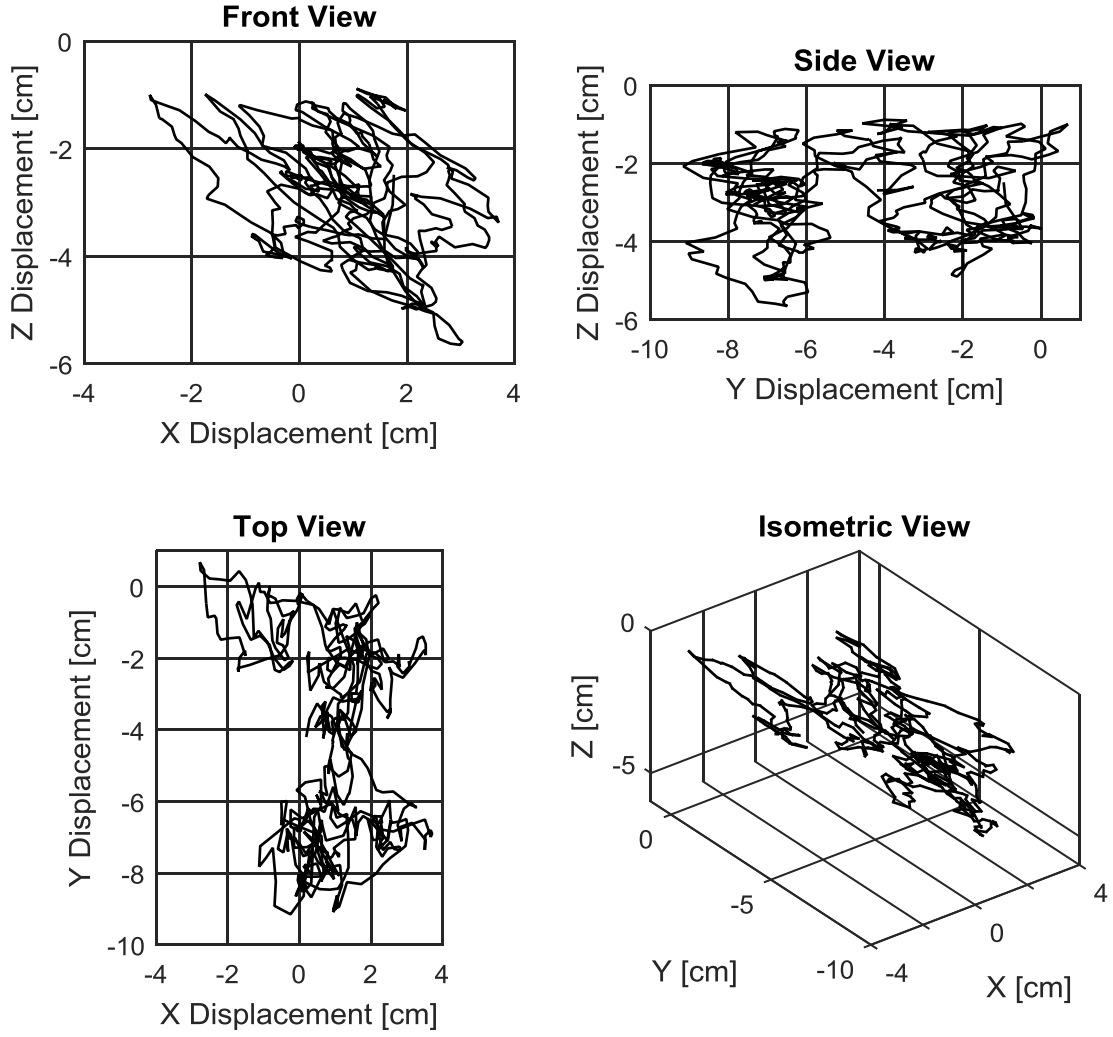


**Figure 3.18: Trace of sphere motion for an uncompensated motion test.**

The motion of the sphere in the flume tank is influenced by the winch operation. In order to control the winch motor, system identification work and PD controller design were required.

## 3.3. SYSTEM IDENTIFICATION AND PD CONTROLLER TUNING

To compare the performance of the different set-point algorithms, some form of closed-loop controller is required. This controller was to be consistent throughout all set-point trials.

A PID controller was initially considered for the flume-scale application. However, because the test rig mechanism was to imitate the constantly shifting ship motion displayed in Figure 3.12, the winch motor was expected to track a continually changing set-point. The integral term of a PID controller is included to reduce long-term offset error. Due to the fluctuations in the set-point signal, the importance of the integral term was reduced, and a PD controller was selected for the winch motor system.

Equation (3.9) is a transfer function of a third order system model for a DC motor in position control [53]. The variables are listed in Table 3.2. The Laplace variable is $\boldsymbol{s}$.

$$\frac{\theta_m(\boldsymbol{s})}{V(\boldsymbol{s})} = \frac{\frac{K_m}{J_m L_m}}{\boldsymbol{s}^3 + \left(\frac{B_m L_m + J_m R_m}{J_m L_m}\right)\boldsymbol{s}^2 + \left(\frac{B_m R_m + {K_m}^2}{J_m L_m}\right)\boldsymbol{s}} \tag{3.9}$$

Alternatively, the system model can be arranged as a state-space representation. Equation (3.10) demonstrates the state-space formulation of this model. Constants are present within the state-space model to account for unit conversion between voltage and PWM signals and between motor encoder counts and radians.

$$\begin{bmatrix} \dot{\theta}_m(\boldsymbol{s}) \\ \ddot{\theta}_m(\boldsymbol{s}) \\ \dot{i}(\boldsymbol{s}) \end{bmatrix} = \begin{bmatrix} 0 & 1 & 0 \\ 0 & -{B_m}/{J_m} & {K_m}/{J_m} \\ 0 & -{K_m}/{L_m} & -{R_m}/{L_m} \end{bmatrix} \begin{bmatrix} \theta_m(\boldsymbol{s}) \\ \dot{\theta}_m(\boldsymbol{s}) \\ i(\boldsymbol{s}) \end{bmatrix} + \begin{bmatrix} 0 \\ 0 \\ {12}/{L_m} \end{bmatrix} V(\boldsymbol{s})$$

$$Y(s) = \begin{bmatrix} -114.65 & 0 & 0 \end{bmatrix} \begin{bmatrix} \theta_m(\boldsymbol{s}) \\ \dot{\theta}_m(\boldsymbol{s}) \\ i(\boldsymbol{s}) \end{bmatrix} \tag{3.10}$$

The nomenclature for Equation (3.10) is presented in Table 3.2.

**Table 3.2: Nomenclature for system model of DC winch motor in Equations (3.9) and (3.10)**

| Nomenclature | Variable | Value | Unit | Measured or Identified |
|---|---|---|---|---|
| Back EMF constant | $K_m$ | $1.4\times10^{-3}$ | Vs/rad | Identified |
| Rotational friction | $B_m$ | $1.4\times10^{-4}$ | Nms/rad | Identified |
| Rotational inertia | $J_m$ | $1.0\times10^{-5}$ | $kgm^2$ | Identified |
| Motor inductance | $L_m$ | $5.0\times10^{-3}$ | H | Measured |
| Coil resistance | $R_m$ | 5.0 | Ω | Measured |
| Motor position | $\theta_m$ | | | |
| Motor voltage | $V$ | | | |
| Motor current | $i$ | | | |

Some motor parameters were measured in order to simplify the system identification process. Motor coil resistance was measured with an Amprobe 34XR-A multimeter [54] and inductance was measured with a B&K 885 LCR meter [55]. The winch motor's response to a chirp signal and step response was recorded and assessed in MATLAB's system identification application to optimize the remaining model parameters for agreement with the recorded output. Figure 3.19 shows the winch motor system and winch motor model response to a 12 V step input. The vertical axis of the figure represents the length of tow cable payed out, while the horizontal axis represents the passage of time in seconds. A normalized root mean square assessment of the model fitness for the step response is 99.7%. The measured model parameters are presented in Table 3.2 along with the optimized model parameters obtained from MATLAB's system identification application.

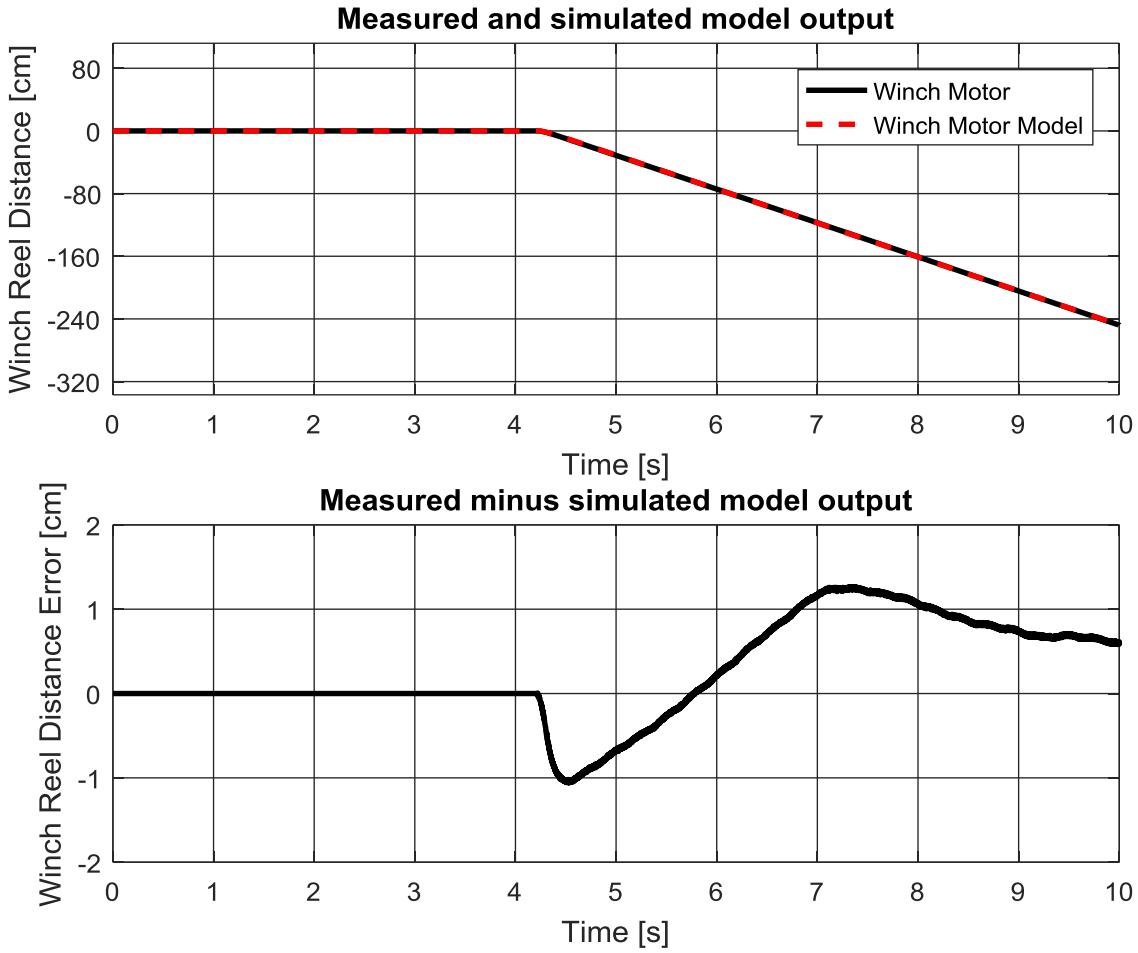


**Figure 3.19: Winch motor model and system step response**

The winch motor model response to a 12 V step input agrees well with recorded output data when provided over the same input data and initial conditions. An additional comparison between the system and model was carried out with a chirp signal to validate the model over a range of frequency inputs. Figure 3.20 shows the chirp signal response. The vertical axis of the figure represents the length of tow cable payed out, while the horizontal axis represents the passage of time in seconds. The chirp signal contained a maximum frequency component of 1.6 Hz.

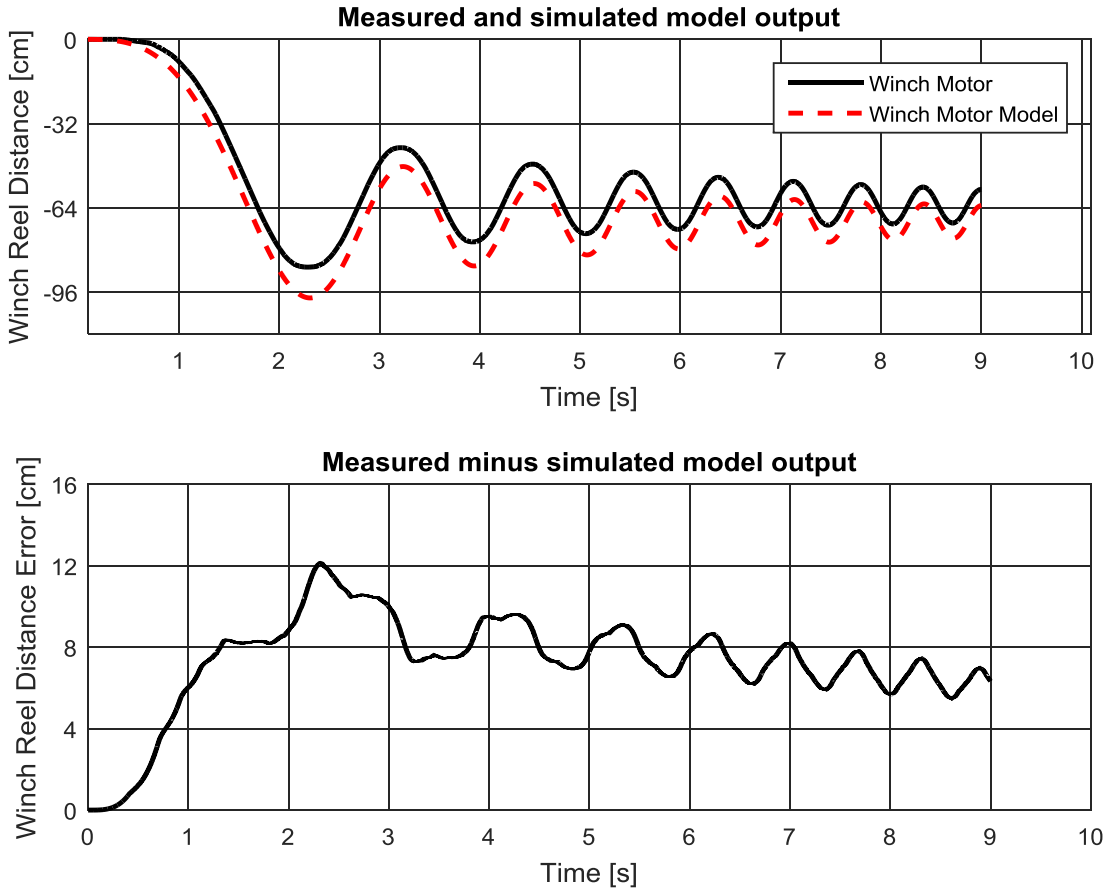


**Figure 3.20: Winch motor model and system chirp response.**

The winch motor model agrees reasonably well with the recorded output data for the chirp signal. The normalized root mean square assessment of model fitness for the chirp signal yields a value of 67.8%. An offset is apparent in Figure 3.20, which is the result of a faster model response than the actual motor. Due to the minimal mass and drag forces expected to be loading the motor during flume tank experiments, the unloaded model was used to approximate the loaded motor behaviour.

Figure 3.21 shows the open-loop frequency response of the resulting winch motor model where response magnitude is based on a system input in PWM and system output in encoder counts (720 encoder counts per revolution).

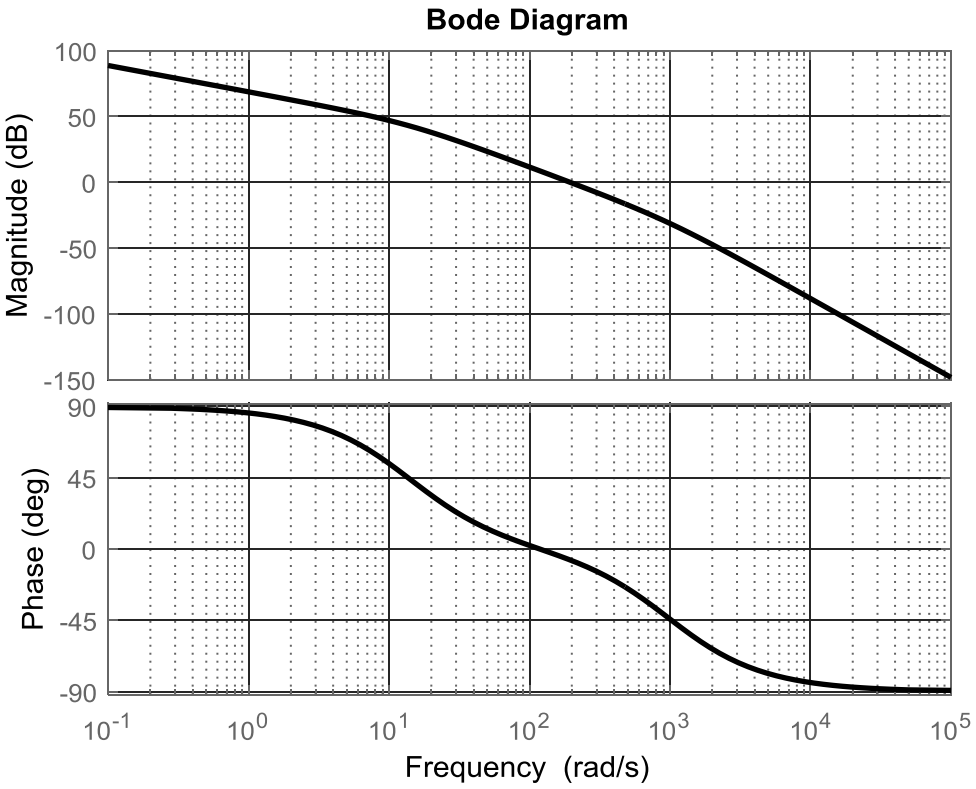


**Figure 3.21: Bode plot of winch motor model.**

System poles affect signal attenuation and can reduce tracking performance. For the identified motor model they are located at 14 rad/s and 1000 rad/s. 99% of the ship motion signal power is located below 4 rad/s, which means that the ship motion signal is relatively slow compared to the motor dynamics. The motor's speed relative to the ship motion confirms that the motor has suitable dynamic response for the test environment.

Once the winch motor system was established, discrete PD controller gains were designed using Simulink to take advantage of the automated PID tuning functionality. Because the video analysis is based on a 0.2 second window between measurements, a unit step response within 0.2 seconds without overshoot is used as a control objective. A control objective of 90% rise time in 0.12 seconds without overshoot was selected. In practice, a saturation limit was placed on the motors limiting their input voltage to 9 V as a precautionary measure. Imposing a 9 V saturation limit increased the 90% rise time to 0.2

seconds, which was still sufficient for the application. Figure 3.22 shows the motor model's response to a 1 cm step input.

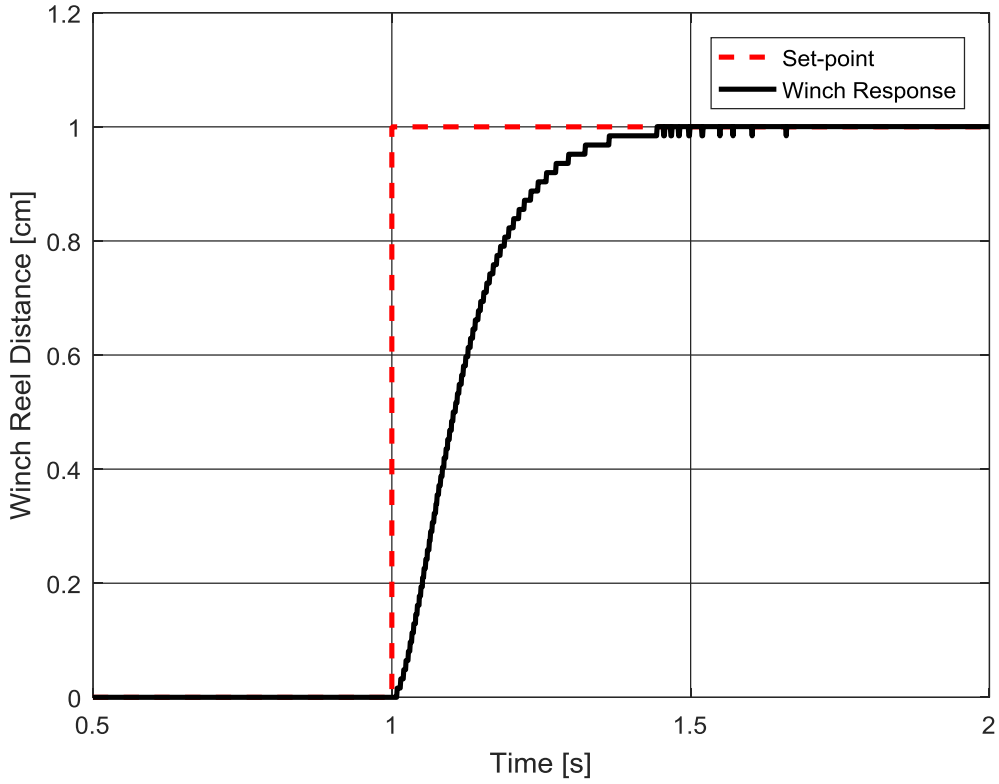


**Figure 3.22: Winch motor model response to step input with 9 V saturation.**

Figure 3.22 presents the effects of signal quantization which are introduced by encoder resolution. A 1 cm response is representative of the magnitude of the set-points provided in experimental tests. Figure 3.23 shows the winch motor model's response to a 1 cm sine wave input.

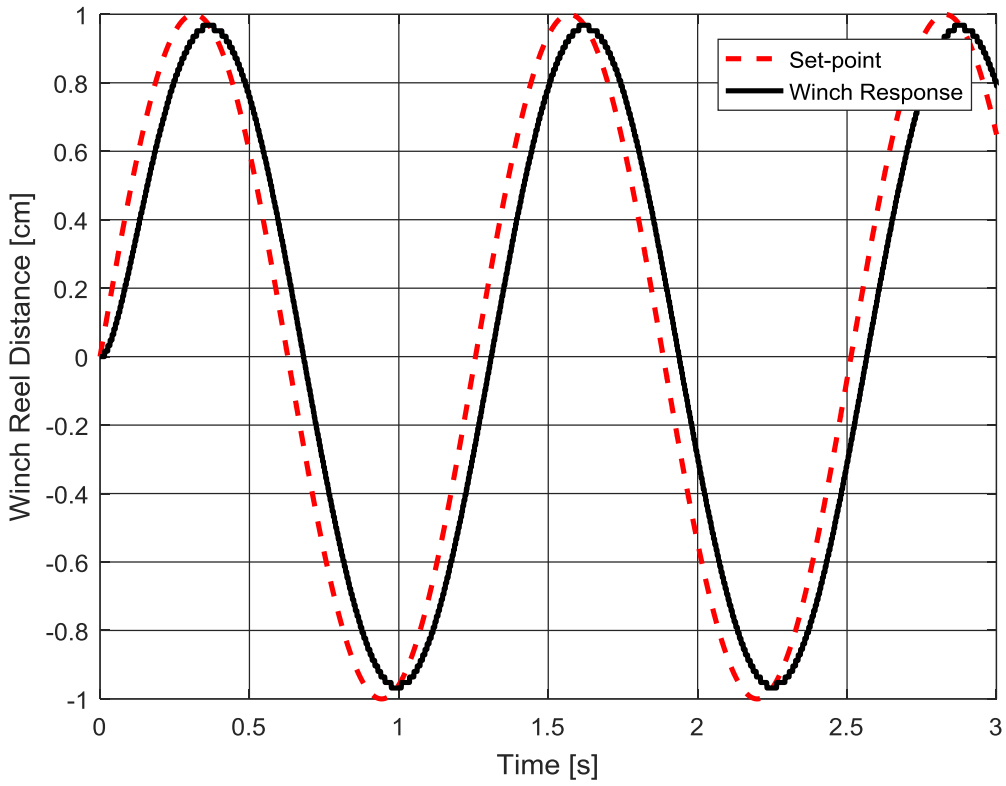


**Figure 3.23: Winch motor model response to sine input with 9 V saturation.**

When tracking the set-point at a relatively fast wave frequency of 5 rad/s, only 3.5% attenuation is observed. Peak-to-peak lag of approximately 0.05 seconds is also observed. These values are sufficiently small for the experimental test application. The proportional and derivative controller gains which were selected are 0.0067 and 0.00049, respectively.

Following controller design, the control loop was programmed in LabVIEW and implemented on the test mechanism. Figure 3.24 shows the real winch motor response when tracking the set-point provided by the Rigorous Sheave set-point algorithm. The winch response lag evident in Figure 3.23 appears to have very little impact on the experimental results in Figure 3.24.

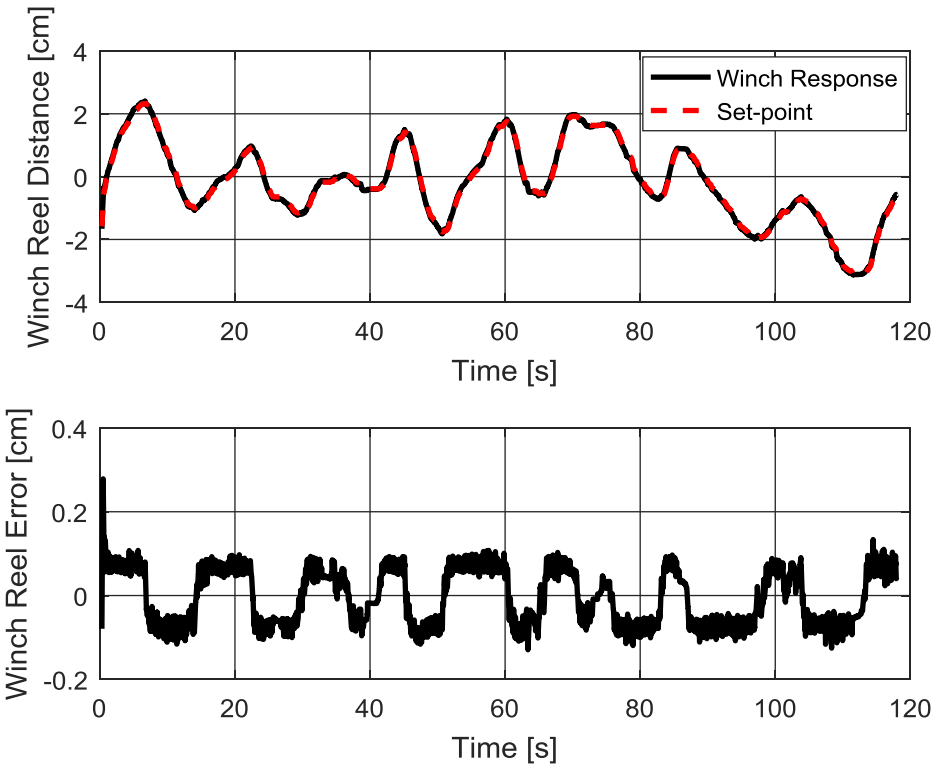


**Figure 3.24: Winch tracking performance in experimental tests with Rigorous Sheave algorithm.**

Using the data collected from experimental flume-scale tests, the relative performance of the set-point algorithms can be assessed.

## 3.4. RESULTS

Results of the experimental tests are assessed by fitting an ellipsoid around the sphere's trace such that sphere is contained within the ellipsoid for 95% of the time. The ellipsoid volume is then used to assess the performance of the set-point algorithm which was used for heave compensation. The ellipsoid fitting process is described in Section 3.4.1, while an assessment of the ellipsoid volume results are presented in Section 3.4.2.

### 3.4.1. Ellipsoid Fitting

The ellipsoid fitting process requires several steps. An illustration of a general ellipsoid with semi-principal axes $X_E$, $Y_E$, and $Z_E$ and the corresponding radii, $r$, along those axes is illustrated in Figure 3.25.

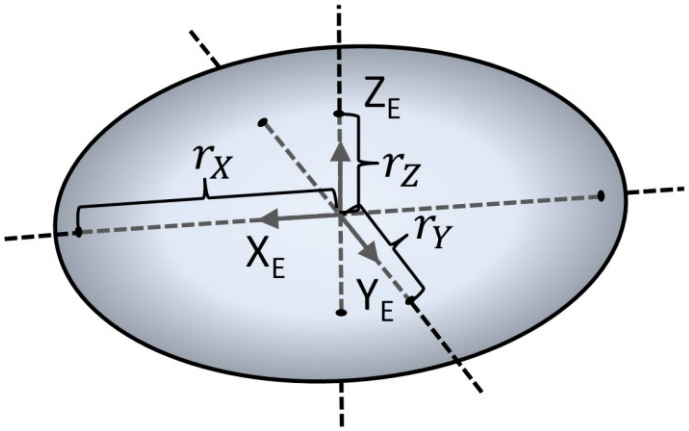


**Figure 3.25: Ellipse with semi-principle axes and radii labelled.**

Ellipsoid volume is computed using Equation (3.11):

$$Volume = \frac{4}{3}\pi r_X r_Y r_Z \tag{3.11}$$

In order to fit an ellipsoid to the sphere motion trace, first an ellipsoid reference frame like the one pictured in Figure 3.25 is positioned on the centroid of the sphere trace. A best-fit line is then generated through the sphere trace and the ellipsoid frame is oriented such that its $X_E$-axis is collinear with the best-fit line. Next, a best-fit plane is projected through the sphere trace. The plane formed by the ellipsoid $X_E$ and $Y_E$ axes are coplanar with the best-fit plane. By aligning the ellipsoid in this way, the variance of the sphere trace is maximized along the $X_E$ and $Y_E$ axes and a consistent orientation procedure can be used across all trials. The shape of the ellipsoid is determined by using the variance of the sphere trace in the $X_E$, $Y_E$, and $Z_E$ directions to determine the relative proportionality of the ellipsoid radii. Finally, a cost-minimization algorithm is used to scale the size of the ellipsoid such that 95% of the sphere trace is contained within the bounds of the ellipsoid surface. Because each point along the trace is taken at a consistent time interval of 0.2 seconds, the result of the fitting process indicates that the towed sphere is located within the ellipsoid 95% of the time during the trial. Figure 3.26 shows a sphere trace fit with an ellipsoid.

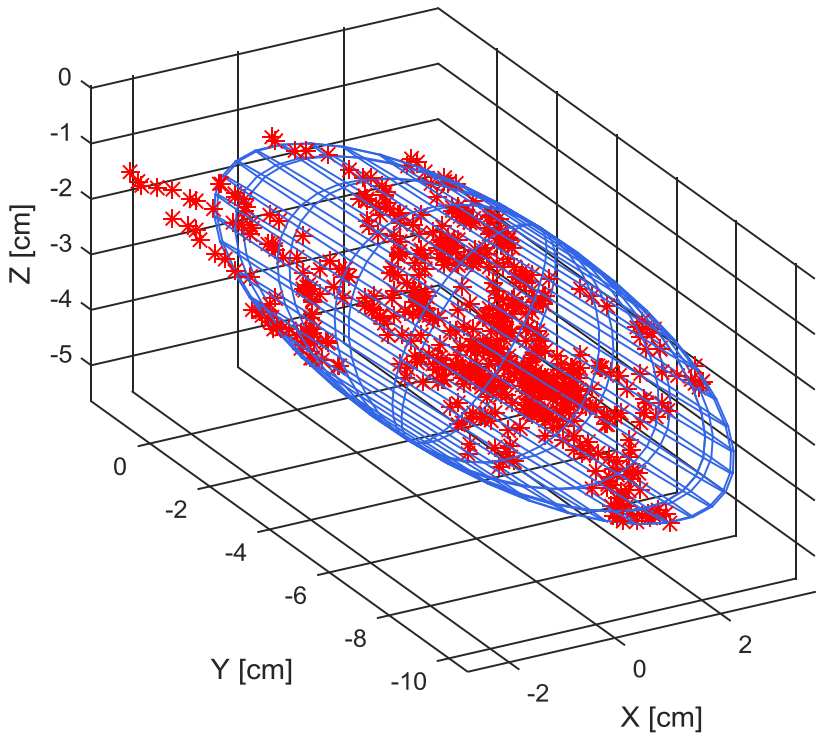


**Figure 3.26: Ellipsoid fit around sphere trace for uncompensated motion trial.**

The ellipsoid volume values for experimental test data can next be compared to assess the performance of the set-point algorithms.

The set-point algorithms presented in this thesis assume that the winch-based AHC system does not provide motion compensation capabilities along the *y* axis. Despite this, *y* direction motion is considered part of the host vessel motion and is used to derive ellipsoid geometry for set-point algorithm assessment.

### 3.4.2. Experimental Results

The test cases which are examined in this thesis consist of the four set-point algorithm approaches presented in Section 3.1, and two baseline trials. The first baseline trial involved recording the sphere trace without any induced motion from the test mechanism. The resulting ellipsoid for a stationary mechanism case captured the effects of the flume tank turbulence and represented the smallest possible ellipsoid area. The second baseline trial involved operating the test mechanism with active heave compensation disabled. The

resulting ellipsoid for an uncompensated case represented the largest possible ellipsoid area (assuming that all set-point algorithms offered some level of heave compensation). These best and worst-case baseline trials are used to provide a reference for analysis of the four set-point algorithms.

Figure 3.27 compares the ellipsoid volume of the different test cases. The Rigorous Waterline case is absent from Figure 3.27, as it presented stability issues in experimental trials.

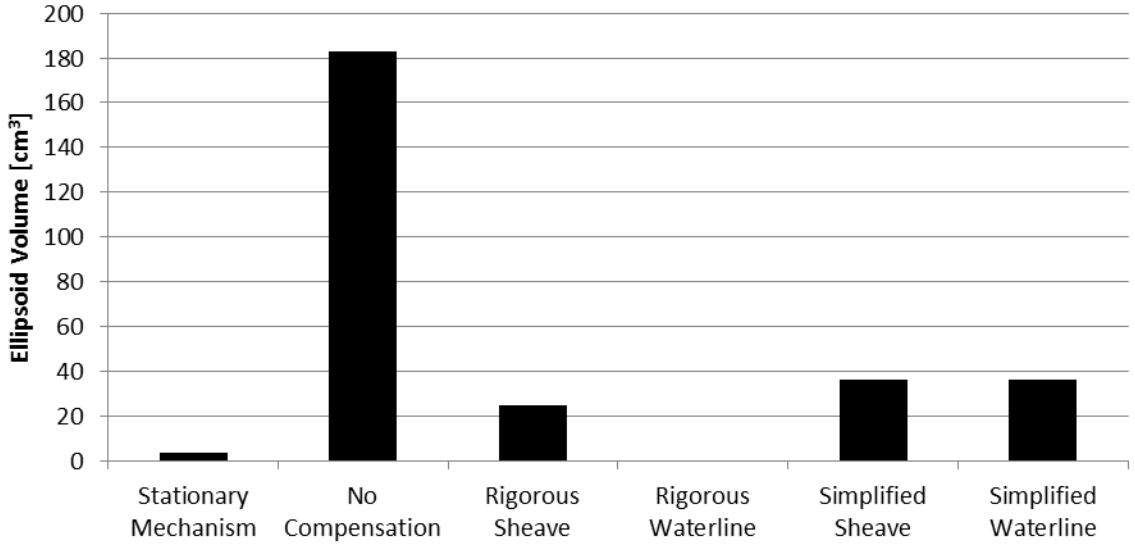


**Figure 3.27: Comparison of ellipsoid volume for different flume tank test cases.**

Figure 3.27 shows that the uncompensated case demonstrates the largest amount of sphere motion, while the stationary mechanism case demonstrates the smallest amount of sphere motion. Amongst the set-point algorithms which are presented in Figure 3.27, the Rigorous Sheave algorithm performs better than both the Simplified Sheave and Simplified Waterline algorithms. The Rigorous Sheave algorithm reduces motion by 86% compared to the uncompensated case. The two Simplified algorithms perform nearly identically, reducing sphere motion by 80% compared to the uncompensated case. The best possible performance is indicated by the difference between the Stationary Mechanism case and the uncompensated case, which is 97% motion reduction.

As shown in Figure 3.27, the Simplified Sheave and Simplified Waterline algorithms performance was extremely similar. These similarities between the two Simplified

algorithms are a result of the test environment. The combination of the nominal winch height, motion envelope provided by the motion path, and the length of tow cable result in a flume-scale version of an extremely shallow tow with very calm conditions. In shallow and calm conditions, the Simplified Sheave and Rigorous set-point algorithms provide the same set-point. Due to limitations of the test environment, these conditions could not be altered. Figure 3.28 shows the set-points provided by the Simplified Sheave and Simplified Waterline algorithms in the upper portion of the figure as well as the difference between the two algorithms in the lower portion of the figure. The difference between the two algorithms is achieved by subtracting the Simplified Waterline trace from the Simplified Sheave trace. Figure 3.28 indicates a maximum difference of approximately 2 mm between the two set-point algorithms in the flume-scale experimental tests. The vertical axes represent the set-point value provided to the motor controller in units of cm, while the horizontal axis represents the passage of time in seconds.

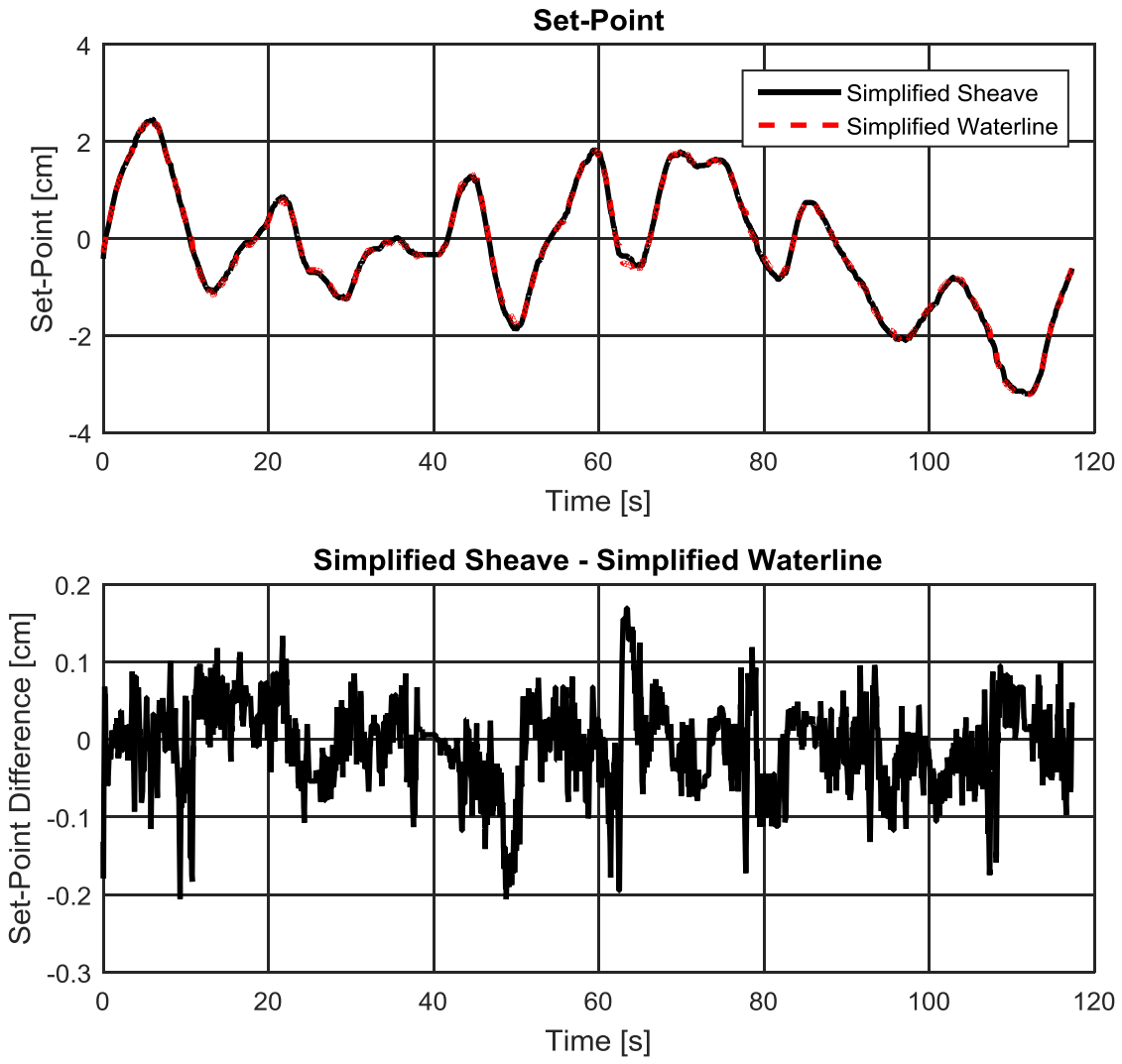


**Figure 3.28: Comparison between Simplified Sheave and Simplified Waterline algorithms for experimental tests.**

Despite the fact that the test environment could not be altered to highlight the differences of the Simplified algorithms, the test environment is replicated and then modified in simulation later in this thesis.

Because simplified set-point algorithms assume that the sheave angle remains constant, the difference in performance between the Simplified Sheave algorithm and the Rigorous Sheave algorithm is dependent upon the amount of sheave angle variability. Figure 3.29 is a plot of the sheave angle over the course of the Simplified Sheave trial. The vertical

axis represents the sheave angle in units of degrees, while the horizontal axis represents the passage of time in seconds.

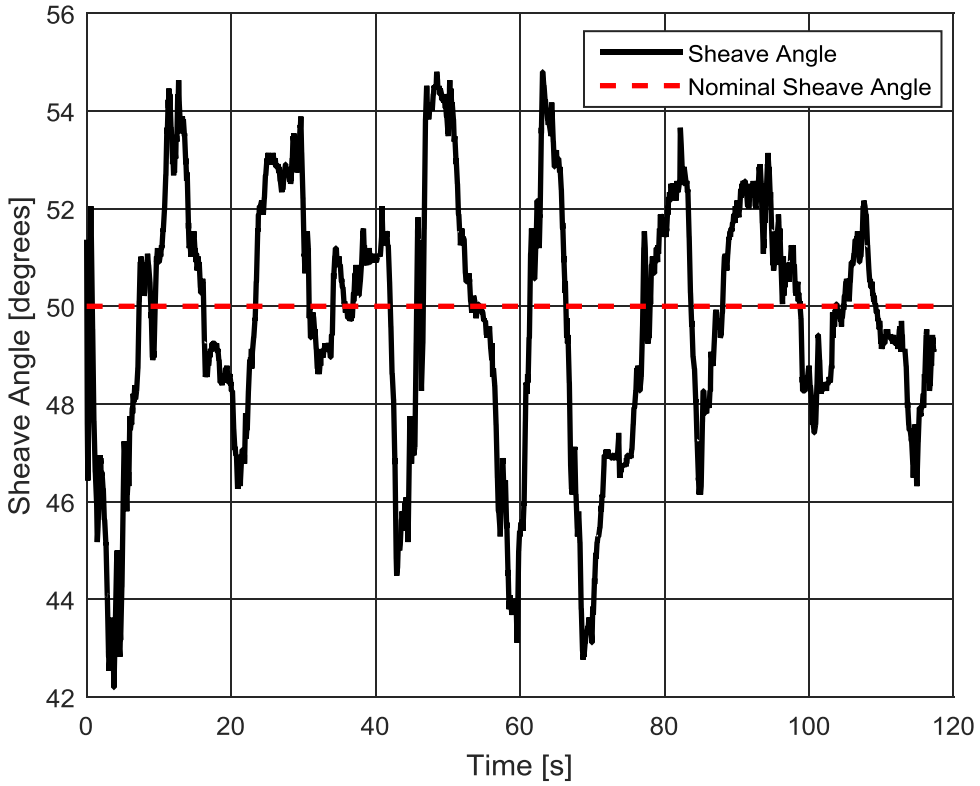


**Figure 3.29: Sheave angle change over time for the Simplified Sheave trial.**

Figure 3.29 shows that the sheave angle changes by up to 13º. The nominal sheave angle used for the calculation of the set-point in experimental tests was 50º. There was as much as 8º error associated with this assumption for the Simplified Sheave trial according to Figure 3.29. The performance of the Simplified Sheave algorithm is directly impacted by the difference between the actual sheave angle and its nominal value. In the experimental test results presented in Figure 3.27, the sheave angle disagreement resulted in a measurable difference between the Simplified Sheave algorithm and the Rigorous Sheave algorithm.

While the Rigorous Sheave algorithm performed well, the Rigorous Waterline algorithm exhibited a stability issue that led to erratic behavior. One of the reasons for this instability is that this compensation method produces large responses to small changes in

the tow-line angle. For example, with the winch in its nominal position 46 cm above the waterline, an error of 1º in sheave angle measurement from its nominal value corresponds to an error of approximately 1 cm in tow cable length. Furthermore, low cable tension and significant rotational inertia of the sheave angle measurement device allowed for a discontinuity in the line as depicted in Figure 3.30 whenever the sheave angle changed. The discontinuity aggravated Rigorous Waterline instability by introducing a source of measurement error – especially when the sheave angle changed quickly. The Rigorous Sheave algorithm was more robust in response to sensor error, since the compensation method calculates the winch command based on the winch location, not on the difference in tow cable length. For the same error of 1º in sheave angle measurement near its nominal range, the maximum expected error for the Rigorous Sheave algorithm is approximately 0.13 mm.

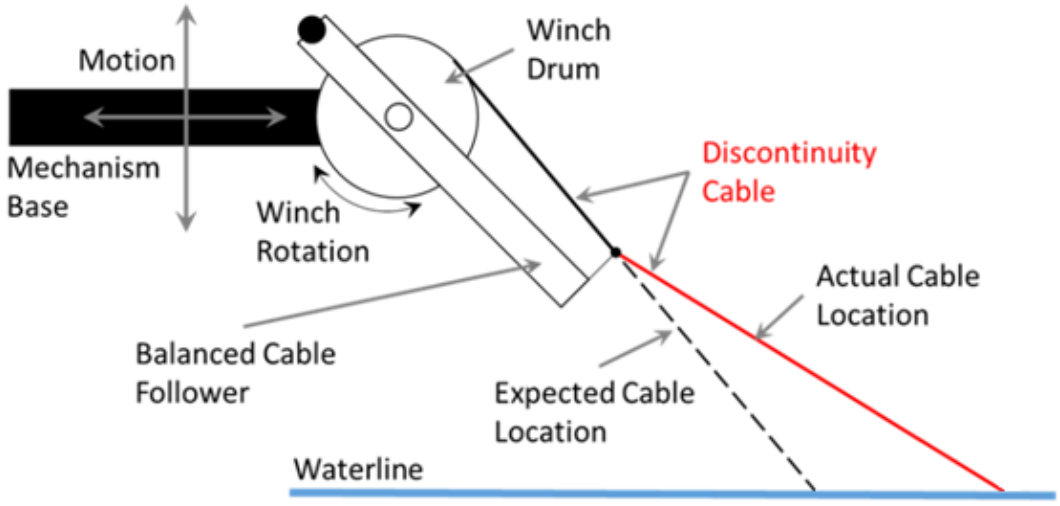


**Figure 3.30: Illustration of tow cable discontinuity caused by sheave angle measurement device.**

## 3.5. SUMMARY

This chapter has provided the description of set-point algorithms and their experimental implementation, meeting the first key objective of this thesis described in Chapter 1 and contributing flume-scale experimental data analysis toward the second and third

objectives of this thesis. The results of flume-scale experimental tests indicate that the Rigorous Sheave algorithm performed best amongst those which were tested for the specific test environment. The good performance of the Rigorous Sheave algorithm compared to the Simplified Sheave algorithm indicates that real-time measurement of the sheave angle is useful for the flume-scale experimental test environment. It is evident from the instability associated with the Rigorous Waterline algorithm that it is likely a poor choice for AHC systems. The performance of the Rigorous Waterline algorithm is investigated further in simulation in Chapters 4 and 5. Due to the identical performance of Simplified Sheave and Simplified Waterline algorithms, these methods are investigated in simulation with a rescaled test environment to emulate a deeper tow with increased ship motion in Chapter 4.

# CHAPTER 4 FLUME-SALE COMPUTER SIMULATION

This chapter describes the development of a computer simulator which is used to model the flume-scale towed system discussed in Chapter 3. Cable models composed of elemental cable segments such as Hover et al. [12] and Driscoll et al. [39] were used as a framework to develop a computer simulator in MATLAB and Simulink. Within Simulink, the Simscape mechanical libraries were used to model the towed system. Creation and validation of this flume-scale simulator contribute toward the second and third key objectives of this thesis described in Chapter 1.

Section 4.1 describes the cable model theory that was used to construct the computer simulator as well as model implementation carried out in MATLAB and Simulink. Section 4.2 presents simulator results in recreating the flume-scale experimental test environment as well as a modified version of the test environment, and Section 4.3 summarizes these results.

## 4.1. CABLE MODEL DEVELOPMENT

In order to model the flume-scale test environment accurately, a three-dimensional model was developed. Section 4.1.1 describes how rigid linkages and joints were assembled to create a computer simulator of a tow cable and spherical towed body. External forces are applied to the system to simulate hydromechanical effects, such as fluid drag and buoyancy. Section 4.1.2 describes how the flume tank test environment was replicated in simulation to apply appropriate external effects to the cable model.

### 4.1.1. Towed System

The cable model presented in this section treats the towed system as a collection of discretized segments. An elemental description of the forces acting on any segment can, therefore, be extended to the entire tow cable. A similar approach is used to develop a cable model for Simulink. The cable is treated as a series of rigid linkages, with a rigid towed sphere at the free end. Figure 4.1 illustrates how the neighbouring rigid bodies are connected with respective co-ordinate frames located at the center of gravity of each

segment. The neighbouring links, $L_i$, are connected to make up the physical towed system, with the towed sphere indicated by *TS*.

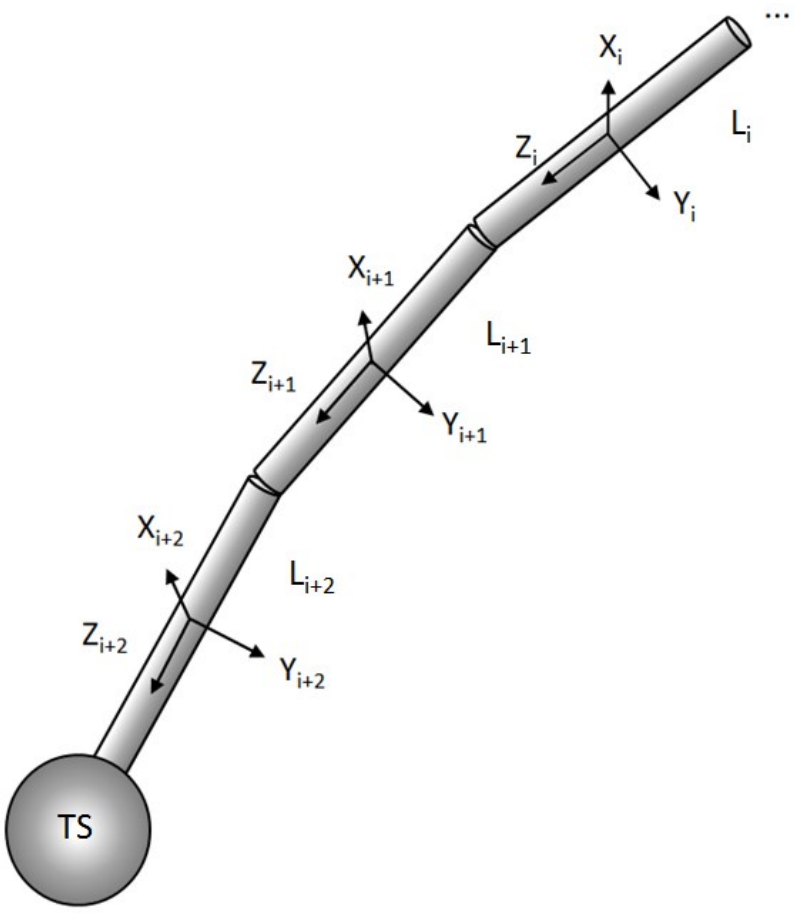


**Figure 4.1: Tow cable linkages connected in succession with respective co-ordinate frames and towed sphere attached.**

Each rigid tow cable linkage is modeled as a cylinder. Each cylindrical tow cable segment has its mass evenly distributed. The rotational inertia of the rigid cable segment is, therefore, equivalent to small, straight segment of the actual tow cable. The towed sphere has evenly distributed mass as well.

The mass properties of the tow cable and the towed sphere were obtained by measuring their values directly. The tow cable has a nominal diameter of 0.46 mm. The mass of a section of tow cable was measured with a Sartorius LP 1200 S digital scale to obtain the mass per unit length and density of the cable. The mass of the towed sphere was also

measured with the same digital scale and the diameter was measured with a set of calipers. Table 4.1 provides the physically measured parameters.

**Table 4.1: Tow cable and sphere parameters.**

| | Parameter | Value |
|---|---|---|
| Tow Cable | Diameter | 0.45 mm |
| | Mass per Length | 0.20 g/m |
| Towed Sphere | Diameter | 10 mm |
| | Mass | 1.33 g |

In Simulink, Simscape rigid bodies from SimMechanics Second Generation are placed in the test environment with parameterized mass properties to achieve this mechanical behaviour. Figure 4.2 shows the placement of a rigid cable link in the Simulink environment.

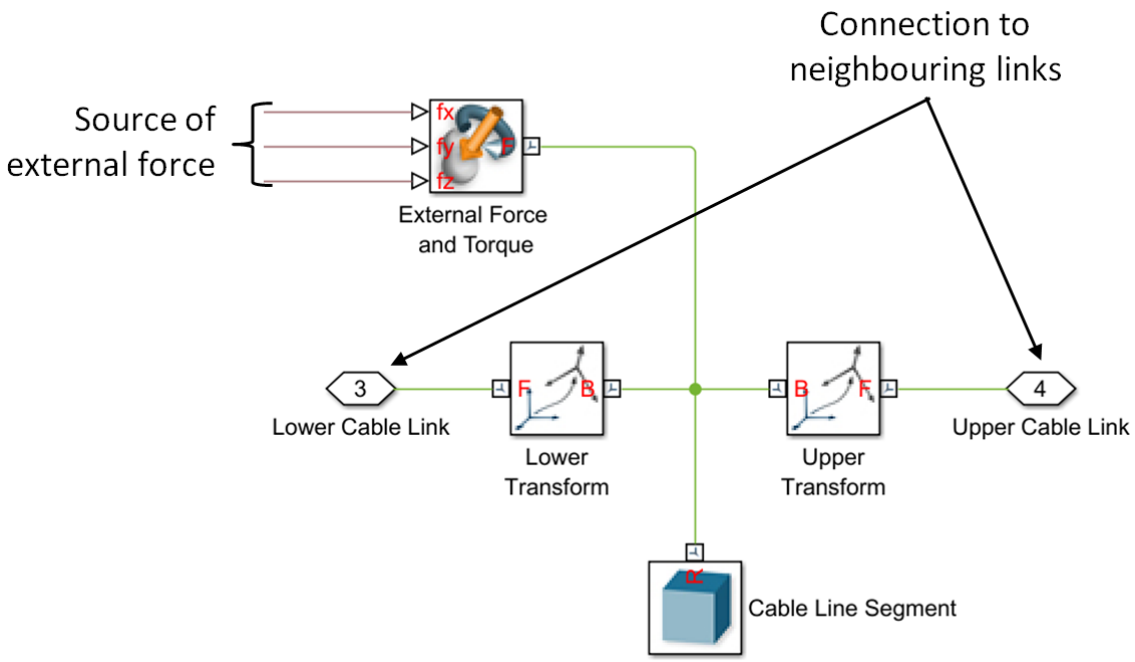


**Figure 4.2: Simulink block diagram of a rigid cable link.**

In Figure 4.2, the rigid cable link geometry and mass is captured by the "Cable Line Segment" block. A reference frame exists at the centre of mass of the cylindrical cable segment, as illustrated in Figure 4.1. The "Upper Transform" and "Lower Transform"

blocks create reference frames at either end of the cable link cylinder to which the neighbouring cable segments, $L_i$, are attached with a universal joint. External forces are applied to the centre of mass of the cable link with the "External Force and Torque" block.

Figure 4.3 shows a schematic of cable segments $L_i$ and $L_{i+1}$ connected by a universal joint. The cable segments are separated so that the joint is visible. In simulation, the ends of these segments are in direct contact. The universal joint is a two DOF rotational joint which allows for motion between cable segments, but restricts $Z_i$ axis rotation along the cable, as this rotation is not typically experienced during normal use. Hover et al. [12], Driscoll et al. [39], and Kamman and Huston [48] all describe the assumption of minimal tow cable torsion in their work. Figure 4.3 shows $X_i$ and $Y_i$ rotation directions.

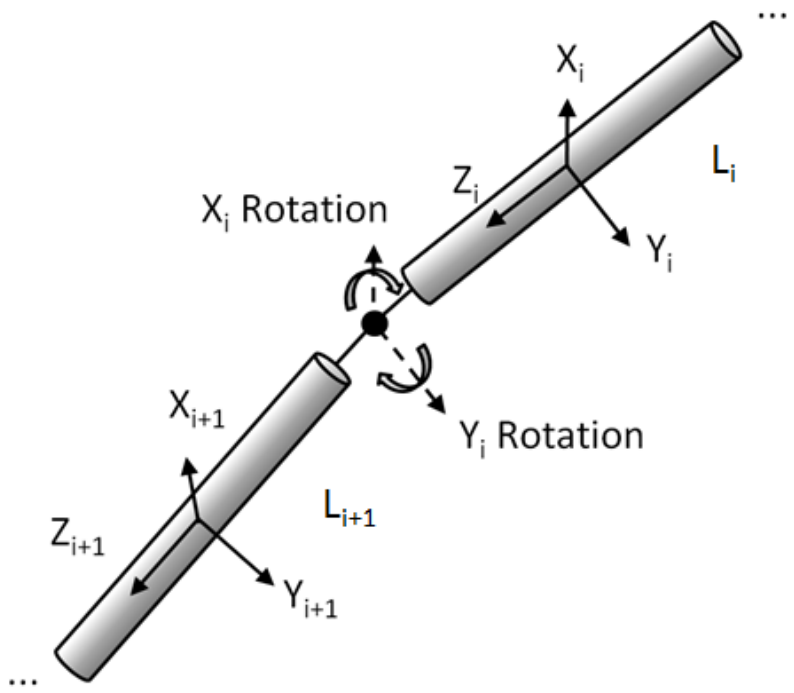


**Figure 4.3: Universal joint between two cable segments allowing $X_i$ and $Y_i$ rotation.**

In order to discern whether the flume-scale experimental test environment represented a low-tension application of a towed body, cable tension can be obtained by observing the sheave angle during experimental tests. Using the sheave angle and the weight of the towed sphere, the tension force vector tangent to the tow cable can be computed. The

magnitude of this force vector should provide a good estimation of cable tension. Figure 4.4 displays how cable tension can be resolved from the net vertical force and sheave angle.

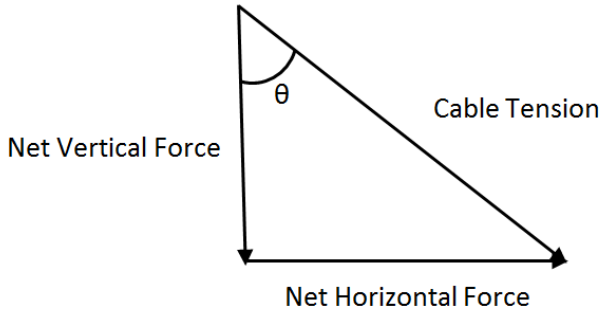


**Figure 4.4: Cable tension displayed as combined net horizontal and vertical forces.**

The net vertical force in Figure 4.4 is 0.0125 N, which is calculated by subtracting the buoyant force acting on the submerged sphere from the sphere's weight in air. The nominal sheave angle is 50º, which is $\theta$ in Figure 4.4. Cable tension is, therefore, approximately 0.02 N.

The modulus of elasticity of the tow cable is required in order to carry out this computation. A representative value of modulus of elasticity for nylon is 3 GPa, which is the material from which the tow cable is constructed [56] [57]. Tensile strain can be computed using Equation (2.3). Tensile strain $\varepsilon_T$ is $4.1\times10^{-5}$ m/m in this flume-scale application, indicating a very small tensile extension of 42 μm. As a result of the very small tension and tensile deflection in the flume-scale experiment, tensile stiffness is neglected from the flume-scale computer simulation.

While tensile strain provided very little effect in the flume-scale experimental tests, curvature strain was found to be more than an order of magnitude greater. An estimate of curvature strain is computed using Equation (2.4). The minimum radius of curvature observed in the flume tank experiments is approximated from camera footage. The tow cable radius is known. Curvature strain is approximately $8.3\times10^{-4}$ m/m. Because curvature strain is much larger than tensile strain in the flume-scale towing application, rotational stiffness and damping effects are included in the computer simulator and

applied at each universal joint connecting cable segments. Figure 4.5 illustrates how internal stiffness and damping can be resolved for the endpoint of a rigid cable segment.

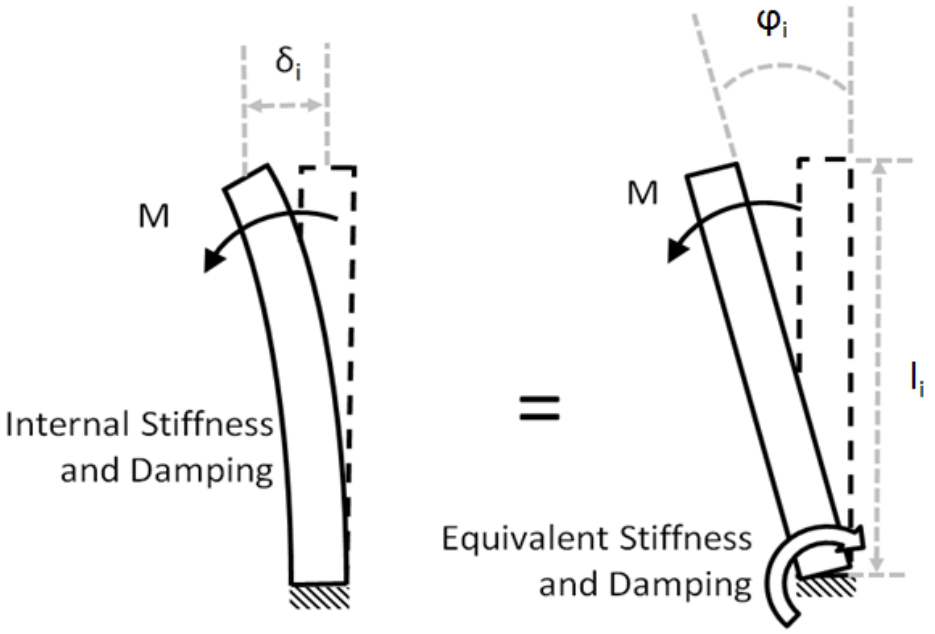


**Figure 4.5: Length of cable under load. Internal stiffness and damping apply restoring moment for left cable segment. Stiffness and damping applied at discrete location on rigid cable segment on the right.**

To obtain values for rotational stiffness, beam theory can be applied. Equation (4.1) displays the deflection of a cable segment $\delta_i$ in response to an applied moment $M$:

$$\delta_i = \frac{Ml^2}{2EI} \tag{4.1}$$

where $E$ is the modulus of elasticity of the cable, $I$ is the moment of inertia of the cable cross-section, and $l_i$ is the length of the cable segment. For small deflections, $\delta_i$ is assumed to be approximately the same length as the arc formed by cable segment displacement, as stated in Equation (4.2).

$$\delta_i \cong l_i \varphi_i \tag{4.2}$$

Finally, the rotational cable stiffness value, $K_R$ can be obtained, as presented in Equation (4.3).

$$K_R = \frac{M}{\varphi_i} = \frac{2EI}{l} \tag{4.3}$$

Rotational damping was computed by observing the decaying vibrational response of a segment of cable. A small length of cable was fixed at one end and free at the other. The free end was deflected and then released. The responding vibration was recorded at 60 frames per second with the GoPro Hero 3+. It was observed that over 12 vibration periods, the vibration decayed almost entirely. 99% amplitude decay was assumed. The logarithmic decrement method was used to obtain a damping ratio from this observation. Equation (4.4) indicates how the logarithmic decrement *D* can be computed:

$$D = \frac{1}{n} \ln\left(\frac{Amp(t)}{Amp(t + nT_P)}\right) \tag{4.4}$$

where *Amp(t)* indicates the response amplitude at time *t*, *n* indicates the number of periods over which the response decayed, and $T_p$ is the response period. The damping ratio $\zeta$ is next defined in Equation (4.5).

$$\zeta = \frac{1}{\sqrt{1 + \left(\frac{2\pi}{D}\right)^2}} \tag{4.5}$$

From the vibration decay observations, the damping ratio $\zeta$ was 0.061, which indicates an underdamped system.

Next, the tow cable segment is described as a rotational spring-mass-damper system. Figure 4.6 shows how the universal joint is used as a pivot for the rotational mechanical system with rotational moment of inertia *J*, rotational stiffness $K_R$ and rotational damping $B_R$. Stiffness $K_R$ is defined already, and Equation (4.6) describes the calculation of rotational inertia for a uniform, rigid rod rotating from one end:

$$J = \frac{1}{3} m_i {l_i}^3 \tag{4.6}$$

where $m_i$ indicates the mass per unit length of the cable segment.

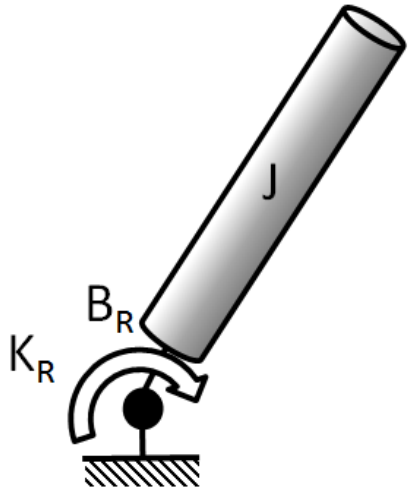


**Figure 4.6: Cable segment described as mechanical rotational system.**

This rotational mechanical model allows for the determination of $B_R$ from $\zeta$. Equation (4.7) describes the governing equation of the rotational mechanical system, where τ is torque.

$$\tau = J\ddot{\theta}_i + B_R\dot{\theta}_i + K_R\theta_i \tag{4.7}$$

Next, using Equation (4.7), $B_R$ can be computed.

$$B_R = 2\zeta\sqrt{JK_R} \tag{4.8}$$

The 101 cm tow cable is discretized into 20 segments, each approximately 5 cm long. Table 4.2 contains the dynamic tow cable parameters for 5 cm segments.

**Table 4.2: Dynamic tow cable parameters**

| | Parameter | Value |
|---|---|---|
| Tow Cable | Young's Modulus | 3 GPa |
| | Rotational Stiffness | $4.488\times10^{-6}$ Nm/deg |
| | Rotational Damping | $3.116\times10^{-9}$ Nms/deg |

In Simulink, Simscape universal joint blocks connect the rigid cable segment links. Figure 4.7 shows a universal joint block connecting two cable links.

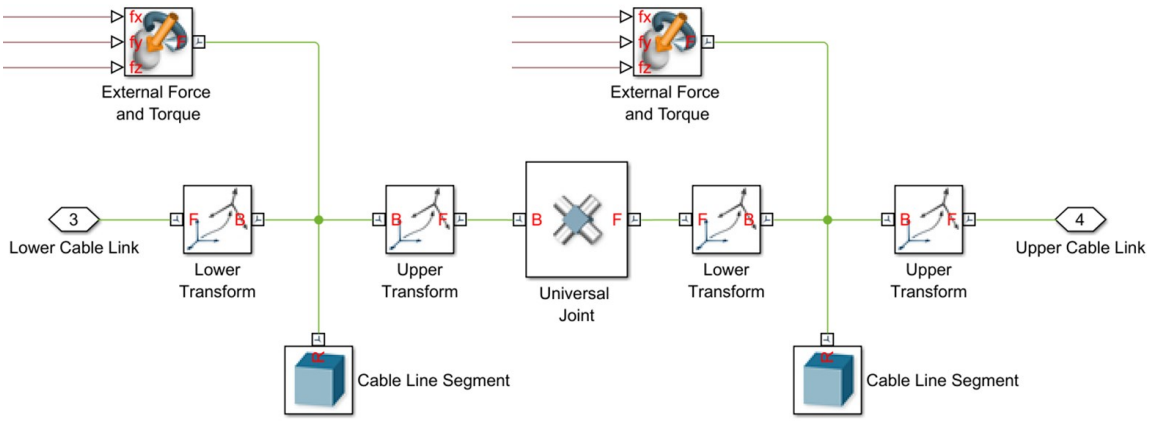


**Figure 4.7: Connection of two rigid cable links with a universal joint.**

In Figure 4.7, the rigid cable links are joined with a universal joint. The universal joint is located between the "Lower Transform" block of one link and the "Upper Transform" block of the other.

Following the physical construction of the flume-scale cable model, external effects are implemented to reflect the conditions experienced at the flume tank during testing.

### 4.1.2. External Effects

When the cable segments and towed sphere are submerged in flowing water, several forces are applied to the submerged objects. Figure 4.8 illustrates how drag, buoyancy, and gravity act on a cable link.

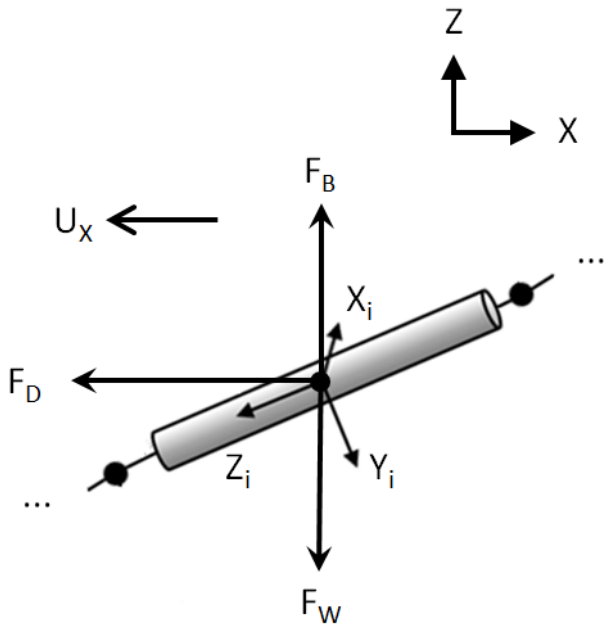


**Figure 4.8: Forces acting on a cable link.**

Weight affects all cable linkages and the towed sphere. Weight is a function of the gravitational field $g$ and the mass of the cable segment or towed object, $m_{obj}$. Equation (4.9) describes the force due to gravity. $F_G$ represents the weight of a cable segment. Weight is always applied in the negative $z$ direction in the world frame.

$$F_W = m_{obj} g \tag{4.9}$$

Buoyancy behaves similarly to weight within the flume-scale simulation. The buoyant force acts in the positive $z$ direction in the world frame. Buoyancy is only applied to components which are submerged beneath the flume tank waterline. Buoyancy is a function of the density of the flume tank water $\rho_w$ and the displaced volume $V_D$, which is equivalent to the volume of the cable segment of interest or the towed object which is submerged. Equation (4.10) describes the buoyant force.

$$F_B = \rho_w g V_D \tag{4.10}$$

When an object moves through fluid, a portion of the fluid surrounding the object is transported along with the object. The mass of the transported fluid can influence the dynamic response of the object moving through the fluid such that, the additional mass of

the transported fluid increases the amount of inertia of the object. This effect is called added mass. Added mass is a function of the transported object's shape [58]. Equation (4.11) and Equation (4.12) represent the value of added mass for a sphere $m_{SA}$ and cylinder $m_{CA}$, respectively.

$$m_{SA} = \frac{2}{3}\rho_w \pi {r_S}^3 \tag{4.11}$$

$$m_{CA} = \rho_w \pi l_i {r_C}^2 \tag{4.12}$$

where $r_S$ is the radius of the towed sphere, $r_C$ is the radius of the cable segment, and $l_i$ is the length of the cable segment. The value of added mass for the tow cable and towed sphere used in the simulator are 0.17 g/m and 0.26 g, respectively.

Fluid drag force is applied to any object moving through fluid. The drag force is only applied to components submerged beneath the flume tank waterline. Equation (4.13) describes the fluid drag force.

$$F_D = \frac{1}{2}\rho_w C_D A_E |U_i| U_i \tag{4.13}$$

where $C_D$ is the drag coefficient of the submerged object (which is dependent upon geometry), $A_E$ is the area exposed to the flowing fluid, and $U_i$ is the relative flow velocity vector in the submerged objects co-ordinate frame. Flow is decomposed into cable segment co-ordinates $x_i$, $y_i$, and $z_i$ for drag calculation. For flow along the segment $x_i$ and $y_i$ axes, the corresponding area $A$ used for drag calculation is the product of cable diameter and cable segment length, while the area $A$ for tangential flow along the $z_i$ axis is a product of the cable circumference and length $l_i$. The drag coefficient used for the drag force computation is based on the Reynolds number of the submerged object in the particular flow [59]. Equation (4.13) shows the formula for computation of an object's Reynolds number:

$$Re = \frac{\rho_w U D_C}{\mu} \tag{4.14}$$

where $D_C$ is the characteristic length of the object, which is the diameter of the tow cable or towed body, and $\mu$ is the dynamic viscosity of the fluid, which is 1.20 mNs/m$^2$ [59] for seawater. Drag coefficients for normal flow against the tow cable and flow over the towed sphere are found to be 1 and 0.5 in theory [59], following from their Reynolds number. Drag acting tangentially along the tow cable has a much smaller influence on the system. The tangential drag coefficient is approximated by 0.01 [12].

When gravity, buoyancy, and drag act upon a submerged body in simulation, a corresponding force is applied to the centre of gravity of that rigid body link with the "External Force and Torque" block, which can be observed in Figure 4.2.

Fluid flow speed within the flume tank varied as a function of depth. Flow variation was included in the simulator and the Vectrino velocimeter was used to measure this effect. Figure 4.9 shows a plot of the mean *x* direction flow profile, which is the primary flow direction in the flume tank. The vertical axis of Figure 4.9 indicates the depth in cm of the measurement, while the horizontal axis is a measurement of the flow velocity in m/s. A best-fit line is included as a reasonable approximation of the flow profile. Statistical and measurement uncertainties are indicated with error bars for a 95% confidence interval. The $R^2$ of this best-fit line is 0.9906, with Equation (4.15) displaying the best-fit line equation for mean *x* direction flow $\overline{U_x}(z)$.

$$\overline{U_x}(z) = -0.5873z - 0.2304 \tag{4.15}$$

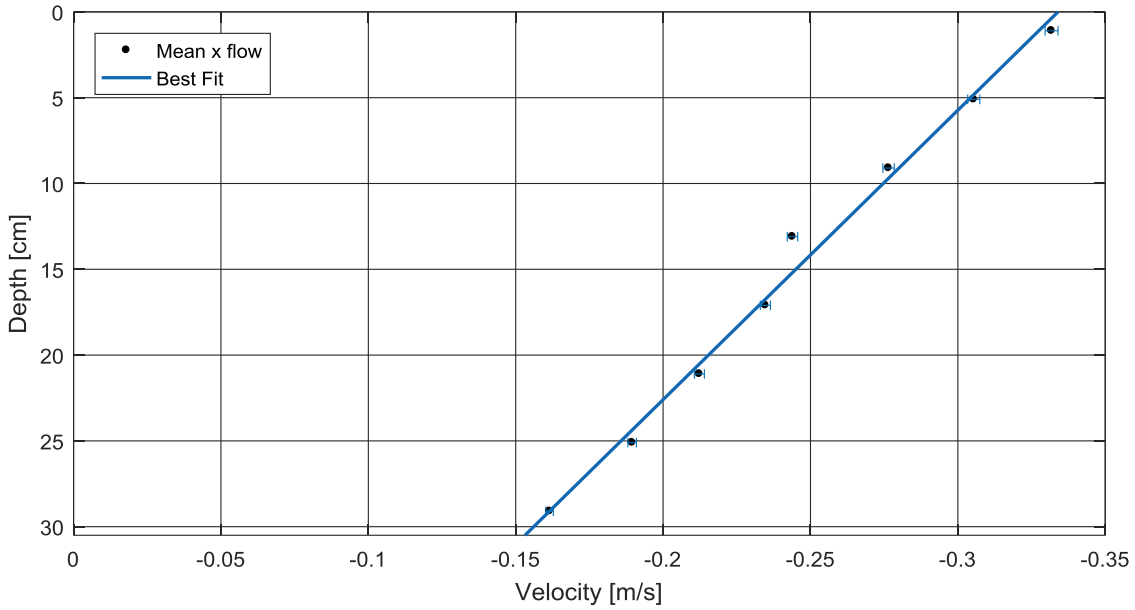


**Figure 4.9: Flow profile in flume tank.**

In addition to a changing mean flow speed as a function of depth, the Vectrino measured flow variance during the measurement period. The presence of such flow variance indicates that the flume tank produces some measurable turbulence within the stream. Figure 4.10 is a plot of the *x*, *y*, and *z* direction flow over the course of a two minute sampling period near the surface of the flume tank. The vertical axis represents the flow speed in m/s, while the horizontal axis represents the passage of time.

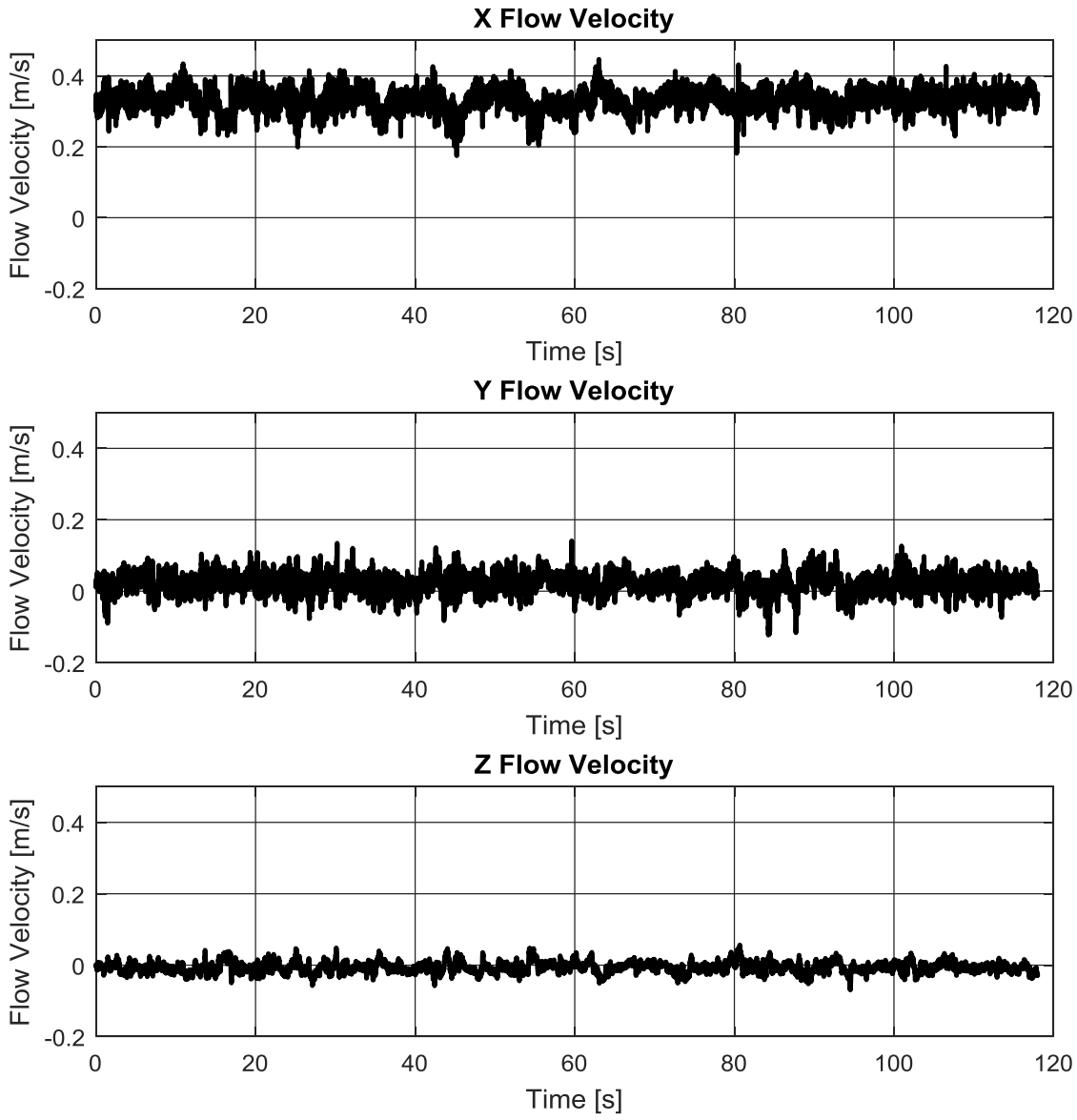


**Figure 4.10: Flume tank flow velocity in *x*, *y*, and *z* directions.**

From Figure 4.10, it is evident that the signal variance differs for each axis direction, as larger levels of signal variation can be observed in the *x* and *y* flow velocity plots than the *z* flow velocity plot. Figure 4.11 presents the flow variance for the *x*, *y*, and *z* directions as a function of depth. The vertical axis of Figure 4.11 indicates the depth beneath the flume tank water's surface in cm, while the horizontal axis of the figure indicates the magnitude of the standard deviation of the flow in m/s.

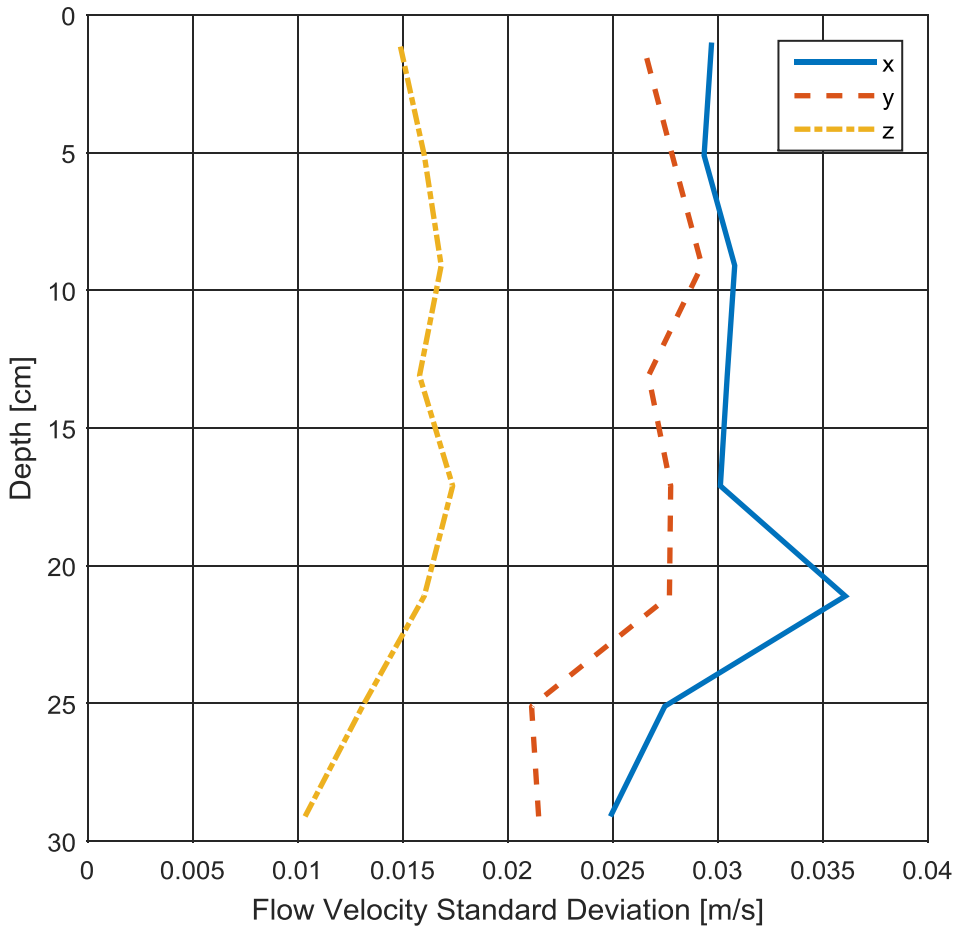


**Figure 4.11: Flow variation in world frame directions along the flume tank water column.**

The standard deviations of flow velocity in Figure 4.11 show no strong dependence on depth, particularly at depths ranging from 0 cm to 20 cm below the surface, which is where the towed sphere is frequently located throughout tests. A representative average variance value for each orthogonal direction can be used to describe the variance of flume tank flow in simulation.

To replicate turbulence in simulation, a frequency domain representation of the flow signal is useful. Figure 4.12 presents a spectral analysis of the *x* direction experimentally-measured flow signal for a constant shallow depth. Also presented in Figure 4.12 is a spectral analysis of an approximated flow signal, which was constructed through

combination of a white noise signal and a low-pass filter. The original signal displays a roll-off rate of approximately 10 dB/dec. beginning at about 0.2 Hz.

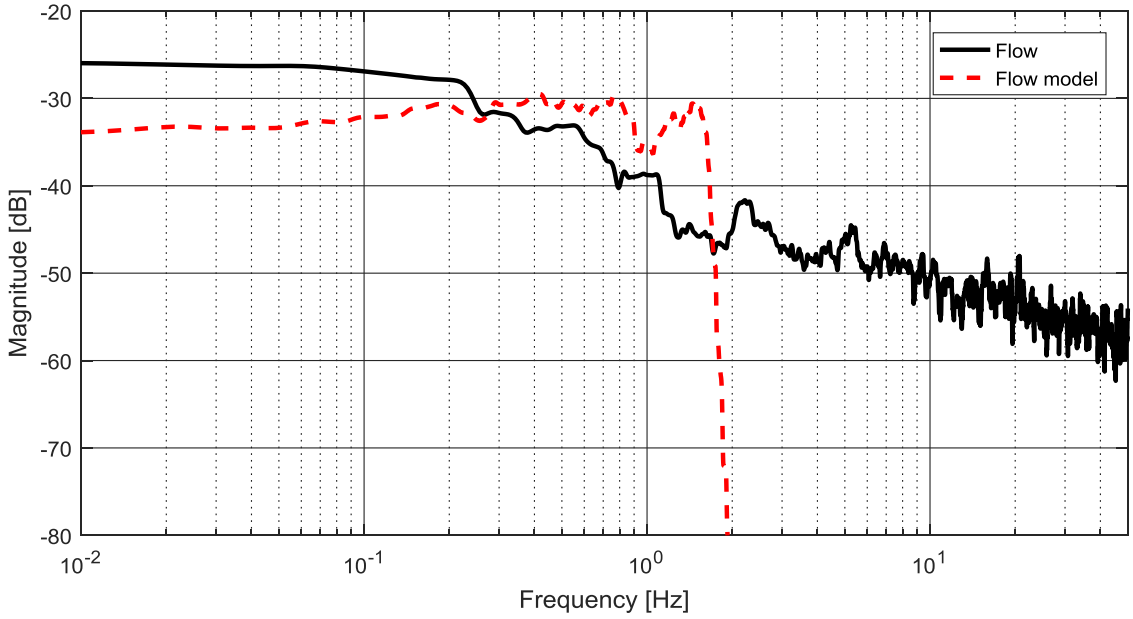


**Figure 4.12: Frequency spectrum of *x* direction velocity and simulated velocity signal.**

White noise is used as an approximation of the turbulence in simulation, as it has a flat frequency response that matches the low frequency behaviour of the flow signal depicted in Figure 4.12. A low-pass filter is applied to the white noise signal to truncate the flat frequency response at 3 Hz, which allows for the simulated flow signal to capture the low frequency components of the original signal. The magnitude contribution from signal frequency components higher than 3 Hz were 1% or less compared to the low frequency region. Additionally, turbulence effects at frequencies higher than 3 Hz were found to have very little impact on the flume-scale towed system through simulated tests. Following low-pass truncation, the flow model is scaled such that its signal variance is equivalent to the original signal. Flow model scaling is accomplished using three independent scaling factors for *x*, *y*, and *z* flow directions. As a result, the flow model under-predicts frequency components lower than 0.3 Hz and over-predicts frequency components from 0.3 Hz to 2 Hz, which is apparent in Figure 4.12. Increasing the three scaling factors to improve low frequency agreement led to excessive simulated turbulence effects, so the flow model variance was constrained to remain equivalent to

the measured flow signal variance. Figure 4.13 depicts a flow chart of the flow modeling process.

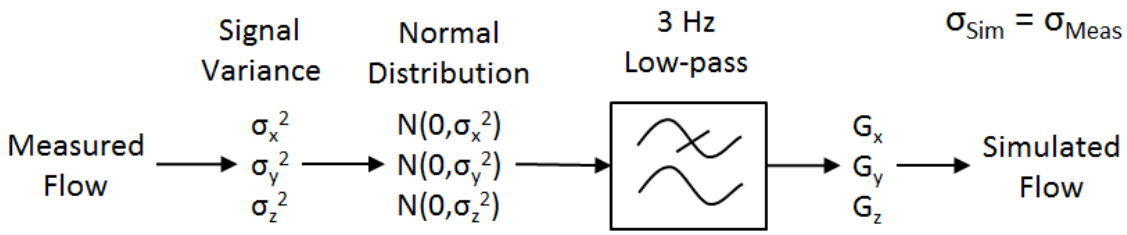


**Figure 4.13: Flowchart of procedure to obtain simulated flow signal.**

where $N(0, \sigma^2)$ represents a Gaussian distribution with a standard deviation $\sigma$, and $\sigma_x$, $\sigma_y$, $\sigma_z$ are 0.0300 m/s, 0.0262 m/s, and 0.0152 m/s, respectively. The scaling factors are $G_x$, $G_y$, and $G_z$, which are equal to 3.95, 4.88, and 4.31, respectively.

Equation (4.16) presents the application of the simulated noise signal for calculation of the relative flow velocity for fluid drag calculation on tow cable segments and the towed sphere for the *x*, *y*, and *z* directions:

$$\begin{bmatrix} U_x(\boldsymbol{s}) \\ U_y(\boldsymbol{s}) \\ U_z(\boldsymbol{s}) \end{bmatrix} = \begin{bmatrix} \overline{U_x}(z) \\ \overline{U_y}(z) \\ \overline{U_z}(z) \end{bmatrix} + LP(\boldsymbol{s}) \begin{bmatrix} G_x N(0, {\sigma_x}^2) \\ G_y N(0, {\sigma_y}^2) \\ G_z N(0, {\sigma_z}^2) \end{bmatrix} \tag{4.16}$$

where $U_x$, $U_y$, and $U_z$ represent the flow velocity in *x*, *y*, and *z* directions, and $\overline{U_x}(z)$, $\overline{U_y}(z)$, and $\overline{U_z}(z)$ are the mean flow velocities as a function of depth. The mean flow velocity $\overline{U_X}(z)$ is obtained from Equation (4.15), and $\overline{U_Y}(z)$ and $\overline{U_Z}(z)$ are set to zero. $LP(\boldsymbol{s})$ represents the low-pass filter which is used to truncate the noise signal in Figure 4.12. The low-pass filter used in the simulator is a Chebyshev II filter with 80 dB attenuation. Following the generation of the flow vector for each submerged cable segment and the towed sphere, the drag force described in Equation (4.13) was applied to the centre of gravity of each rigid object.

To manipulate the winch motion in simulation, the motion path recorded by the test mechanism encoders is applied to a Cartesian joint in Simscape. Figure 4.14 shows the winch positioning system.

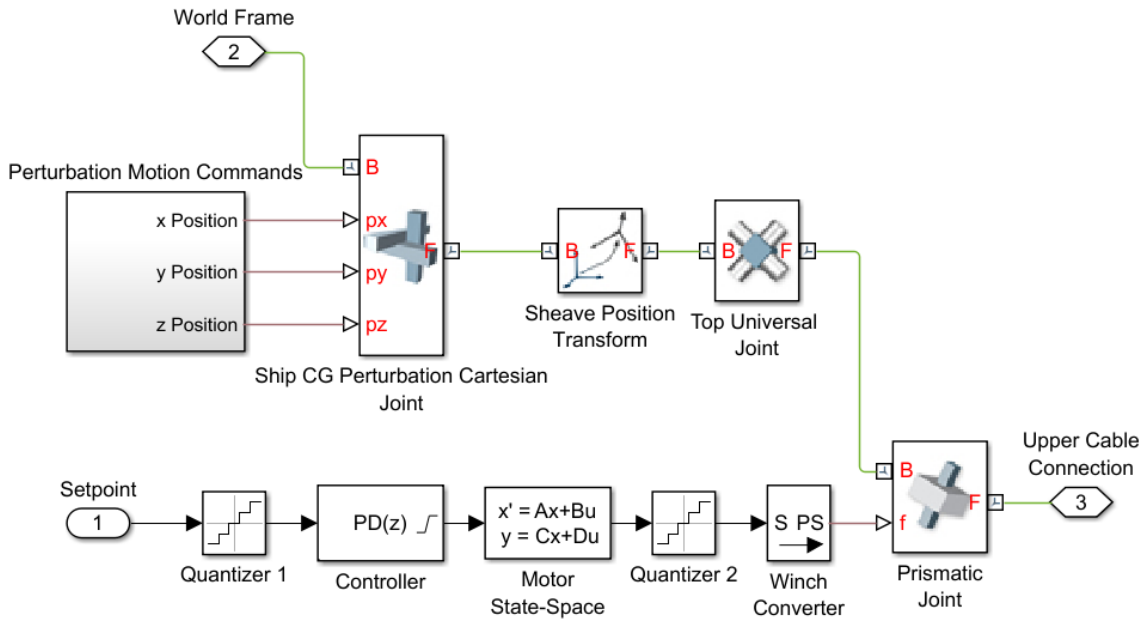


**Figure 4.14: Winch perturbation motion and reel command block diagram within Simulink.**

Referring to Figure 4.14, motion is recorded from the flume-scale test mechanism motor encoders and used to provide a motion input command to "Ship CG Perturbation Cartesian Joint" which moves the simulator winch relative to the world frame (indicated with port 2) using position inputs provided by the "Perturbation Motion Commands" subsystem.

To model the winch motor dynamics, the winch motor model which was identified in Section 3.3 is included in the flume-scale simulator. Figure 4.14 shows the feedback discrete PD controller in the flume-scale system operating at 1 kHz with a set-point provided by the set-point algorithm through port 1. Quantizer blocks are used to capture the resolution error of the winch motor encoder. The "Motor State-Space" block contains Equation (3.10).

To reel in and reel out the tow cable a prismatic joint connects the upper-most tow cable segment to the winch point as it moves along the motion path. Figure 4.14 displays how

the winch system is constructed in Simulink. The prismatic joint is extended or retracted in response to the winch motion signal provided by "Winch Converter" block and moves the uppermost cable segment with the "Upper Cable Connection" port 3.

Once the computer simulator was constructed in Simulink, simulations were carried out to verify the accuracy of the simulator and assess the set-point algorithms.

## 4.2. SIMULATION RESULTS

Results obtained by the flume-scale computer simulator are presented in this section. Section 4.2.1 describes the results obtained by the simulator in recreating the flume-scale test environment. Section 4.2.2 presents the results obtained when the test environment is modified to enhance the difference between the Simplified Sheave set-point algorithm and the Simplified Waterline set-point algorithm.

### 4.2.1. Flume Tank Simulation

The simulator results can be compared to the results obtained from the flume-scale experimental work to validate that the simulator is accurately capturing the towed sphere behaviour. Figure 4.15 illustrates the towed sphere motion in both simulation and with experimental results for the case of no imposed motion from the test mechanism. The vertical and horizontal directions on the plot correspond to locations in the test environment co-ordinate frame along the $z$ and $x$ axes, respectively. The only motion is a result of flume tank turbulence. In order to obtain an acceptable level of agreement between the simulator results and experimental data, the normal drag coefficient for the tow cable was reduced by 15% from the theoretical value to 0.85.

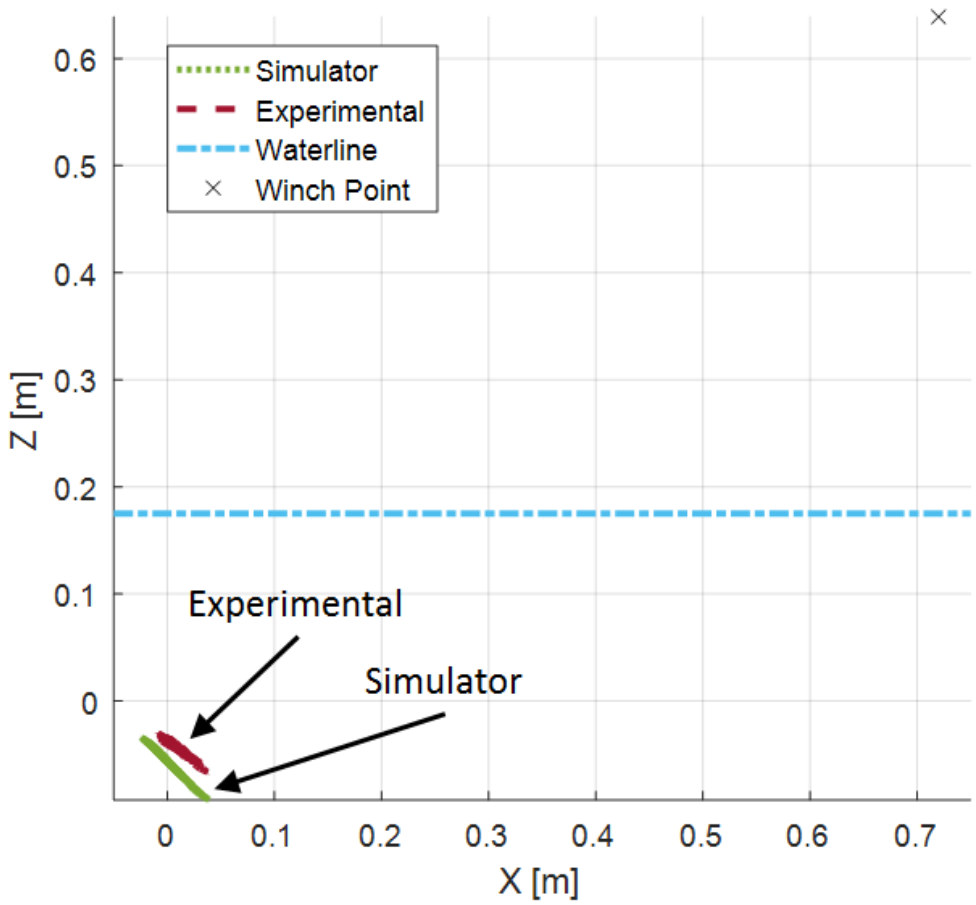


**Figure 4.15: Simulated and experimental towed sphere motion in the flume-scale test environment without test mechanism disturbance.**

Some disagreement between experimental results and simulator results can be observed in Figure 4.15. The centroids of both sphere traces are 1.2 cm apart, which is approximately 1.2% of the total tow cable length – a relatively small level of error. It can be observed that the simulated turbulence appears to impose motion along a more planar ellipsoid shape in simulation than in experimental results. Figure 4.16 shows the towed sphere motion traces in top, front, right, and isometric views within the test environment co-ordinate frame.

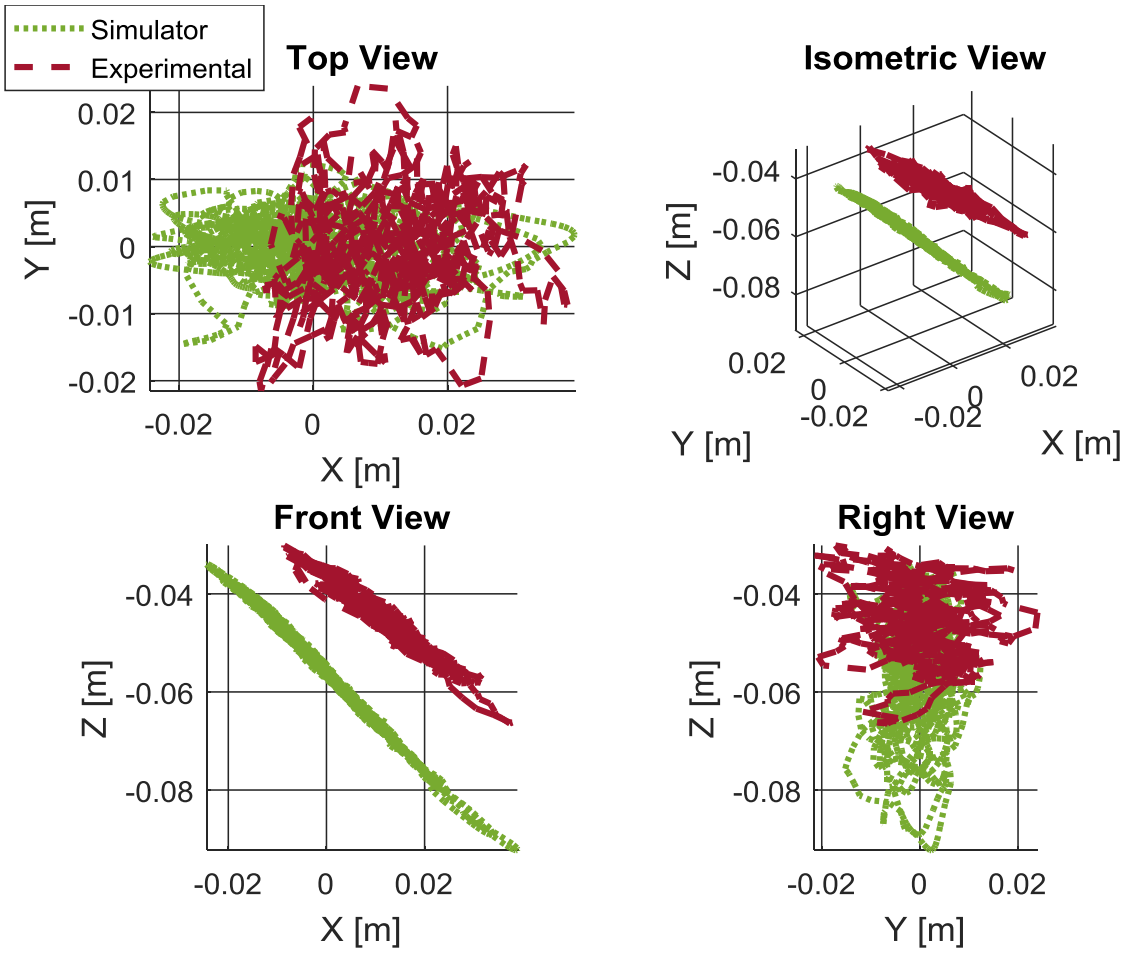


**Figure 4.16: Simulated and experimental towed sphere motion in front, right, top, and isometric views from the test environment co-ordinate frame without test mechanism disturbance.**

The towed sphere trace standard deviations can be examined to compare the dispersion of the traces along the three ellipsoid axes. Table 4.3 presents the standard deviation values along the ellipsoid axes as well as the ratio of experimental and simulated standard deviation values in order to assess the level of agreement between the two sets of results.

**Table 4.3: Standard deviation of towed sphere motion path in $X_E$, $Y_E$, and $Z_E$ directions for no test mechanism motion.**

| | Experimental | Simulator | $\frac{\text{Experimental}}{\text{Simulator}}$ |
|---|---|---|---|
| $X_E$ Direction Std. Dev. | 1.19 cm | 1.43 cm | 0.84 |
| $Y_E$ Direction Std. Dev. | 0.78 cm | 0.43 cm | 1.80 |
| $Z_E$ Direction Std. Dev. | 0.13 cm | 0.05 cm | 2.73 |

Table 4.3 indicates that the greatest disagreement between the simulated and experimental ellipsoid standard deviations is along the $Z_E$ axis, which is the shortest axis.

In addition to examining the test case with no winch or mechanism motion, an uncompensated trial can be compared to observe how the test mechanism motion affects movement of the towed sphere. Figure 4.17 illustrates the towed sphere motion in both simulation and with experimental results for the case of imposed motion from the test mechanism without an AHC system acting. The vertical and horizontal directions on the plot correspond to location in the test environment co-ordinate frame along the *z* and *x* axes, respectively.

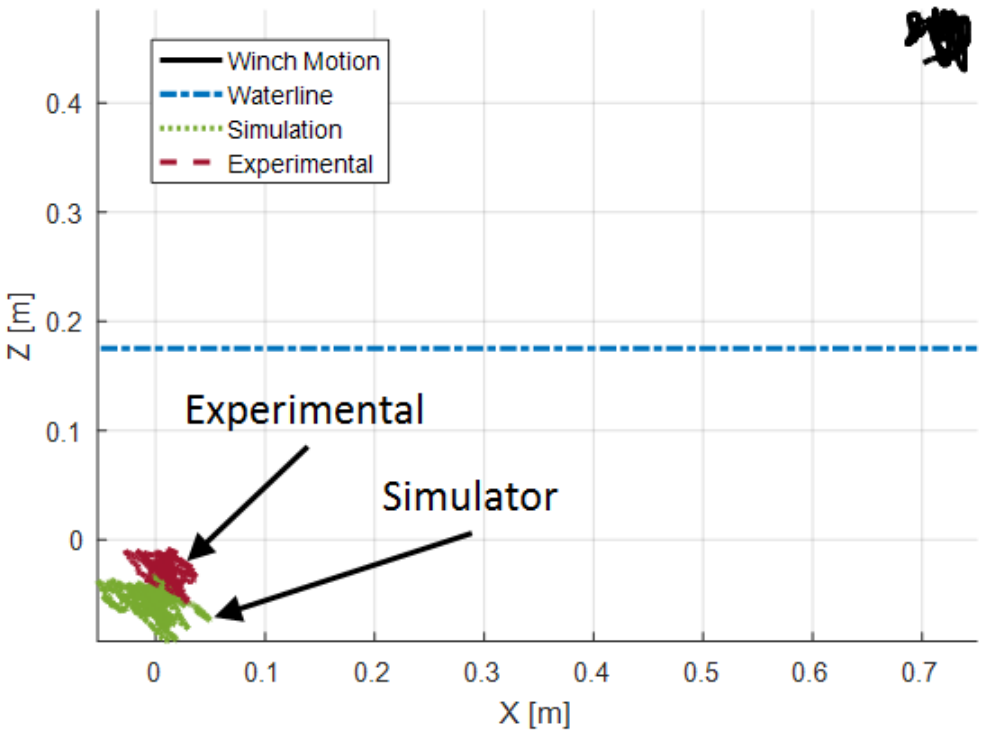


**Figure 4.17: Simulated and experimental towed sphere motion in the flume-scale test environment with test mechanism disturbance and no AHC system.**

Test mechanism motion results in similar towed sphere motion paths in the uncompensated case. Figure 4.18 shows the towed sphere motion traces in top, front, right, and isometric views within the test environment co-ordinate frame.

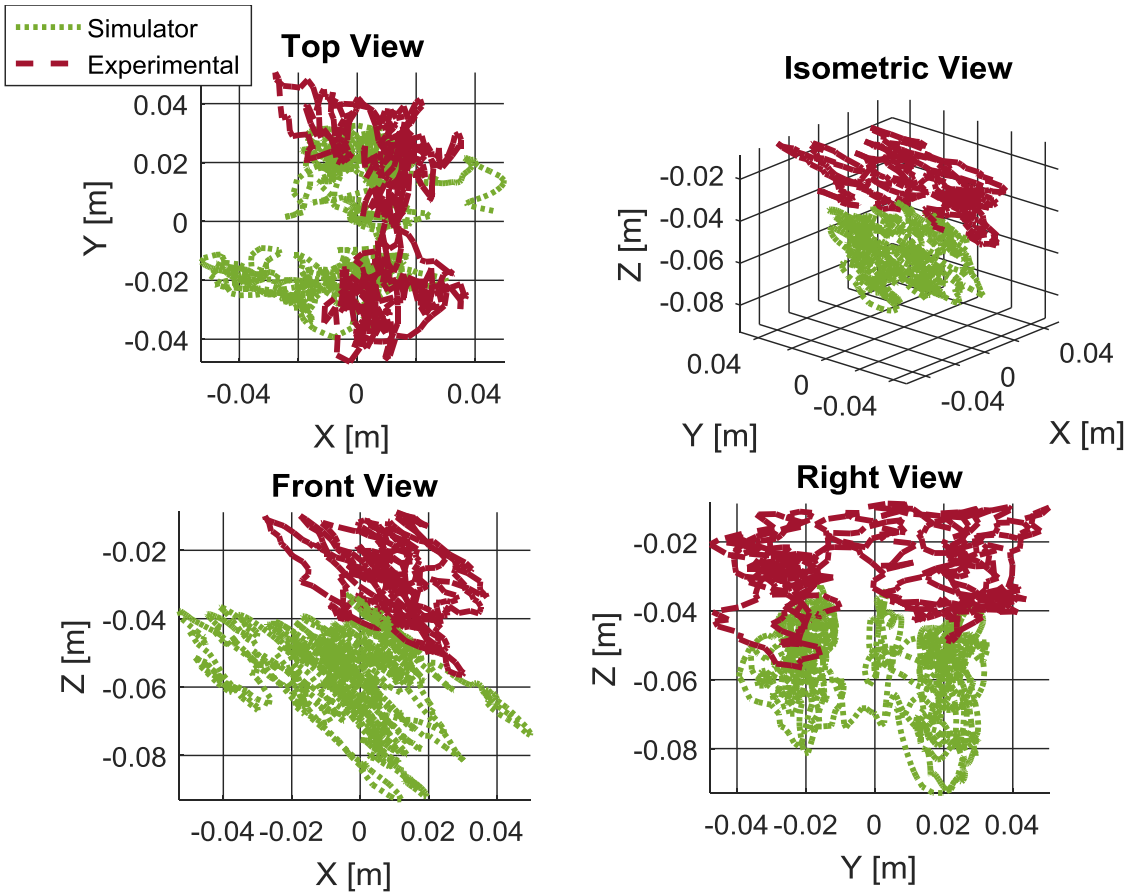


**Figure 4.18: Simulated and experimental towed sphere motion in front, right, top, and isometric views from the test environment co-ordinate frame with test mechanism disturbance and no AHC system.**

Upon inspection, experimental and simulated motion paths appear to agree well when disturbance motion is included in the simulation. Table 4.4 compares the standard deviation of the simulated and experimental towed sphere motion path along the ellipsoid axes.

**Table 4.4: Standard deviation of towed sphere motion path in $X_E$, $Y_E$, and $Z_E$ directions for uncompensated motion case.**

| | Experimental | Simulator | $\frac{\text{Experimental}}{\text{Simulator}}$ |
|---|---|---|---|
| $X_E$ Direction Std. Dev. | 2.20 cm | 2.73 cm | 0.81 |
| $Y_E$ Direction Std. Dev. | 1.42 cm | 1.36 cm | 1.04 |
| $Z_E$ Direction Std. Dev. | 1.05 cm | 0.88 cm | 1.19 |

Figure 4.19 illustrates the motion of the towed sphere when the Rigorous Sheave algorithm is enabled to compensate for the test mechanism motion.

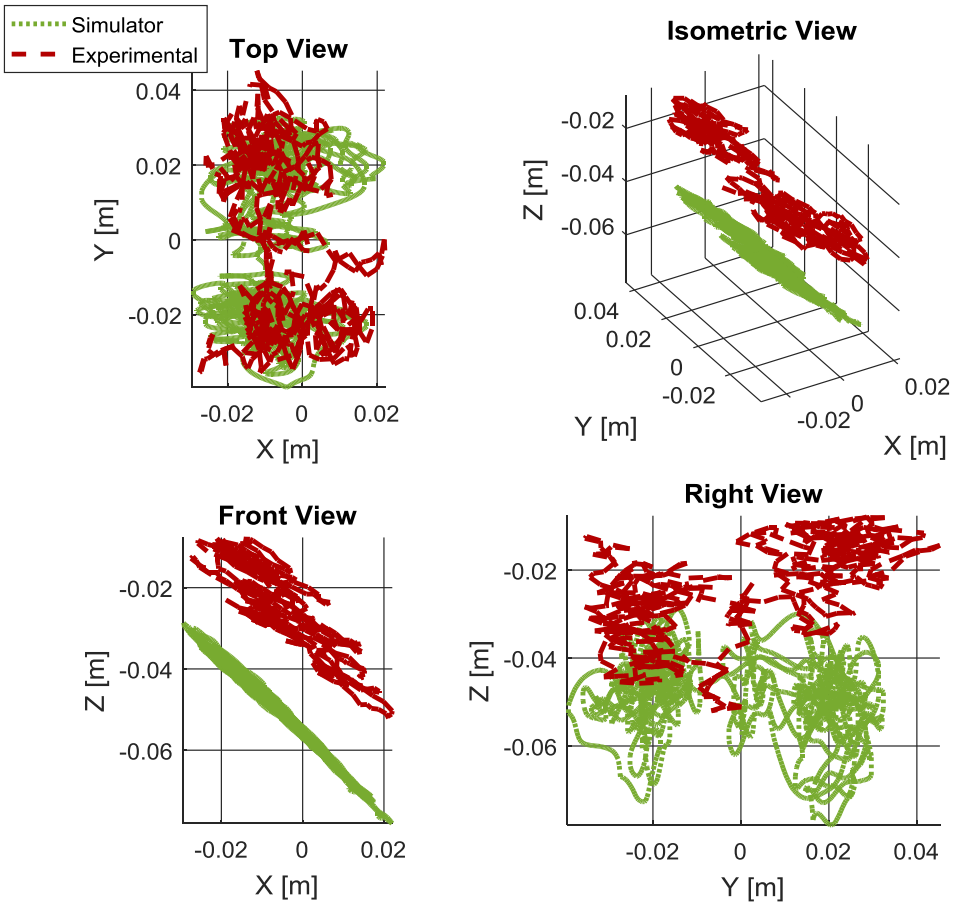


**Figure 4.19: Simulated and experimental towed sphere motion in front, right, top, and isometric views from the test environment co-ordinate frame with test mechanism disturbance and AHC operating under the Rigorous Sheave algorithm.**

Upon inspection, the motion paths presented in Figure 4.19 appear to agree well along the $X_E$ and $Y_E$ axes. The $Z_E$ axis appears to have some disagreement between the experimental and simulated cases, which is consistent with the results obtained from the case without test mechanism motion. Table 4.5 displays the standard deviation values of the motion paths along each ellipsoid axis.

**Table 4.5: Standard deviation of towed sphere motion path in $X_E$, $Y_E$, and $Z_E$ directions for Rigorous Sheave set-point algorithm case.**

| | Experimental | Simulator | $\frac{\text{Experimental}}{\text{Simulator}}$ |
|---|---|---|---|
| $X_E$ Direction Std. Dev. | 2.42 cm | 2.08 cm | 1.16 |
| $Y_E$ Direction Std. Dev. | 1.15 cm | 1.15 cm | 1.00 |
| $Z_E$ Direction Std. Dev. | 0.28 cm | 0.06 cm | 4.67 |

Table 4.5 confirms a relatively large disparity along the $Z_E$ axis between the simulated and experimental results. The simulated value is only slightly larger than the case without test mechanism motion.

Comparing the ellipsoid volumes for the full range of test cases provides a complete representation of the set-point algorithm performance in simulation. Figure 4.20 displays the simulated ellipsoid volumes along with the experimental results for the various algorithms. The Rigorous Waterline algorithm, which was unstable in experiments, proved to be unstable in simulation, so it is neglected from Figure 4.20.

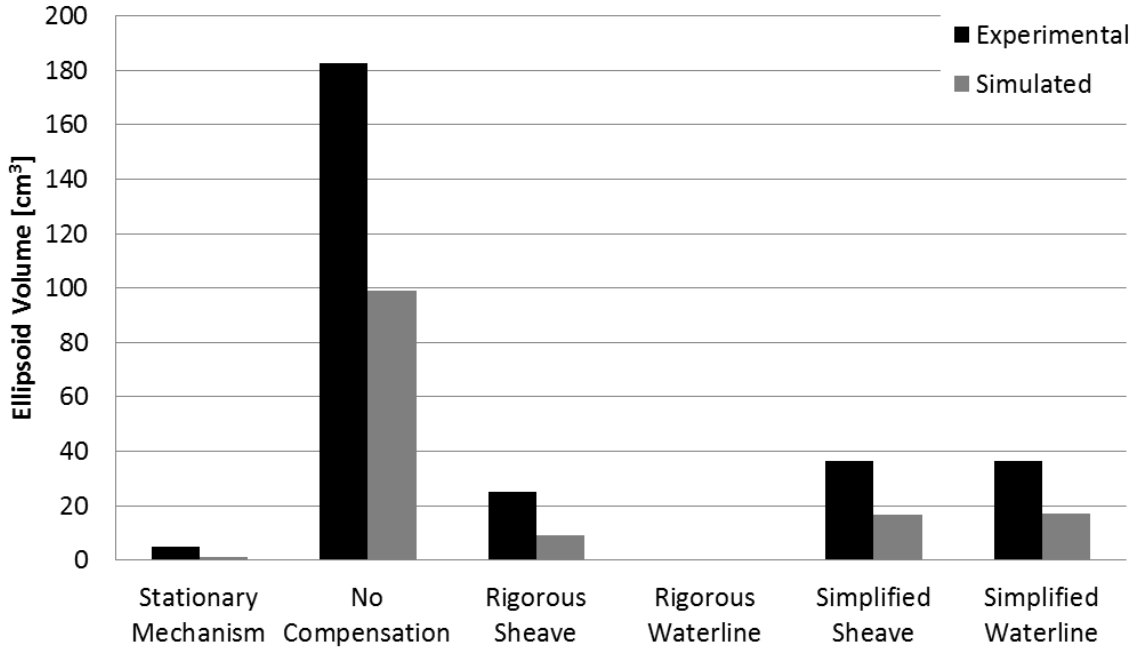


**Figure 4.20: Ellipsoid volume for experimental and simulated flume-scale results.**

Figure 4.20 indicates that the simulated ellipsoid volumes are consistently smaller than experimental results. For all of the test cases, simulated ellipsoid volume is approximately half of the experimental results. The reason for this difference is potentially oversimplification of turbulence effects. The test case pictured in Figure 4.16 without imposed disturbance motion allows for a direct comparison between the simulated towed sphere and the experimental test results in response to turbulence. The white noise model of turbulence is a potential source for the disagreement between the experimental results and the simulated results.

Figure 4.21 summarizes the set-point algorithm performances in simulation and experimentation in terms of ellipsoid volume reduction. Ellipsoid volume reduction is computed by comparing the compensated volume to the uncompensated volume for all experimental cases and for all simulated cases.

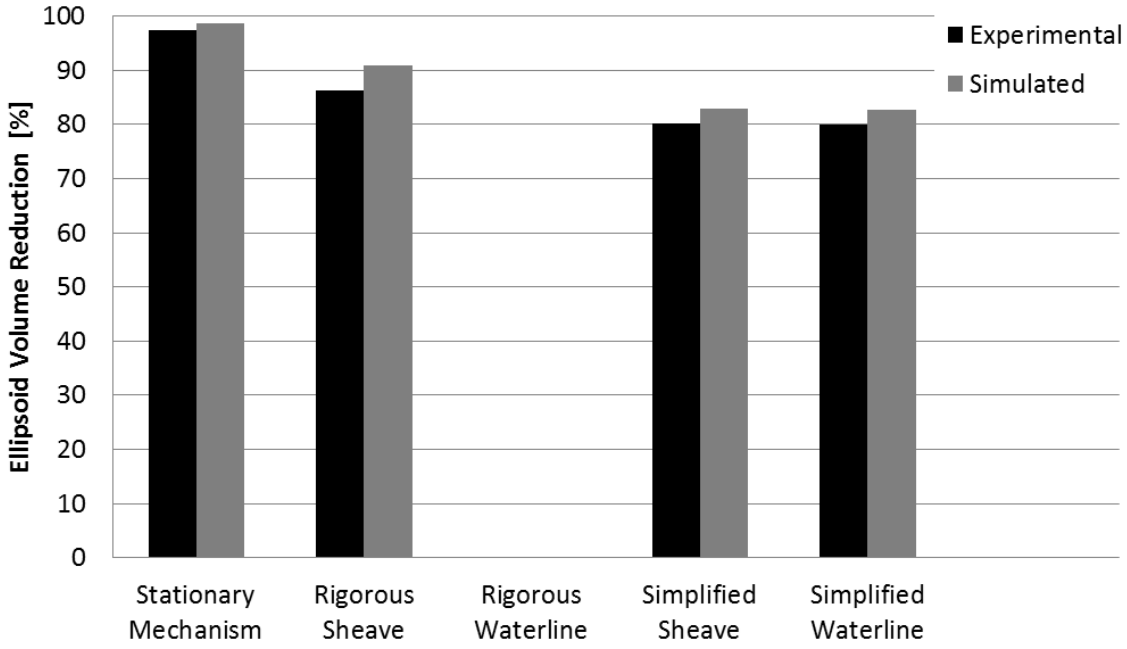


**Figure 4.21: Ellipsoid volume reduction compared to uncompensated case for experimental and simulated flume-scale results.**

Figure 4.21 indicates that ellipsoid volume reduction agrees well. Additionally, simulated AHC systems appear to perform better than experimental versions. This result is due to

the $Z_E$ standard deviation values which are significantly smaller in simulation than in experimentation, as shown in Table 4.5.

The same trend of performance in all of the set-point algorithms was observed in experimentation and simulation. The Rigorous Sheave algorithm reduced towed body motion by 90%, performing the best. Additionally, the Rigorous Waterline algorithm proved to be unstable in simulation, which was also observed in experimental results. The Simplified Waterline and Simplified Sheave algorithms performed identically, reducing the ellipsoid volume by 83% in simulated tests. Section 4.2.2 presents simulated results in a test environment with alternate geometry to highlight the differences between the two Simplified Sheave and Simplified Waterline algorithms.

### 4.2.2. Alternate Geometry Test Environment

Due to limitations of the test environment, Simplified Sheave and Simplified Waterline methods performed identically. In simulation, the test mechanism parameters can be altered so that the winch is closer to the waterline. The nominal sheave height is lowered from 46 cm to 17 cm. Peak-to-peak vertical disturbance motion is approximately 7 cm, or 41% of the vertical offset. If a towed system were mounted to the stern of an FFG-7 vessel studied in the Australian DSTO report [49], a vertical offset of 8.2 m could be expected, with a vertical range of motion of 4 m, or 48% of the vertical offset. By altering the geometry of the simulated test environment in this way, the Simplified algorithm results are more likely to be representative of full-scale behaviour.

In addition to altering the geometry of the test environment, exterior effects on the towed system were removed to isolate the towed system as much as possible. Winch dynamics and the PD controller were removed from the simulator by actuating the winch directly with position control of the prismatic joint simulating winch actuation. Additionally, turbulence was removed from the simulator by simplifying the flow profile to the mean flow $\overline{U_x}(z)$. Figure 4.22 presents the results of the alternative geometry test environment.

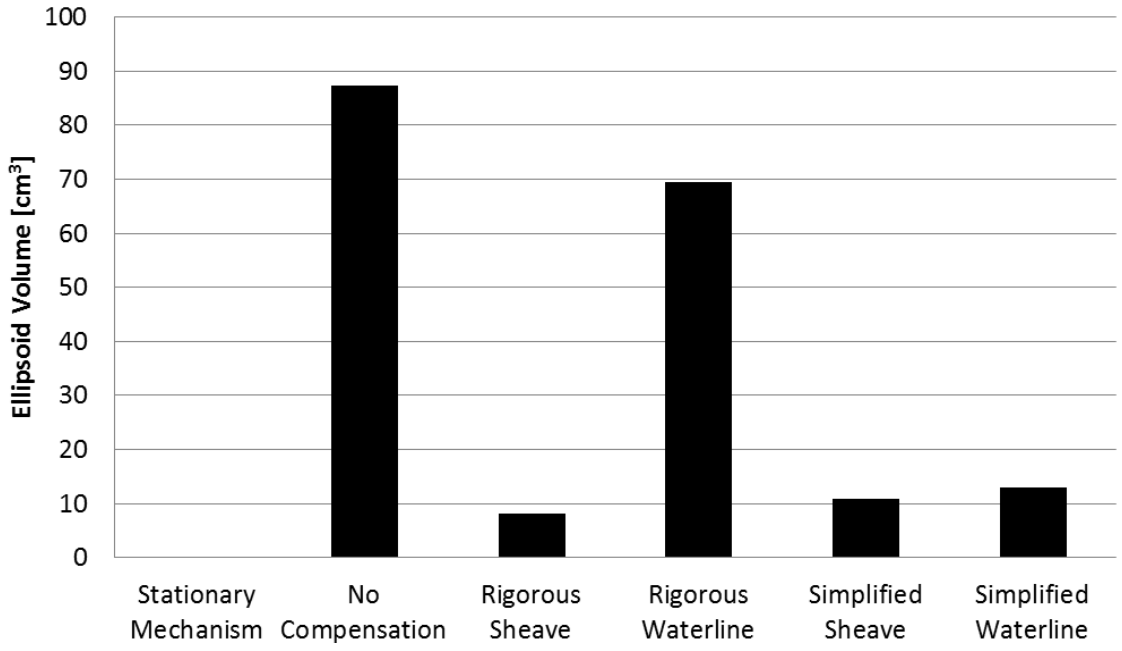


**Figure 4.22: Ellipsoid volume for the alternative geometry simulated flume-scale results.**

The Rigorous Sheave set-point algorithm still performed the best in the alternative geometry simulation, reducing ellipsoid volume by 91% compared to the uncompensated case. The improvement in performance of the Rigorous Sheave algorithm was, however, reduced compared to the Simplified Sheave algorithm in the alternative geometry case. The original geometry produced an improvement of 7% by applying the Rigorous formulation of the Sheave algorithm, while the alternative geometry reduces this improvement to only 3%. The reduction in performance in this rescaled geometry indicates that the benefit of real-time sheave angle measurement might be reduced in full-scale situations.

A difference is noticeable between the Simplified Sheave algorithm and the Simplified Waterline algorithm in Figure 4.22, with the Simplified Sheave algorithm reducing ellipsoid volume by 88% compared to the uncompensated motion case and the Simplified Waterline algorithm reducing ellipsoid volume by 85% compared to the uncompensated motion case. The increasing difference between the two Simplified algorithms indicate that in the Simplified Sheave algorithm might perform better than the Simplified Waterline algorithm in full-scale applications.

The stationary mechanism case produced no towed body motion, as turbulence was removed from the simulator. The Rigorous Waterline algorithm remained partially stable throughout the simulation, but small changes in sheave angle still provoked large set-point responses. Despite the erratic behaviour of the Rigorous Waterline algorithm, it was able to reduce ellipsoid volume by 21%.

## 4.3. SUMMARY

The creation of a simulator to study the performance of the different set-point algorithms contributes toward the second and third key objectives of this thesis. By studying the set-point algorithms in simulation, the test environment can be altered to more accurately reflect real-world conditions and geometry.

Results from flume tank simulation indicate the same trends as experimental results, with the Rigorous Sheave algorithm performing best amongst the set-point algorithms, reducing ellipsoid volume compared to the uncompensated case in the original experimental geometry and the alternative geometry result by 90% and 91%, respectively. The Rigorous Waterline algorithm exhibited instabilities which was consistent with experimental results. Simplified Sheave and Simplified Waterline algorithms performed the same in the simulated test environment, which was also observed experimentally.

The alternative geometry test environment allowed for re-examination of the various set-point algorithms with a lowered winch. A reduced vertical offset of the winch above the waterline presents a more accurately scaled towed system. Increased performance of the Simplified Sheave algorithm in the alternative geometry tests indicates that for a full-scale system, the Simplified Sheave algorithm might provide better performance than the Simplified Waterline algorithm. Additionally, the benefit of real-time sheave angle measurement for the Sheave algorithm appeared to decrease with the alternative geometry simulations. Decreased performance of the Rigorous Sheave algorithm compared to the Simplified Sheave algorithm suggests that for a full-scale system, real-time sheave angle measurements might not be necessary in order to achieve good heave

compensation in full-scale applications. To further investigate these results, a full-scale simulation is carried out in Chapter 5.

# CHAPTER 5 FULL-SCALE COMPUTER SIMULATION

This chapter describes the development of a full-scale simulator which is used to examine the performance of the four set-point algorithm approaches. The simulator used for full-scale investigation was adapted from the previous flume-scale version. MATLAB and Simulink are used to construct the simulator using the Simscape mechanical libraries.

Section 5.1 describes the differences between the full-scale simulator and the small-scale version. Section 5.2 presents the simulator results, comparing the various set-point algorithms for several towed system parameters, contributing towards the second and third key objectives of this thesis. Finally, Section 5.3 summarizes the results.

## 5.1. FULL-SCALE SIMULATOR

The flume-scale simulator described in Chapter 4 was adapted to create a full-scale simulator. In order to adapt the flume-scale simulator for the full-scale application, the flume tank flow profile and turbulence effects were replaced with a constant 3.66 m/s $x$ direction velocity obtained from the Australian DSTO report [49]. Table 5.1 provides the towed system parameters which were used to create the full-scale simulator. Tow cable parameters presented in Sun et al. [38] were used for the full-scale tow cable parameters. Towed body parameters, such as towed body buoyant force and frontal area were adapted from Walton and Brillhart [60] and used to provide the simulator with the remaining towed system parameters.

**Table 5.1: Parameters for full-scale simulator adapted from Sun et al. [38], Walton and Brillhard [60], and Munson et al. [59].**

| Parameter | Symbol | Value | Reference |
|---|---|---|---|
| Cable Length | $l_{Tot}$ | 460 m | [38] |
| Cable Drag Coefficient | $C_d$ | 1.80 | [38] |
| Cable Mass | $m$ | 5.2 kg/m | [60] |
| Cable Elasticity | $K_T$ | 1.141 MN/m | [38] |
| Towed Body Mass | $m_S$ | 1734 kg | [60] |
| Towed Body Radius | $r_S$ | 0.45 m | [60] |
| Towed Body Drag Coefficient | $C_s$ | 0.5 | [59] |
| Sheave Position Translation from ship CG | | (-62,0,8.2) m | [49] |

Similar to the flume-scale simulator, the full-scale simulator uses a towed sphere as a generalized towed body shape. This approach also is used by Kamman and Huston [48] for their full-scale study.

Ship perturbation motion is included in the simulation as depicted in Figure 5.1. Ship motion in six degrees of freedom is taken directly from the Australian DSTO report [49] and applied to a Cartesian joint and gimbal joint at the ship's centre of gravity, which is the full-scale simulation origin frame. A horizontal and vertical offset along the *x* and *z* axes, respectively, is applied. This offset is implemented with a translation block entitled "Sheave Position Transform" in Figure 5.1. The offset locates the towed system sheave at the stern of the vessel, 1.5 m above the deck.

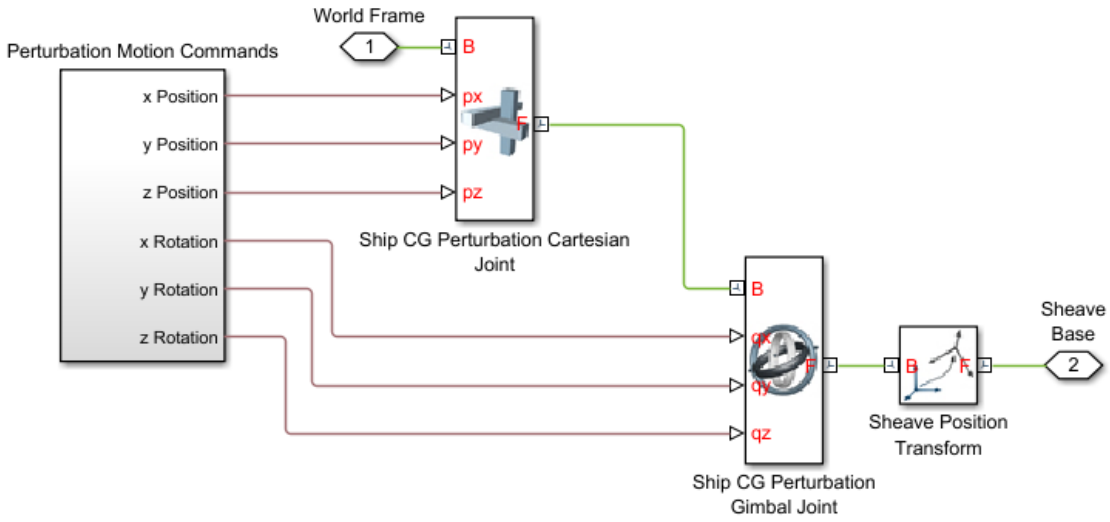


**Figure 5.1: Ship disturbance through Cartesian and gimbal joints.**

Figure 5.2 shows the ship perturbation motion which was digitized from the Australian DSTO report [49] and used for the full-scale simulation.

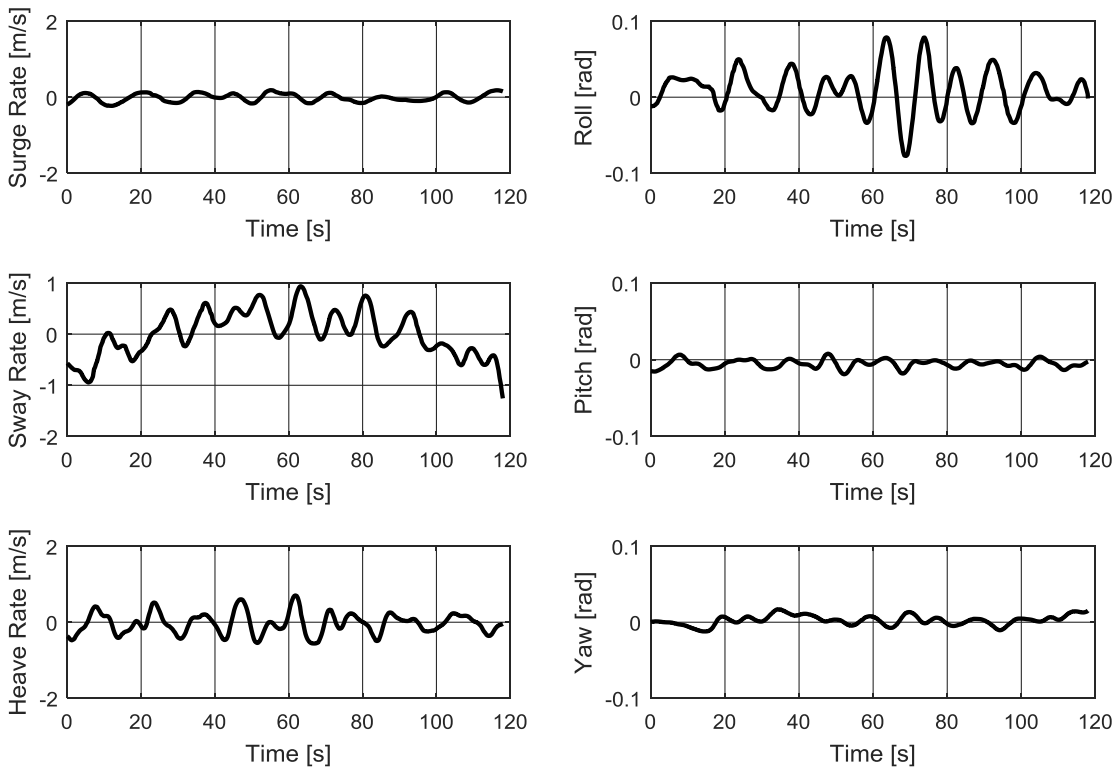


**Figure 5.2: Ship perturbation motion digitized from DSTO report [49].**

Zhu et al. [61], Sun et al. [38], Hover et al. [12], Howell [34], and Driscoll et al. [39] describe and justify the assumption that tensile cable strain dominates curvature strain in full-scale high tension towed applications. As a result, rotational stiffness and damping can be neglected for the full-scale simulator, and tangential stiffness is included instead. With respect to the corresponding tangential damping, Driscoll et al. [39] and Hover et al. [12] introduce damping effects into their models through fluid drag. Because of the dominant effect of fluid drag on the system, internal damping within the tow cable is neglected from the simulator. Driscoll et al. [39] describe tensile cable segment stiffness according to Equation (5.1):

$$K_T = \frac{EA}{l_i} \tag{5.1}$$

where $l_i$ is the length of each cable segment and $EA$ is obtained from Sun et al. [38]. Cable segment elasticity is presented in Table 5.1. Figure 5.3 shows how tangential

stiffness is included into the simulator model for each cable segment with a linear spring. The separation of cable segments is exaggerated for illustrative purposes.

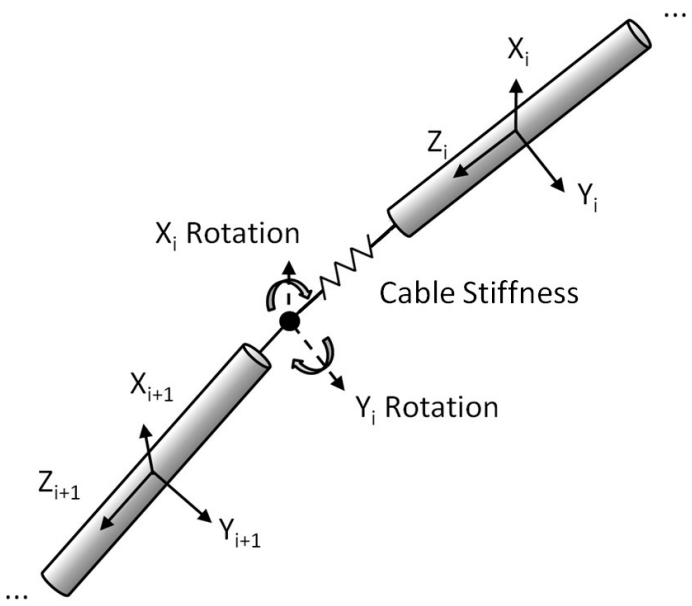


**Figure 5.3: Interconnection between rigid cable segments in full-scale simulation including tensile cable stiffness.**

Tangential stiffness is included into the model along the cable segment *z* axis. Modelling tangential stiffness is accomplished in Simulink with the addition of a prismatic joint, as depicted in Figure 5.4. The prismatic joint allows translation along the cable segment $z_i$ axis and includes a stiffness parameter for inclusion of a linear spring along the prismatic joint translation.

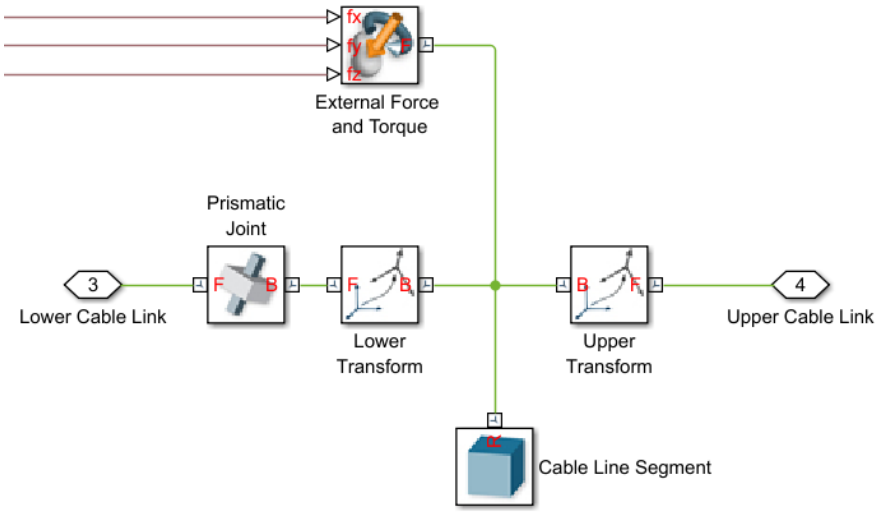


**Figure 5.4: Computer simulator implementation of tangential stiffness in cable model.**

It is desirable to study the performance of the set-point algorithms with a range of towed system parameters at full-scale in order to obtain a general sense of the relative performance of the algorithms. The parameters listed in Table 5.1 are used as a nominal configuration of a full-scale towed system. Additional configurations are listed in Table 5.2.

**Table 5.2: Summary of full-scale test case parameters.**

| | Test Case | | | | | | |
|---|---|---|---|---|---|---|---|
| Parameter | Nominal | A | B | C | D | E | F |
| Tow Cable Length | 460 m | 460 m | 460 m | 460 m | 460 m | 230 m | 100 m |
| Towed Body Mass | 1734 kg | 3468 kg | 867 kg | 1734 kg | 1734 kg | 1734 kg | 1734 kg |
| Tow Cable $C_d$ | 1.8 | 1.8 | 1.8 | 0.9 | 2.7 | 1.8 | 1.8 |

The test cases presented in Table 5.2 consist of three different tow cable lengths, towed body masses, and tow cable drag coefficients. The first test case is the nominal configuration. Test cases A and B have towed body mass values which are 50% and 200% of the nominal value, respectively. Test cases C and D have tow cable drag coefficients which are 50% and 150% of the nominal value, respectively. Finally, test cases E and F have increasingly shorter tow cable lengths of 230 m and 100 m,

respectively. The performance of the various set-point algorithms is compared for the different towed system configurations listed in Table 5.2.

## 5.2. RESULTS

Full-scale simulations were carried out with the towed parameters presented in Table 5.2. The nominal results are presented along with the other test cases in Section 5.2.1. In Section 5.2.2, the Simplified Sheave method is examined for its sensitivity to nominal sheave angle error.

### 5.2.1. Test Case Results

The test cases presented in Table 5.2 provide a range of different tow cable profiles under the waterline. Figure 5.5 displays how the tow cable profile changes between the different test cases. The vertical and horizontal directions on the plot correspond to displacement from the host vessel centre of gravity along the $x$ and $z$ directions, respectively. For the tow cables presented in Figure 5.5, no ship disturbance is applied in simulation, so that the tow cables assume their steady-state curvature.

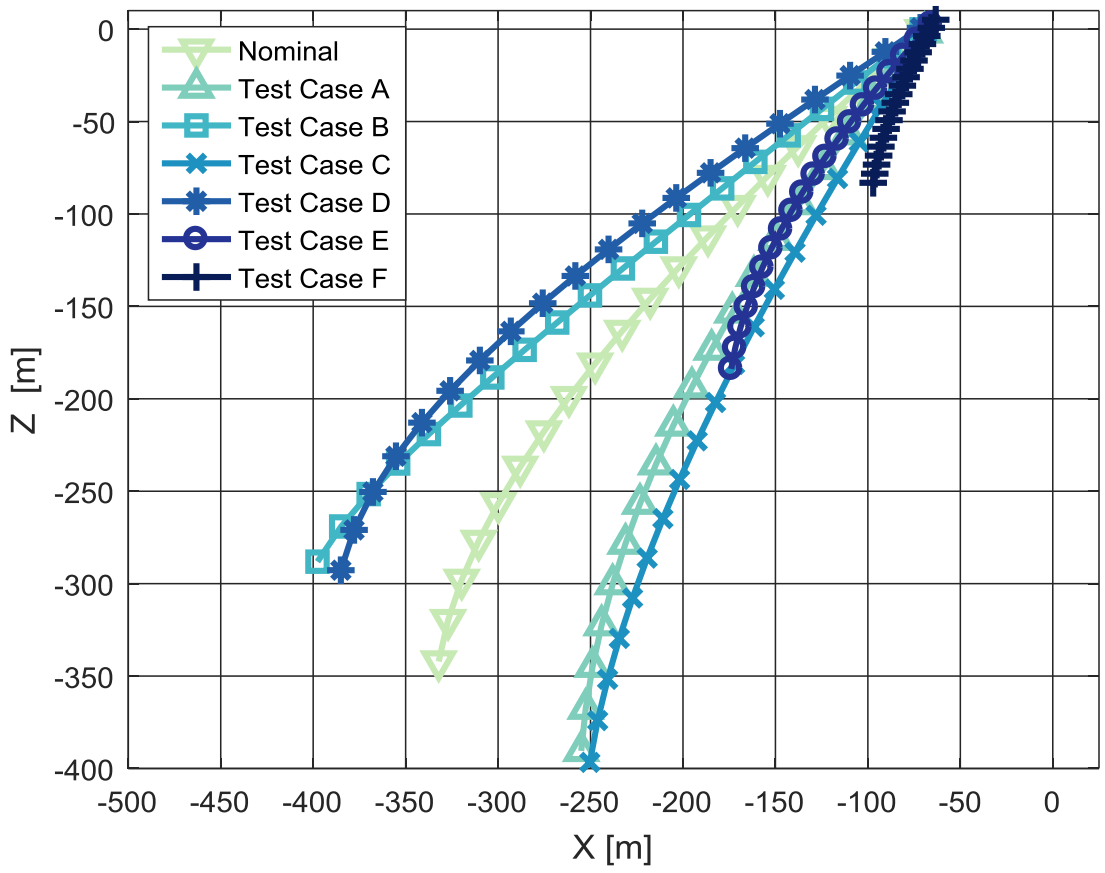


**Figure 5.5: Steady-state tow cable profiles for all full-scale test cases.**

Test cases A and C have roughly similar tow cable profiles, resulting from an increase in towed body mass and a decrease in tow cable drag, respectively. Test cases B and D also have somewhat similar tow cable profiles, resulting from a decrease in towed body mass and an increase in tow cable drag.

Following simulations with the range of tow system parameters, the associated ellipsoid volume results were computed. Figure 5.6 shows a plot comparing all of the ellipsoid volumes for the different test cases and set-point algorithms.

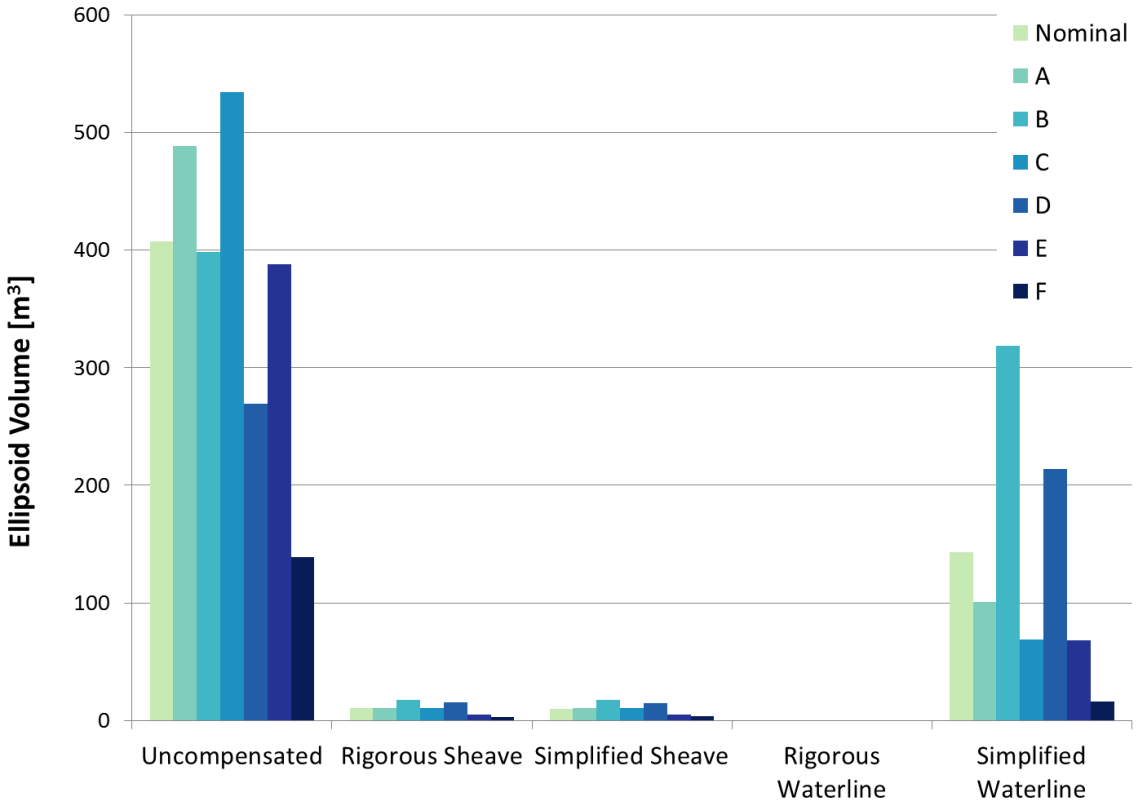


**Figure 5.6: Comparison of set-point algorithms for various test cases at full-scale.**

As with flume-scale simulation, the Rigorous Sheave and Simplified Sheave algorithms performed best for all test cases. The Rigorous Waterline algorithm exhibited instability again in full-scale simulation. For all test cases, the Simplified Waterline set-point algorithm performed worse than both Sheave algorithms.

In reeling in and out tow cable, corrective action is only being taken along the vector formed by the current tow cable as it travels from the sheave to the waterline. The Sheave set-point algorithm only attempts to correct for host vessel motion along this vector. By contrast, the Waterline algorithm assumes that it is possible to maintain steady-state behaviour for the entire submerged towed system by ensuring that the same location on the tow cable crosses the waterline at all times. Theoretically, this method would require a tow cable discontinuity as it crosses the waterline. This means that as the host vessel is deviating from the unperturbed trajectory, the Waterline algorithm is attempting to impose a discontinuous condition on the tow cable. An illustration of the tow cable discontinuity is indicated in Figure 5.7. It is likely for these reasons that the Sheave

algorithm effectively reduces towed body motion while the rigorous Waterline algorithm is unstable in many applications.

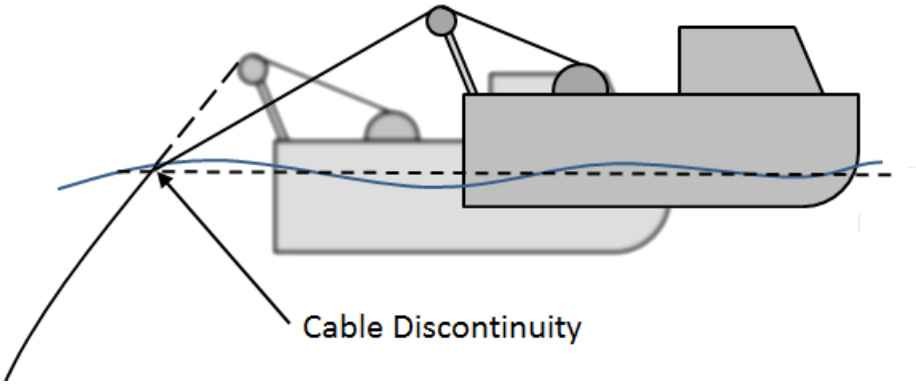


**Figure 5.7: Cable discontinuity required for proper implementation of Waterline set-point algorithm.**

Figure 5.6 indicates that as tow cable length decreases, the performance of the Simplified Waterline algorithm improves and eventually approaches the performance of the Simplified Sheave algorithm. For the nominal case, the ellipsoid volume of the Simplified Waterline algorithm is 14 times larger than the ellipsoid volume of the Simplified Sheave algorithm. This ratio is reduced to approximately 4.5 for the 100 m tow cable in test case F. This trend linking tow cable length and similarity between Simplified Sheave and Simplified Waterline algorithms agrees with results from small-scale experimental and simulation work. In the flume-scale experimental results, the tow cable length was relatively smaller than the 100 m test case presented in this chapter. If the sheave height is used as a scaling factor, the relative tow cable length for the flume-scale experimental results with alternative geometry is only 34 m. With this relatively small tow cable length, the ellipsoid volume of the Simplified Waterline algorithm is only 1.3 times larger than the ellipsoid volume of the Simplified Sheave algorithm.

Test cases presented in Figure 5.6 do not include the performance of the Rigorous Sheave algorithm. This algorithm demonstrated instabilities in full-scale simulation. As a result of its frequent instabilities throughout all test environments, it is not recommended that the Rigorous Waterline algorithm be pursued further.

The performance of the Simplified Sheave algorithm depends on the quality of the assumption that the sheave angle is a constant, nominal value. Throughout the full-scale tests, the performance of the Simplified Sheave algorithm was practically identical to that of the Rigorous Sheave algorithm. Sheave angle variation proved to be reduced during full-scale tests over small-scale tests, which did show a difference between the Simplified and Rigorous Sheave algorithms. The standard deviation of the sheave angle was 0.9 degrees over the course of the nominal test case at full scale, while it was 2.7 degrees in small-scale tests. Reduction of sheave angle variation at full-scale has led to increased performance of the Simplified Sheave algorithm.

### 5.2.2. Error Sensitivity

Consistently good performance of the Simplified Sheave algorithm raises a question regarding the performance of this method under circumstances where the nominal sheave angle is assigned incorrectly. Simulations were carried out with a range of error values inserted into the set-point algorithm in order to assess the robustness of this method. Equation (5.2) demonstrates how angle measurement error is inserted into the Simplified Sheave set-point algorithm.

$$SP = (\Delta x)\sin(\theta_{nom} + ERROR) + (\Delta z)\cos(\theta_{nom} + ERROR) \tag{5.2}$$

Figure 5.8 shows the performance of the Simplified Sheave set-point algorithm with significant error introduced for the nominal towed system configuration. Each column presented in the figure indicates the level of error which was introduced into the set-point calculation through modification of the perceived nominal sheave angle. The ellipsoid volume for the uncompensated case is also included in Figure 5.8 to demonstrate the relative performance of the Simplified Sheave algorithm with significant error.

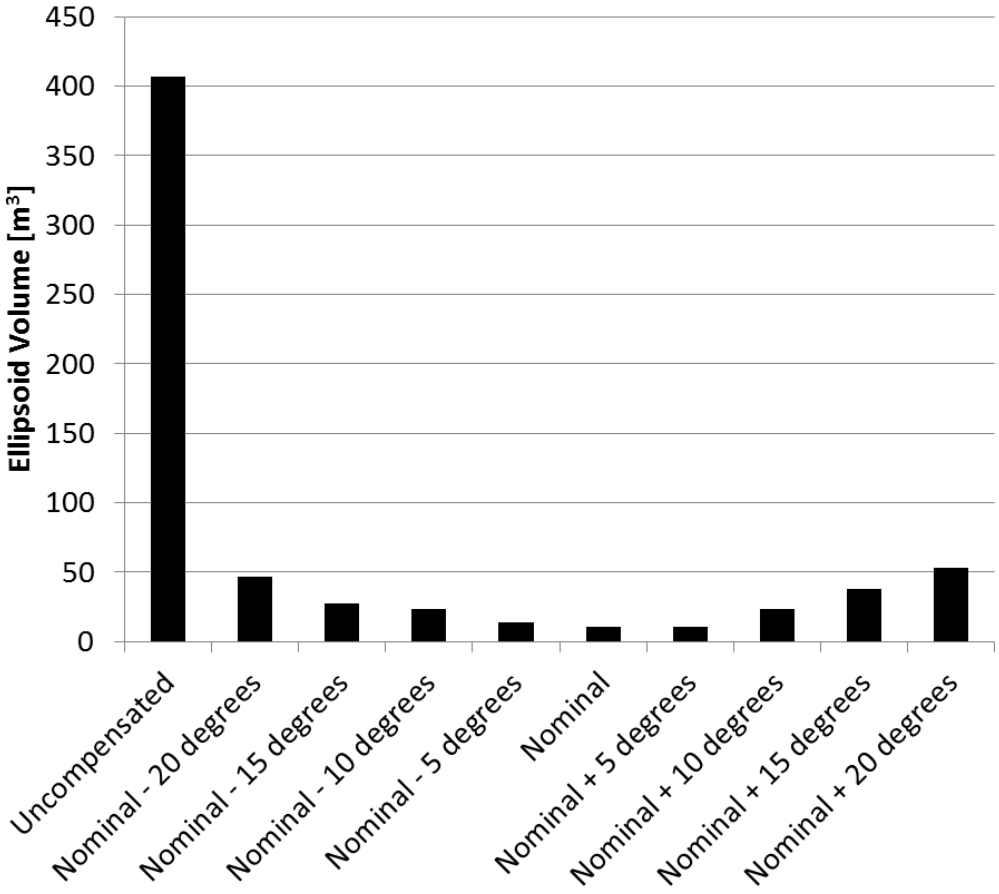


**Figure 5.8: Performance of Simplified Sheave set-point algorithm for nominal towed system parameters with range of nominal sheave angle error.**

Figure 5.8 shows that reasonable performance of the Simplified Sheave algorithm is maintained despite the presence of large angle measurement error in simulation. The introduction of 20 degrees of error into the set-point algorithm increases the ellipsoid volume by a factor of 5 over the case without error. However, the maximum error cases presented in Figure 5.8 still demonstrate an ellipsoid volume reduction of 87% to 89%. The robustness of this method suggests that, for the conditions used in this research, the Simplified Sheave algorithm can be used to effectively compensate for heave motion with a rough estimate of sheave angle.

## 5.3. SUMMARY

Simplified and Rigorous set-point algorithms are compared in full-scale simulation in this chapter, contributing towards the third key objective of this thesis. The performance of

the Simplified Sheave and Rigorous Sheave set-point algorithms is similar for tow cable lengths ranging from 100 m to 460 m, towed body mass ranging from 867 kg to 3468 kg, and tow cable drag coefficients ranging from 0.9 to 2.7. The similarity of these results indicates that for many towing applications, real-time sheave angle measurement can be avoided by using the Simplified Sheave set-point algorithm.

A range of tow cable lengths, cable drag coefficients, and towed body masses are used to conduct a parametric study of set-point algorithm performance in simulation. Good performance is observed with the Sheave algorithm, contributing towards the second key objective of this thesis. Additionally, the performance of the Simplified Sheave algorithm is examined with significant error introduced into the assessment of the nominal sheave angle. Performance of the set-point algorithm is negatively affected by the introduction for this error, but ellipsoid volume reduction of 87% to 89% is still possible with 20 degrees of error introduced.

# CHAPTER 6 CONCLUSION

The three key contributions of this thesis are:

1. To develop an appropriate set-point algorithm for the control of a winch-based AHC system to reduce surface disturbances on passive towed bodies.

2. To determine the most suitable set-point algorithm in flume-scale experimental tests and flume-scale and full-scale simulations.

3. To assess the necessity of real-time measurement of the sheave angle.

This chapter summarizes the results of this thesis in the context of the three key contributinos in Sections 6.1 through 6.5. Section 6.6 identifies areas of future work relating to this project.

## 6.1. CONTRIBUTION ONE: SET-POINT ALGORITHM DEVELOPMENT

Chapter 3 presented two set-point algorithms which were developed for the application of winch-based AHC to passive towed bodies. The set-point algorithms determine the length of tow cable which should be reeled in or out based on measured ship perturbation. Two variants of each algorithm are defined which depend on the presence or absence of additional sensory equipment capable of measuring the towed system's sheave angle in real-time. The four algorithm approaches are:

1. Rigorous Sheave

2. Simplified Sheave

3. Rigorous Waterline

4. Simplified Waterline

The sheave set-point algorithm determines a set-point for a winch system control loop based on the displacement of the host vessel's sheave relative to its expected, unperturbed position. The Waterline set-point algorithm determines a set-point for a winch system

control loop based on ensuring that the same point along the tow cable always crosses the mean water level.

Rigorous set-point algorithm approaches require a real-time measurement of the tow cable sheave angle as it leaves the host vessel and enters the water. Simplified set-point algorithm approaches make the assumption that the sheave angle remains approximately constant when the host vessel is underway.

## 6.2. Contribution Two: Set-Point Algorithm Comparison

Chapters 3, 4, and 5 presented experimental and simulated tests that were conducted to compare the performance of the four set-point algorithm approaches. From among the two principal set-point algorithms, for the conditions used in this research the Sheave algorithm has performed as well or better than the Waterline algorithm across all experimental and simulated tests, with the best observed performance occurring at large tow depths in full-scale simulation. Additionally, the Rigorous Waterline algorithm has frequently demonstrated a tendency to drive the AHC system unstable due to its relatively large response to small changes in sheave angle measurement.

## 6.3. Contribution Three: Simplified and Rigorous Set-Point Algorithm Approaches

From examining the results of experimental and simulated tests presented in Chapters 3, 4, and 5, the usefulness of real-time sheave angle measurement can be assessed. For the conditions used in this research, it was determined that for the flume-scale experimental and simulated tests, a noticeable performance improvement can be achieved by implementing a Rigorous formulation of the Sheave set-point algorithm. A range of full-scale experimental results conducted with different towed system parameters indicated negligible difference between the Simplified and Rigorous Sheave set-point algorithm approaches. This lack of improvement in full-scale simulations suggests that for full-scale applications, real-time sheave angle measurement might not be required and a simplified set-point algorithm approach is sufficient.

## 6.4. FUTURE WORK

This thesis has shown that the Sheave set-point algorithm can provide a suitable signal for an AHC system in experimental and simulated trials. Several recommendations are provided which can help improve simulator accuracy and continue the development of this set-point algorithm.

1. The tow cable is reeled in and out with a prismatic joint in simulation. The extended prismatic joint has no inertial properties, meaning that for significant tow cable extension, some portion of the cable above the waterline is massless. Similarly, for significant tow cable retraction, the first cable segment is partially overhanging behind the sheave, creating an unwanted moment about the sheave. An illustration of these undesired effects is presented in Figure 6.1

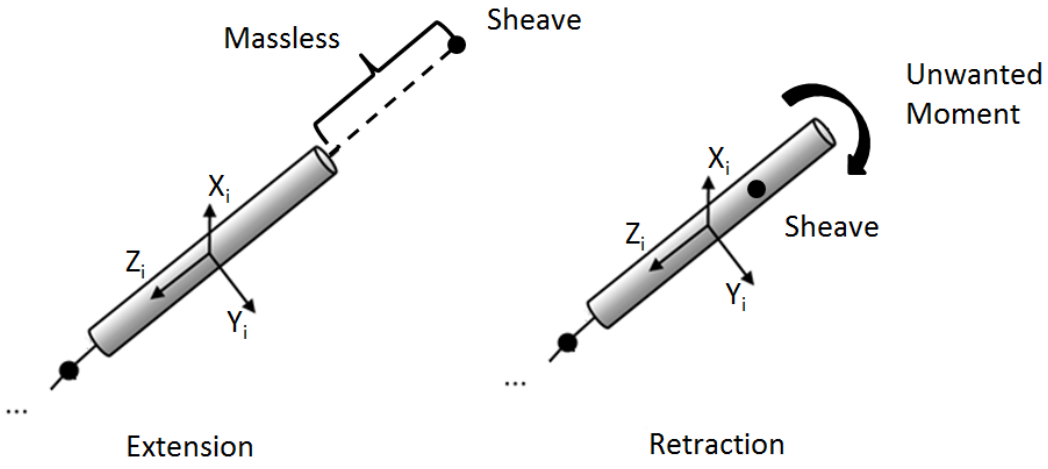


**Figure 6.1: Effects from simplified cable extension and retraction in Simulink model.**

   A more accurate model of the cable links as they are reeled in and out could improve simulator accuracy.

2. Full-scale simulation in this thesis is conducted without the inclusion of full-scale on-board winch dynamics. Inclusion of these dynamics in simulation can improve the accuracy of the full-scale simulator.

3. Additional improvements to the full-scale simulator can be achieved by modifying the towed body model to reflect a more realistic geometry. Set-point algorithm performance can then be studied with a range of towed body designs.

4. Experimental tests with full-scale equipment can be used to empirically test set-point algorithms at sea.

5. Data from full-scale experimental tests can be used to validate a full-scale simulator, improving accuracy.

# REFERENCES


[1] El-Hawary, F. (1982, April). Compensation for source heave by use of a Kalman filter. *IEEE Journal of Oceanic Engineering*, 7(2), 89-96.

[2] Woodacre, J., Bauer, R., Irani, R. (2015, August). A review of vertical motion heave compensation systems. *Ocean Engineering*, 104, 140-154.

[3] Hatleskog, J. & Dunnigan, M. (2006, September). Heave compensation simulation for non-contact operations in deep water. *OCEANS 2006*, 1-6.

[4] Neupert, J., Mahl, T., Haessig, B., Sawodny, O., & Schneider, K. (2008). A heave compensation approach for offshore cranes. *American Control Conference*, pp. 538–543

[5] Benedict, K., Balduf, M., & Kirchhoff, M. (2016). Ships motions related to the axis of the hull. Retrieved from http://schiw.sf.hs-wismar.de/siw/paper/heft5/beitrag10

[6] Rexroth Bosch Group passive heave compensation. Retrieved 2016 from https://www.boschrexroth.com/en/xc/industries/machinery-applications-and-engineering/offshore/products-and-solutions/heave-compensation/passive-heave-compensation/index

[7] Cranemaster. Retrieved 2016 from http://www.cranemaster.no/smarter-systems-more-possibilities

[8] Jakobsen, S. (2008). Passive heave compensation of heavy modules. Master's Thesis. University of Stavanger, Norway

[9] Cannell, D., Labbe, C., Odigie, E., & Riddell, S., (2016). Passive heave compensator. US Patent 20,160,002,012.

[10] Wu, K., Yao, B., Fu, B., Ren, P., & Lian, L. (2011). Research on the performance of passive heave compensator for tethered remotely operated vehicle system. *Journal of Shanghai Jiaotong University (Science)*, 16(1), 40-44.

[11] Driscoll, F., Nahon, M., & Lueck, R. (2000). A comparison of ship-mounted and cage-mounted passive heave compensation systems. *Journal of Offshore Mechanics and Arctic Engineering*, 122(3), 214-221.

[12] Hover, F., Grosenbaugh, M., & Triantafyllou, M. (1994). Calculation of dynamic motions and tensions in towed underwater cables. *Oceanic Engineering, IEEE Journal of*, 19(3), 449-457.

[13] Bliek, A. (1984). Dynamic analysis of single span cables. Ph. D. Massachusets Institute of Technology, United States.

[14] Gu, P., Walid, A., Iskandarani, Y., & Karimi, H. (2013). Modeling, simulation and design optimization of a hoisting rig active heave compensation system.

[15] Do, K. & Pan, J., (2008). Nonlinear control of an active heave compensation system. *Ocean Eng*. 35, 558–571.

[16] Korde, U. (1998). Active heave compensation on drill-ships in irregular waves. *Ocean Engineering,* 25(7), 541-561.

[17] Yao, B., Bu, F., & Chiu, G. (2001). Non-linear adaptive robust control of electro-hydraulic systems driven by double-rod actuators. *International Journal of Control, 74*(8), 761-775.

[18] Hatleskog, J. & Dunnigan, M. (2007, June). Active heave crown compensation sub-system. *OCEANS 2007*, 1-6

[19] Richter, M., Arnold, E., Schneider, K., Eberharter, J., & Sawodny, O. (2014). Model predictive trajectory planning with fallback-strategy for an active heave compensation system. *American Control Conference (ACC), 2014,* 1919-1924.

[20] Küchler, S., Mahl, T., Neupert, J., Schneider, K., & Sawodny, O. (2011). Active control for an offshore crane using prediction of the vessels Motion. *Mechatronics, IEEE/ASME Transactions on, 16*(2), 297-309.

[21] Fusco, F., & Ringwood, J. (2010). Short-term wave forecasting for real-time control of wave energy converters. *Sustainable Energy, IEEE Transactions on,* 1(2), 99-106.

[22] Rao, C., Wright, V., & Rawlings, S. (1998). Application of interior-point methods to model predictive control. *Journal of Optimization Theory and Applications, 99*(3), 723-757.

[23] Woodacre, J. (2015). Model-predictive control of a hydraulic active heave compensation system with heave prediction. M. A. Sc. Thesis. Dalhousie University, Canada

[24] Woodacre, J., Wahidi, W., Bauer, R., & Irani, R. (2016, November) Coupling a standard hydraulic valve and advanced control to achieve a motion compensation system. *2016 ASNE Launch and Recovery*, Linthicum Heights, MD.

[25] Küchler, S., & Sawodny, O. (2010). Nonlinear control of an active heave compensation system with time-delay. *Control Applications (CCA), 2010 IEEE International Conference on,* 1313-1318.

[26] Quan, W., Liu, Y., Zhang, Z., Li, X., & Liu, C. (2016). Scale model test of a semi-active heave compensation system for deep-sea tethered ROVs. *Ocean Engineering, 126*, 353-363.

[27] Huang, L., Zhang, Y., Zhang, L., & Liu, M. (2013). Semi-active drilling drawworks heave compensation system. *Petroleum Exploration and Development Online, 40*(5), 665-670.

[28] Liu, Q., Tang, Y., Xie, C., & Huang, C. (2015). Study on a mechanical semi-active heave compensation system of drill string for use on floating drilling platform. *PLoS ONE, 10*(7), PLoS ONE, 17 July 2015, Vol.10(7).

[29] Qinghui Y. (2010). Actively damped heave compensation (ADHC) system. *American Control Conference (ACC), 2010,*1544-1549.

[30] Yang, W., Zhang, Z., & Zhang, A. (2007). Study on active heave compensation system for underwater vehicle. *Ocean Eng*. 25, 68–73.

[31] Quan, W., Zhang, A., & Zhang, Z. (2013). Modeling and simulation for semi-active heave compensation system of composite-cylinder type. *Mach. Tool. Hydraul*., 1, p. 042

[32] Huang, L., Zhang, Y., Zhang, L., & Liu, M. (2013). Semi-active drilling drawworks heave compensation system. *Petroleum Exploration and Development Online, 40*(5), 665-670.

[33] Hatleskog, J. & Dunnigan, M. (2006). Heave compensation simulation for non-contact operations in deep water. *OCEANS 2006*, 1-6.

[34] Howell, C. (1992). Investigation of the dynamics of low-tension cables. Ph. D. Thesis. Massachusetts Institute of Technology, United States.

[35] Irvine, H., & Caughey, T. (1974). The linear theory of free vibrations of a suspended cable. *Proceedings of the Royal Society of London. Series A, Mathematical and Physical Sciences (1934-1990), 341*(1626), 299-315.

[36] Triantafyllou, M. (1991). Dynamics of cables, towing cables, and mooring systems. *Shock and Vibration Dig.* 23, 3-8.

[37] Chen, B., Su, F., Huo, C., Zhang, R., Yao, B., & Lian, L. (2015). Numerical investigation of the dynamics for low tension marine cables. *Journal of Shanghai Jiaotong University (Science), 20*(3), 257-264.

[38] Sun, Zhu, & Larosa. (2011). Dynamic modeling of cable towed body using nodal position finite element method. *Ocean Engineering, 38*(4), 529-540.

[39] Driscoll, Lueck, & Nahon. (2000). Development and validation of a lumped-mass dynamics model of a deep-sea ROV system. *Applied Ocean Research, 22*(3), 169-182.

[40] Wu & Chwang. (2001). Investigation on a two-part underwater manoeuvrable towed system. *Ocean Engineering, 28*(8), 1079-1096.

[41] Reissner, E. (1972). On one-dimensional finite-strain beam theory: the plane problem. *Zeitschrift Für Angewandte Mathematik Und Physik ZAMP, 23*(5), 795-804.

[42] Simo, J. C. & Vu-Quoc, L. (1986). A three-dimensional finite-strain rod model, Part II: Computational aspects. *Computer Methods in Applied Mechanics and Engineering*, 58(1), 79-116.

[43] Cardona, A. & Geradin, M. (1988). A beam finite element nonlinear theory with finite rotations, *Int. J. Numer. Methods Eng.*, 26(11), 2403-2438.

[44] Ablow C. M. & Schechter S. (1983). Numerical simulation of undersea cable dynamics. *Ocean Engineering*, 10(6), 443-457.

[45] Park, Jung, & Koterayama. (2003). A numerical and experimental study on dynamics of a towed low tension cable. *Applied Ocean Research, 25*(5), 289-299.

[46] Calnan, C., Bauer, R., & Irani, R. (2016, September) Controller design and motion compensation for marine towed bodies. *IEEE/MTS OCEANS 16*, Monterey, CA.

[47] Nortek Instruments. Vectrino high-resolution acoustic doppler velocimeter datasheet. Retrieved in 2016 from http://www.nortek-as.com/en/products/velocimeters/vectrino

[48] Kamman, J., & Huston, W. (2001). Multibody dynamics modeling of variable length cable systems. *Multibody System Dynamics, 5*(3), 211-221.

[49] Arney, A., (1994, October). FFG-7 ship motion and airwake trial. part II : removal of ship motion effects from measured airwake data. *Air Operations Division Aeronautical and Maritime Research Laboratory*, Melbourne Victoria, Australia.

[50] Avago technologies. AEAT-6012-A06 12-bits magnetic encoder datasheet. Retrieved in 2016 from http://www.avagotech.com/products/motion-control-encoders/magnetic-encoders/aeat-6012-a06#specifications

[51] Canon Canada inc. About EOS 7D specifications. Retrieved in 2016 from http://www.canon.ca/inetCA/en/products/method/gp/pid/873

[52] GoPro. Hero3+ user manual. Retrieved in 2016 from http://cbcdn2.gp-static.com/uploads/product_manual/file/195/UM_H3PlusSilver_ENG_REVB_WEB.pdf

[53] DC motor speed: system modeling. *Control tutorials for MATLAB & Simulink*. Retrieved in 2016 from http://ctms.engin.umich.edu/CTMS/index.php?example=MotorSpeed&section=SystemAnalysis

[54] Amprobe. 34XR-A digital multimeter data sheet. Retrieved in 2016 from http://www.tme.eu/en/Document/9794b2c662c23f17dd15f86c0a9195b6/34XRA.pdf

[55] BK precision. High accuracy handheld LCR/ESR meters: model 885 overview. Retrieved in 2016 from http://www.bkprecision.com/products/component-testers/885-synthesized-lcr-esr-meter-with-smd-probe.html

[56] Unal, H., Findik, F., & Mimaroglu, A. (2003). Mechanical behavior of nylon composites containing talc and kaolin. *Journal of Applied Polymer Science, 88*(7), 1694-1697.

[57] Berkley. Angler education: why use monofilament. Retrieved in 2016 from http://www.berkley-fishing.com/Berkley-ae-why-use-monofilament.html

[58] Epps, B., Techet, A. (n.d.). 2.016 Hydrodynamics. Retrieved in 2016 from http://web.mit.edu/2.016/www/handouts/Added_Mass_Derivation_050916.pdf

[59] Munson, B., Young, D., & Okiishi, T. (2006). Fundamentals of fluid mechanics. Hoboken, NJ: J. Wiley & Sons.

[60] Walton, C. & Billhart, R. (1966). The stability derivatives of the scheme a body used with the AN/SQA-13 (XN-1) variable depth sonar system. *Hydromechanics Laboratory David Taylor Model Basin Department of the Navy*

[61] Zhu, Z., Meguid, S., Ong L. (2003). Dynamic multiscale simulation of towed cable and body. *Proceedings of Computational Fluid and Solid Mechanics*, 1–2, 800–803.